TECHNISCHE UNIVERSITÄT MÜNCHEN

NAT
TUM School of Natural Sciences

Bachelor's Thesis

Characterization of Bent CMOS MAPS Detectors for ALICE ITS3

Philipp Antonius Maria Mann

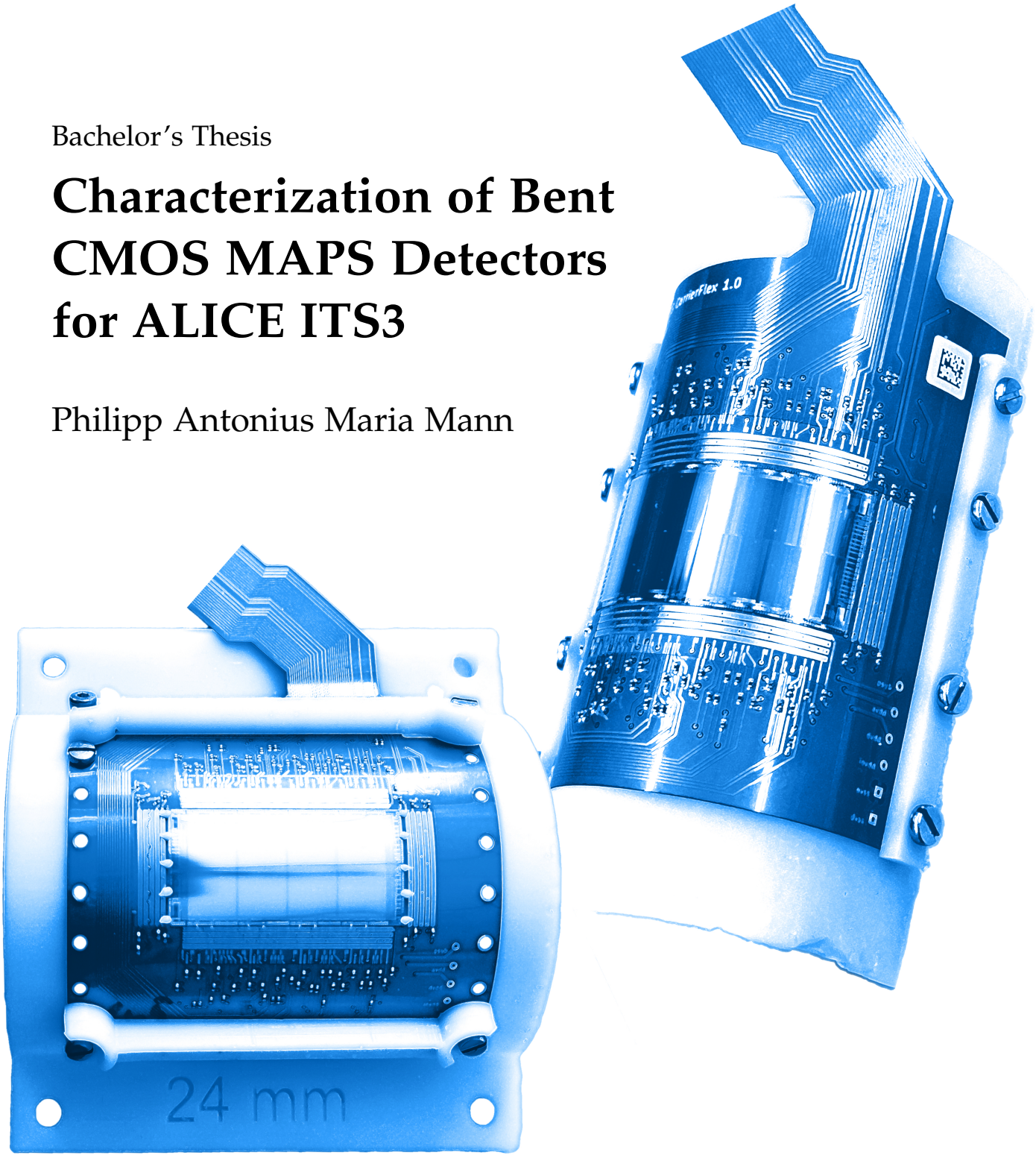

TECHNISCHE UNIVERSITÄT MÜNCHEN

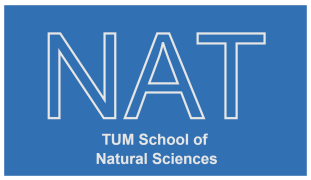

Characterization of Bent CMOS MAPS Detectors for ALICE ITS3

Charakterisierung von gebogenen CMOS MAPS Detektoren für ALICE ITS3

Bachelor's Thesis

Author: Philipp Antonius Maria Mann
Primary Examiner: Prof. Dr. Laura Fabbietti
Supervisor: Berkin Ulukutlu
Date: November 15, 2025

I confirm that the results presented in this bachelor's thesis is my own work and I have documented all sources and materials used.

Ich versichere, dass ich diese Bachelorarbeit selbstständig verfasst und nur die angegebenen Quellen und Hilfsmittel verwendet habe.

Munich, November 15, 2025 Philipp Antonius Maria Mann

Abstract

This work investigates the effects of bending on CMOS MAPS prototypes, designed for ALICE's ITS3 upgrade. For this, small-scale prototypes – babyMOSSes – were mounted onto FPCs, bent to different configurations, and investigated in lab scans as well as a testbeam, where the DACs, the threshold of the analog frontend, the fake hit rate, and the efficiency were measured. Apart from the physical setups used, the software modifications to corryvreckan and EUDAQ2 used to analyze the gathered data will be introduced. This work shows that the operating point of the prototypes changes with bending in terms of the settings provided to the chip and partially recovers upon unbending. The DACs responsible for converting these settings into physical values change, therefore these cannot be ruled out as the reason for the change of the operating point. Despite this, the available headroom in the chip's configuration should allow for the compensation of these changes.

Contents

Acronyms

p_T transverse momentum.

ALICE **A** **L**arge **I**on **C**ollider **E**xperiment.

ALPIDE **AL**ICE **Pi**xel **De**tector.

ATLAS **A** **T**oroidal **L**HC **A**pparatu**s**.

babyMOSS One RSU variant of the MOSS.

BOT bottom.

CERN European Organization for Nuclear Research.

CMOS **C**omplementary-**M**etal-**O**xide **S**emiconductor.

CMS **C**ompact **M**uon **S**olenoid.

corry **Corry**vreckan framework.

DAC **D**igital **A**nalog **C**onverter.

DAQ **D**ata **Acq**uisition.

DUT **D**evice **U**nder **T**est.

ELSA **El**ektronen **S**tretcher **A**nlage.

EMCal **E**lectro**m**agnetic **Cal**orimeter.

ER1 **E**ngineering **R**un **1**.

EUDAQ2 Software Framework for DAQ in testbeams.

FIT **F**ast **I**nteraction **T**rigger.

FPC **F**lexible **P**rinted **C**ircuit.

FPGA **F**ield **P**rogrammable **G**ate **A**rray.

GEM **G**aseous **E**lectron **M**ultiplier.

HIC **H**ybrid **I**ntegrated **C**ircuit.

HL-LHC **H**igh **L**uminosity **L**arge **H**adron **C**ollider.

HMPID **H**igh **M**omentum **P**article **I**dentification **D**etector.

HU **H**alf **U**nit.

IB **I**nner **B**arrel.

ITS **I**nner **T**racking **S**ystem.

ITS2 second iteration of ALICE's **I**nner **T**racking **S**ystem.

ITS3 third iteration of ALICE's **I**nner **T**racking **S**ystem.

LDO **L**ow **D**rop**o**ut Regulator.

LEIR **L**ow **E**nergy **I**on **R**ing.

LHC **L**arge **H**adron **C**ollider.

LHCb **L**arge **H**ardron **C**ollider **b**eauty.

LINAC **Lin**ear **Ac**celerator.

MAPS **M**onolithic **A**ctive **P**ixel **S**ensor.

MCH **M**uon Tracking **Ch**ambers.

MFT **M**uon **F**orward **T**racker.

MID **M**uon **Id**entifier.

MOSS **Mo**nolithic **S**titched **S**ensor.

MOST **Mo**nolithic **S**titched Sensor **T**iming.

NMOS **p**-channel **M**etal **O**xide **S**emiconductor.

OB **O**uter **B**arrel.

PCB **P**rinted **C**ircuit **B**oard.

PHOS **Pho**ton **S**pectrometer.

PID **p**article **id**entification.

PMOS **p**-channel **M**etal **O**xide **S**emiconductor.

PMT **P**hoto **M**ultiplier **T**ube.

PS **P**roton **S**ynchrotron.

QGP **Q**uark **G**luon **P**lasma.

RICH **R**ing **I**maging **C**herenkov **D**etector.

ROI **R**egion **O**f **I**nterest.

RSU **R**epeated **S**ensor **U**nit.

SPS **S**uper **P**roton **S**ynchrotron.

TOF **T**ime **o**f **F**light.

TOP top.

ToT **T**ime **o**ver **T**hreshold.

TPC **T**ime **P**rojection **C**hamber.

TRD **T**ransition **R**adiation **D**etector.

USB **U**niversal **S**erial **B**us.

ZDC **Z**ero **D**egree **C**alorimeter.

1 Introduction

The sections in this chapter aim to provide a general context for the conducted research and introduce the technology investigated. The following chapters introduce the setups and then the analysis pipelines used. Finally, the results will be presented in a structured manner.

1.1 The Large Hadron Collider

The **L**arge **H**adron **C**ollider (LHC), as shown in Figure 1.1, is currently the largest and most powerful stage of the particle acceleration complex at the European Organization for Nuclear Research (CERN). Measuring 26.7 km in circumference, it is located between 45 m and 170 m below ground at Geneva lake, where it occupies the same tunnel in which the Large Electron Positron Collider was previously located. [1, 2]

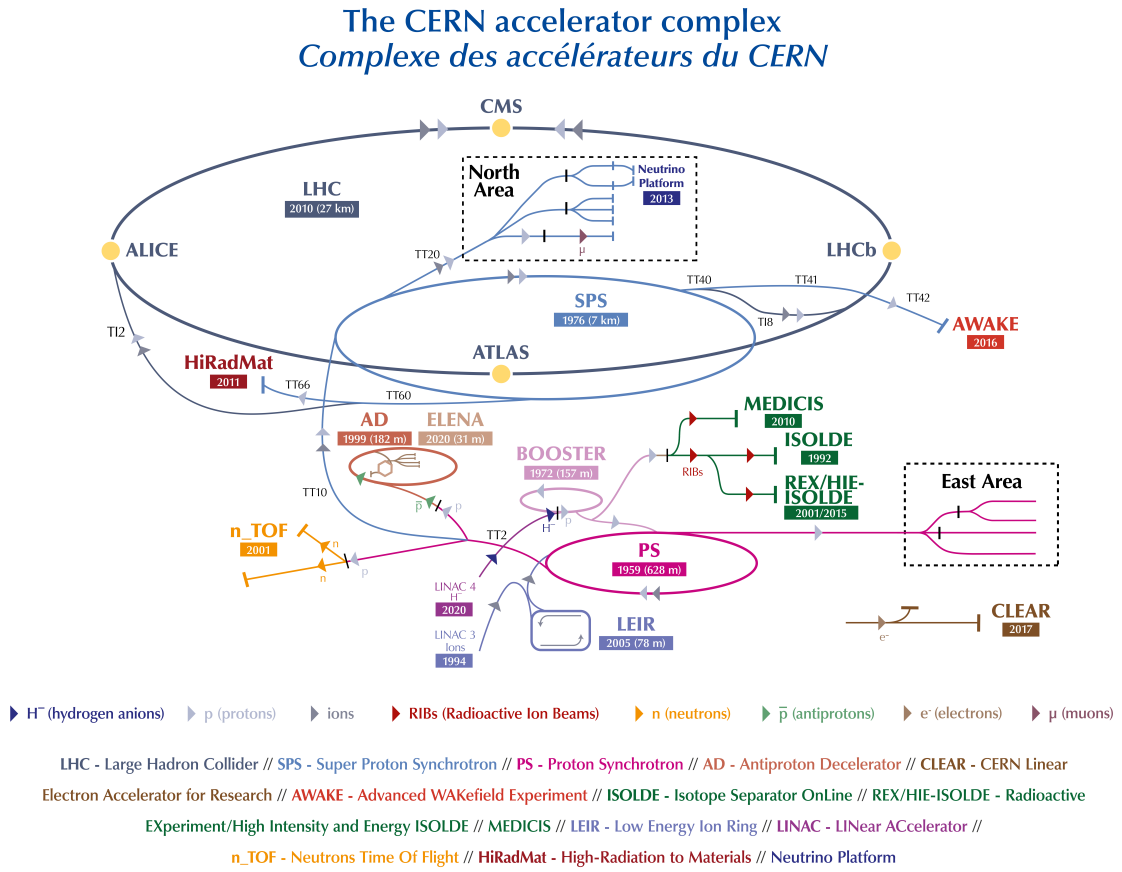

Figure 1.1: Schematic overview of the particle accelerator complex with LHC experiments at CERN. Taken from [3].

Since its first commission in 2008, it has been colliding two bunched beams of hadronic matter – mostly protons and lead nuclei – although lighter nuclei such as xenon, oxygen, and neon are being introduced [1, 4–6].

After production, the protons or ions start their journey in dedicated **Lin**ear **Ac**celerators (LINACs): LINAC 4 and LINAC 3, respectively. The protons, which at this stage still are negative hydrogen ions, continue into the BOOSTER, where they are stripped of their electrons before being injected into the **P**roton **S**ynchrotron (PS). The second stage for the ions is the **L**ow **E**nergy **I**on **R**ing (LEIR), whereupon they are also transferred to the PS. After further acceleration in the **S**uper **P**roton **S**ynchrotron (SPS) both of them end up in the LHC where their final energy is reached. [1, 3, 7]

The beams revolve in opposite directions around the LHC in two separate tubes, being kept on track by a magnet field slightly stronger than 8 T generated by 1232 dipole magnets. The beams cross each other at four points and collide with a center-of-mass energy of $\sqrt{s_{\mathrm{pp}}} = 13\,\mathrm{TeV}$ for proton-proton and $\sqrt{s_{\mathrm{NN}}} = 5.36\,\mathrm{TeV/nucleon}$ for lead-lead. [1, 2]

At each interaction point, one of the main experiments is located, all with different specializations:

A Large Ion Collider Experiment (ALICE) is the only dedicated ion collision experiment at the LHC. It predominantly studies physics related to **Q**uark **G**luon **P**lasma (QGP). [8]

A Toroidal LHC Apparatus (ATLAS) is a general-purpose detector which studies a variety of physics, starting at the Standard Model and going beyond to dark matter candidates or extra dimensions. [9]

Compact Muon Solenoid (CMS) has the same objectives as ATLAS – although it uses different technical solutions, including a different magnet design. [10]

Large Hardron Collider beauty (LHCb) studies the asymmetry between matter and antimatter through the investigation of heavy beauty quarks. Its layout differs significantly from that of the other detectors, as it only detects forward particles, rather than symmetrically surrounding the collision point. [11]

Since the first fundamental discovery of the Higgs Boson in 2012 by ATLAS and CMS [12], the accelerator and its experiments have been further developed to increase statistics and accuracy, enabling more precise measurements and paving the way for new discoveries. The next upgrade, known as the **H**igh **L**uminosity **L**arge **H**adron **C**ollider (HL-LHC), is planned to increase the luminosity and, consequently, the collision rate by a factor of five. This aims to increase the total integrated luminosity by a factor of ten [13]. The upgrade will be implemented during the so-called Long Shutdown 3, which is scheduled to last from 2026 to 2030, during which the experiments will install upgrades [14]. This includes ALICE's ITS3 (cf. Section 1.4), although it will not yet increase the capabilities to accommodate the increased interaction rate.

1.2 The ALICE Detector

Before discussing the upgrade, it is sensible to elaborate on the current version of ALICE, as depicted in Figure 1.2. Measuring $16 \cdot 16 \cdot 26$ m^3 in volume and 8000 t in weight, it surrounds the interaction point 2 of the LHC in St. Genis [15]. The various subsystems complement each other, optimizing the detector for studying QGP produced in heavy-ion collisions. This entails not only providing track reconstruction in the highest multiplicity events at the LHC, but also excellent **p**article **id**entification (PID) over a wide range of transverse momenta p_{T}. In addition, the interaction rate the detector can handle is also optimized[1] [16, 17].

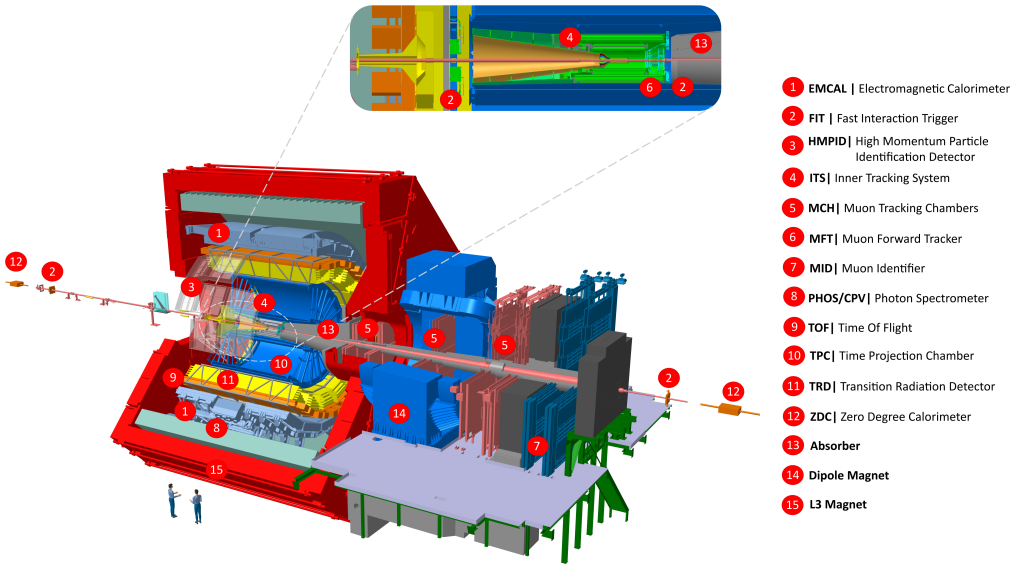

Figure 1.2: Detector Systems of ALICE 2 after the upgrade in long shutdown 2 2019–2022. Taken from [16].

Also visible in Figure 1.2 is that the experiment consists of two main parts: the central barrel detectors and a forward acceptance muon spectrometer. The red L3 solenoid magnet generates a homogeneous magnetic field of 0.5 T encompassing the central barrel detectors. [16, 17]

Closest to the interaction point, the second iteration of ALICE's **I**nner **T**racking **S**ystem (ITS2) is located. It consists of seven concentric layers of MAPS that are distributed over a 22 mm to 395 mm radial range and covers a pseudorapidity of $|\eta| \leq 1.3$ [16]. This makes the ITS2 the biggest **M**onolithic **A**ctive **P**ixel **S**ensor (MAPS) based detector in use to date. Its main purpose is to provide accurate information on the primary vertex and improve the tracking of particles with low p_{T} [18]. It will be described in more detail in Section 1.4.

Next is the **T**ime **P**rojection **C**hamber (TPC), extending from a radius of 0.85 m to 5 m, whilst spanning 5 m in the beam direction [16]. Featuring a fast **G**aseous **E**lectron **M**ultiplier (GEM) readout, it is not only the main workhorse for ALICE's tracking but

[1] The rates ALICE operates at are actually rather low in comparison to the other experiments.

also used for PID up to momenta in the order of 50 GeV [17].

The third detector, spanning radially from 2.8 m to 3.5 m, is the **T**ransition **R**adiation **D**etector (TRD), which is designed for the identification of electrons above 1 GeV through their transition radiation and to provide additional space points. These can be used to complement the tracking, provide general $\mathrm{d}E/\mathrm{d}x$ measurements for PID, or as a method to determine the size of space distortions caused by charge effects in the TPC. [16, 17]

The next layer, located at a radius of around 4 m, is the **T**ime **o**f **F**light (TOF) detector. Consisting of multigap resistive plate chambers, which provide a time resolution below 100 ps, the TOF is used to identify hadrons over a large range in momenta, as well as low-momentum electrons [16, 17].

The **H**igh **M**omentum **P**article **I**dentification **D**etector (HMPID) is a **R**ing **I**maging **C**herenkov **D**etector (RICH) designed to improve the high momentum hadron identification capabilities, having a total surface area of only $10\,\mathrm{m}^2$ [16, 17]. It is also equipped with additional absorbers to measure light anti-nuclei [16].

The **E**lectro**m**agnetic **Cal**orimeter (EMCal) and **Pho**ton **S**pectrometer (PHOS) are both electromagnetic calorimeters with different goals. The former is focused on measuring jet production rates and fragmentation functions, while the latter features higher spatial and energy resolutions. At a radius of around 4.6 m, they finish the central barrel part of the detector. [16, 17]

The second main component of ALICE is the muon spectrometer, which is positioned in the forward direction, covering a pseudorapidity range of $-4.0 < \eta < -2.5$. Using a combination of high- and low-Z absorbers, hadrons are being removed, and the background from pions and kaons is reduced. The muons are tracked by three layers. First is a pixel silicon detector – the **M**uon **F**orward **T**racker (MFT) – that employs the same technology as ITS2 located even before the so-called muon plug. After that, the muons pass multiwire proportional chambers, the **M**uon Tracking **Ch**ambers (MCH), which are situated before, inside, and after the dedicated dipole magnet. Finally, after passing through even more iron absorbers, resistive plate chambers, called the **M**uon **Id**entifier (MID), are positioned. [16, 17]

Additionally, there are a few more systems, such as the **F**ast **I**nteraction **T**rigger (FIT), which consists of multiple subdetectors, or the **Z**ero **D**egree **C**alorimeter (ZDC), providing additional functionality [16].

1.3 Monolithic Active Pixel Sensors

Before diving into the design versions two and three of the ITS, the underlying **M**onolithic **A**ctive **P**ixel **S**ensor (MAPS) technology will be introduced in general. It is a subcategory of semiconductor particle detectors, in which the sensors are not only structured into individual picture elements, also known as pixels, but also contain the readout electronics on the same chip. [20, 21]

Nevertheless, the basic working principle remains the same and is schematically depicted in Figure 1.3. The central element for any semiconductor-based detector is the

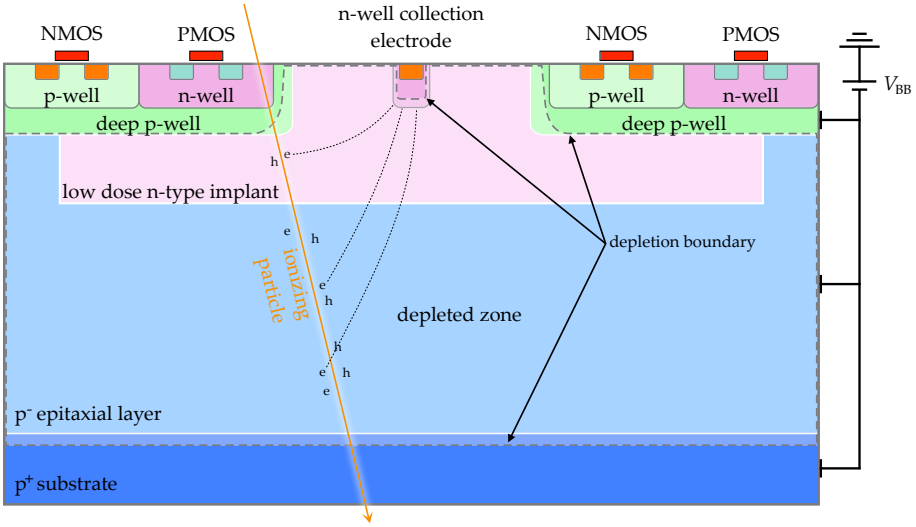

Figure 1.3: Schematic cross section of a pixel in the modified-with-gap design, taken from [19]. The basic working principle of MAPS and the application of backbias are also indicated, following figures and descriptions from [20, 21].

p-n junction, which forms at the interface of p-doped and n-doped material.

The former is characterized by an abundance of holes (positively charged carriers describing a lack of electrons) and is produced by implanting acceptor atoms into the semiconductor. The situation is reversed for the latter: There is an excess of negatively charged carriers (i.e., electrons) originating from donor atoms. Due to the non-vanishing gradient of the charge carrier density, the electrons and holes diffuse from one side to the other. Upon meeting in the middle, they recombine, effectively reducing the number of free charge carriers. Since the immobile dopant ions remain, the diffusion generates an opposing electric field, which stops further macroscopic changes in the charge carrier densities when equilibrium is reached. This leads to a finite depletion zone, in which there are almost no free-moving charges. [20, 21]

Now, electron-hole (e-h) pairs can be generated by relativistic charged particles or by photons in the keV to MeV range, in both cases when they deposit energy into the material. When using silicon as the semiconductor (as all the detectors discussed in this work do) 3.6 eV of deposited energy generate, on average, one e-h pair. [20] In the depletion region, the electric field separates the charge carriers, causing them to drift toward the electrodes. This generates a current pulse that serves as the detector signal for electronic processing. The typical drift time for crossing the depletion region in silicon pixel detectors is around 6 ns. Therefore, the main advantages of MAPS include not only their excellent spatial resolution, achieved through their pixel size, but also their speed in comparison to other detector types. [21]

Furthermore, to increase the depletion zone's volume and decrease its associated capacitance, a so-called backbias voltage V_{BB} can be applied, also positively influencing the signal-to-noise ratio. When thinking of the p-n junction as a diode, this means operating it in the reverse bias direction, i.e., having a higher potential on the n-doped side in comparison to the p-doped one. [20, 21] Subsequently, the differences in silicon

detectors not only arise from the shapes of the active areas but also from the strategies on how to amplify, shape, and read out the generated signal. For all the mentioned aspects, different approaches are available, an overview of which can be found in [20, 21]. Here only the **C**omplementary-**M**etal-**O**xide **S**emiconductor (CMOS) based MAPS will be introduced, as it is the only one relevant for this work.

The term monolithic in MAPS implies that the detection and readout happen on the same chip. This includes the analog amplification and digitization stages for signal processing, an example of which for the MOSS can be seen in Figure 1.8. Both of these stages will be discussed in Section 1.5. Additionally, the digital circuitry related to the readout chain of the entire pixel matrix is also located on the same substrate. [20–23] Traditionally, the use of PMOS transistors was restricted to the outside of the pixel's area, limiting the capabilities of the readout schemes. Through the use of deep p-wells, the n-wells of the PMOS transistors are shielded from the epitaxial layer, preventing interference with the charge collection, as also depicted in Figure 1.3. This enables their usage in the pixel matrix itself, unlocking the full potential of CMOS circuits for more advanced readout schemes while maintaining pixel performance. [22] Apart from the use of backbias, the layout of differently doped regions in a pixel can be used to influence the shape of the depleted zone [23]. The layout seen in Figure 1.3 is known as modified-with-gap, which is implemented in the babyMOSSes used in this work and will be discussed further in Section 1.5 [19].

1.4 From ITS2 to ITS3

Now, after the relevant technology has been introduced, the ITS3 upgrade is discussed. To understand its scope, though, it is sensible to start with a short overview of the ITS2. Its general schematic layout of the latter can be seen in Figure 1.4a. The following description is based on [16, 18], unless indicated otherwise.

The seven layers of the ITS2 are numbered starting from zero and are divided into two barrels, each of which consists of two half-barrels. The **I**nner **B**arrel (IB) consists of the innermost three layers located at an average radius of 23 mm, 31 mm, and 39 mm from the center of the beam pipe, respectively. The middle layers (no. 3 and 4) and outer layers (no. 5 and 6) then from the **O**uter **B**arrel (OB), ranging from a radius of 196 mm to 393 mm. Each layer is comprised of a number of staves, which constitute the basic detector unit[2]. Each stave in turn is made of several components, as shown in Figure 1.4b. The MAPS chips used in this detector – the **AL**ICE **Pi**xel **De**tectors (ALPIDEs) – are bonded to an **F**lexible **P**rinted **C**ircuit (FPC) in addition to some passive components, which together form the **H**ybrid **I**ntegrated **C**ircuit (HIC). The FPC is responsible for the connection of the ALPIDEs with the outside, i.e., it handles not only the power distribution but also all I/O. The HIC is glued to the Cold Plate, a carbon fiber sheet with high thermal conductivity, into which the cooling pipes are also embedded. For the IB, this is integrated into the spaceframe, which provides the necessary mechanical support and stiffness to the entire assembly. Multiple staves are

[2]The staves of the OB are larger than the IB staves and are comprised of more segments. As this is not relevant here, the focus will be on the IB staves. The interested reader is referred to [16, 18]

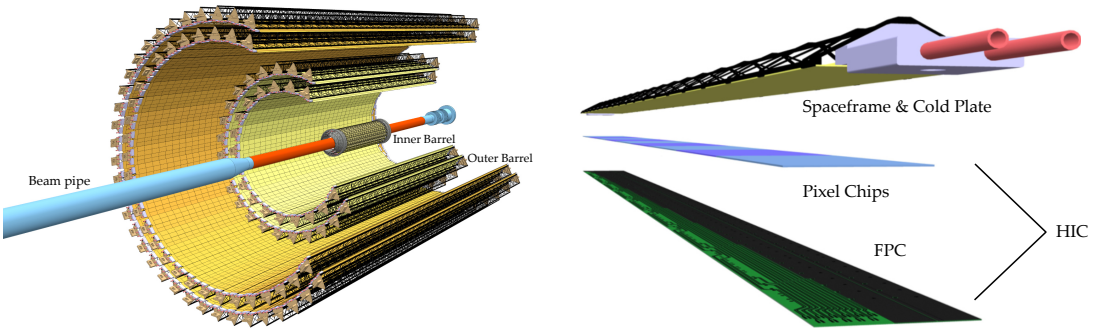

(a) Layout, taken from [18]. **(b)** Inner barrel stave, taken from [24].

Figure 1.4: Schematics of the ITS2.

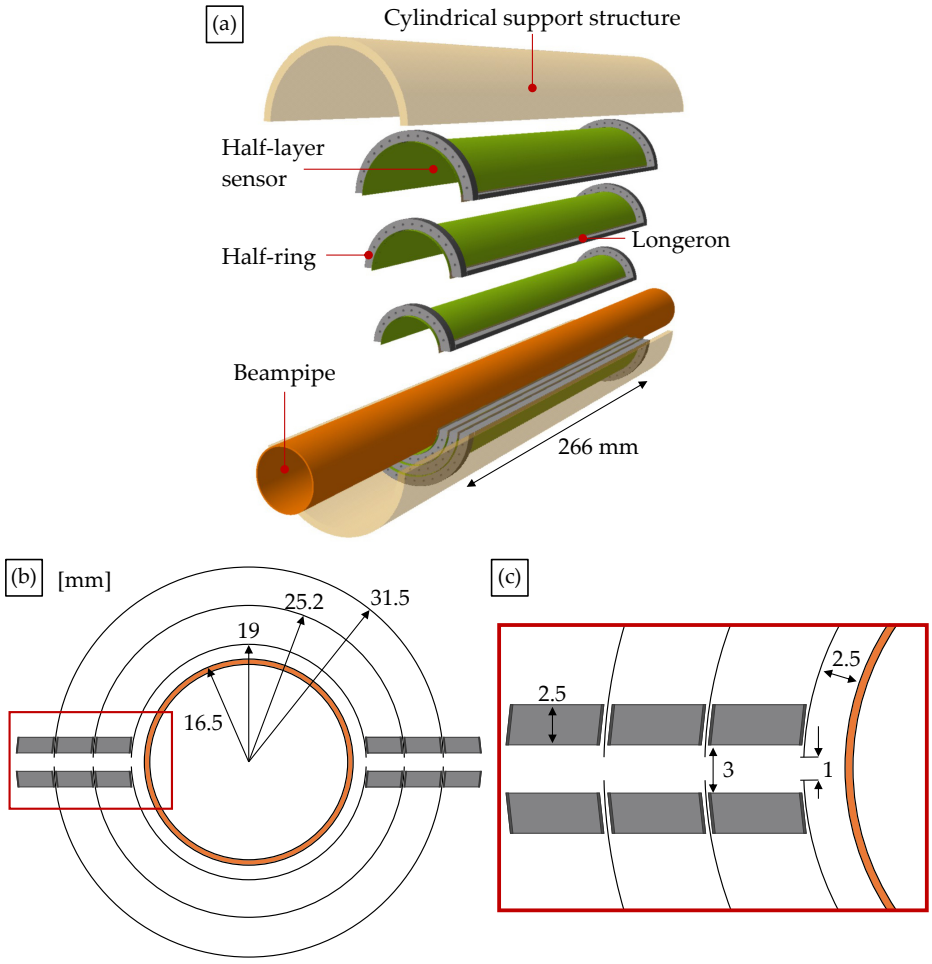

Figure 1.5: Simplified ITS3 Detector layout. Taken from [19]. (a) Top 3 and bottom 3 half-layers around the beam pipe within the cylindrical support structure supported by carbon fiber foam half-rings and longerons. (b) radial distance of beam pipe and layers 0, 1, 2. (c) magnification of supporting structures.

then mounted in a cylindrical fashion, forming the layers depicted in Figure 1.4a.

An analysis of the material budget of ITS2 shows that only about 15 % is accounted for by the 50 µm thick silicon ALPIDEs. The rest results from the FPC, which is the main contributor with about 50 % of the total, as well as the cooling and the spaceframe, contributing about 20 % and 15 % each. Aside from high intrinsic spatial resolution and proximity to the interaction point, a low material budget is imperative for high parameter resolution at low momenta. Achieving the latter will not only improve upon existing measurements but also pave the way for new ones. Since, strictly speaking, the MAPS chips are the only components required to be in the detector's acceptance, the goal of the ITS3 is to get as close to this ideal case as possible [19, 24, 25].

Through a process called stitching, which will be introduced in more detail in Section 1.5, the usual chip size limitations can be overcome, allowing for the creation of full wafer-scale sensors that also incorporate power distribution, sensor control, and data acquisition on-chip. After production using the selected 65 nm technology on 300 mm wafers, they can be thinned, enabling them to be bent into half-cylinders. These will form in total six so-called half-layer sensors[3] of three different radii replacing the IB of ITS2. A schematic drawing including approximate dimensions can be found in Figure 1.5. This geometry allows the sensor to retain its shape with only a minimal amount of lightweight carbon foam support, specifically the half-rings and longerons depicted in Figure 1.5a which also serve as heat radiators. As has also been demonstrated through full-scale thermal prototypes, sufficient cooling can be achieved using air only, flowing parallel to the beampipe at a speed in the order of $8\,\mathrm{m\,s^{-1}}$. Lastly, the whole electronic interface of the sensors is located on the short side, which further eliminates the need for extra electronic circuitry inside the detector's acceptance. In total, this not only leads to a reduction of the material budget per layer from 0.36 % X_0 down to 0.07 % X_0 [4], but also enables the innermost layer to be placed closer to the interaction point than before. As a consequence of this upgrade, simulations predict an improvement of tracking efficiency for low p_T as well as a doubling of the pointing resolution across the board. [19, 24, 26]

1.5 The MOSS and its Baby

The **Mo**nolithic **S**titched **S**ensor (MOSS) is the largest prototype in the **E**ngineering **R**un **1** (ER1), measuring 259 mm · 14 mm in size and containing a total of 6.72 megapixels. As the name implies, this sensor, as well as the **Mo**nolithic **S**titched Sensor **T**iming (MOST), which is not relevant in this work, are created by a manufacturing process called stitching. [19]

Typically, the upper size limit of CMOS chips is determined by the dimensions of the reticle used, as these are individually projected onto the wafer next to each other

[3] These will measure roughly 266 mm in length along the beam direction with different widths for each layer: 59 mm, 78 mm and 98 mm for layer 0, 1 and 2 respectively.

[4] X_0 is the radiation length. It is defined as the mean length an electron needs to traverse through a material to reduce its energy to $1/e$ of its initial value, i.e., it lost $1 - 1/e \approx 63\,\%$. [21]

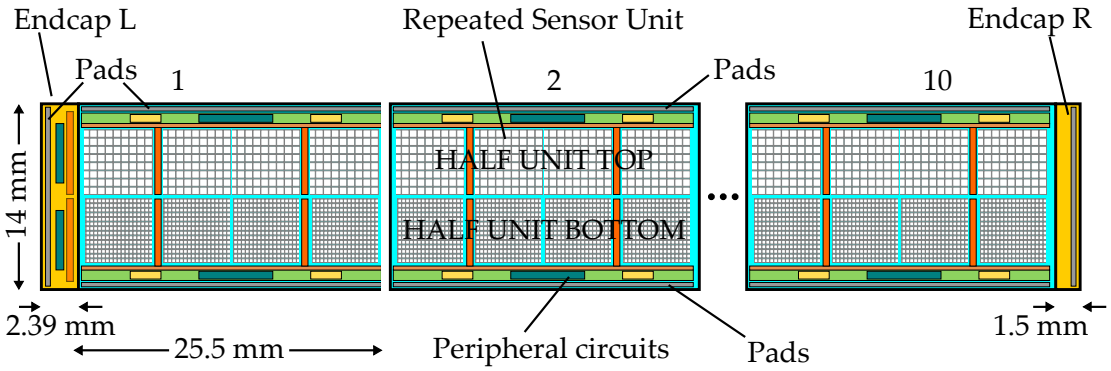

Figure 1.6: Concept diagram of the MOSS chip. Taken from [19]

with a small space in between [24, 27]. The reticle's maximum size is in turn limited by the field of view used in the photolithography steps in the production, which in this context is about 3 cm · 2 cm [24, 26, 27]. Now, if the reticles are designed accordingly, they can be precisely aligned with a small, well-defined overlap, connecting them together. By repeating them a number of times, they form one large functional unit [24]. Exactly this has been implemented for the MOSS, where in total 10 of the so-called **R**epeated **S**ensor **U**nits (RSUs) have been stitched together and terminated on the short ends by the left and right endcaps, respectively [24, 26, 27]. A conceptual drawing of this can be found in Figure 1.6, while a picture of the finished wafer is shown in Figure 1.7. Using the pads on all sides[5], the MOSS can then be connected to a dedicated **D**ata **Acq**uisition (DAQ) system used to characterize the sensor. Due to the chip's size, the test system (approximately 65 cm · 15 cm) is bulky and difficult to handle, especially for use in testbeam telescopes. [19, 26]

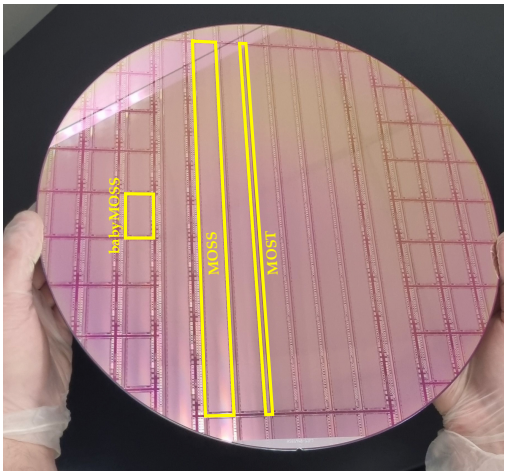

Figure 1.7: Overview of a 300 mm ER1 wafer, containing six MOSS and MOST stitched sensors, a number of babyMOSS (these three are indicated), and other small prototype chips. Taken from [19] and modified.

Fortunately, a smaller prototype – the babyMOSS – is also available, which consists of only one RSU with both endcaps and is therefore virtually identical to the MOSS [19, 26]. It is the main component of interest in this work. Its test system will be described in Section 2.1, while its functionality will be discussed in the following. Each RSU and therefore babyMOSS consists of two **H**alf **U**nits (HUs): the top (TOP) and bottom (BOT). Each of these HUs features four individual pixel matrices called regions. For the TOP HU these contain 256 · 256

[5]For the final sensor of the ITS3, the connections will only be made using the equivalent of the left endcap and, if needed, the right endcap for power support [19].

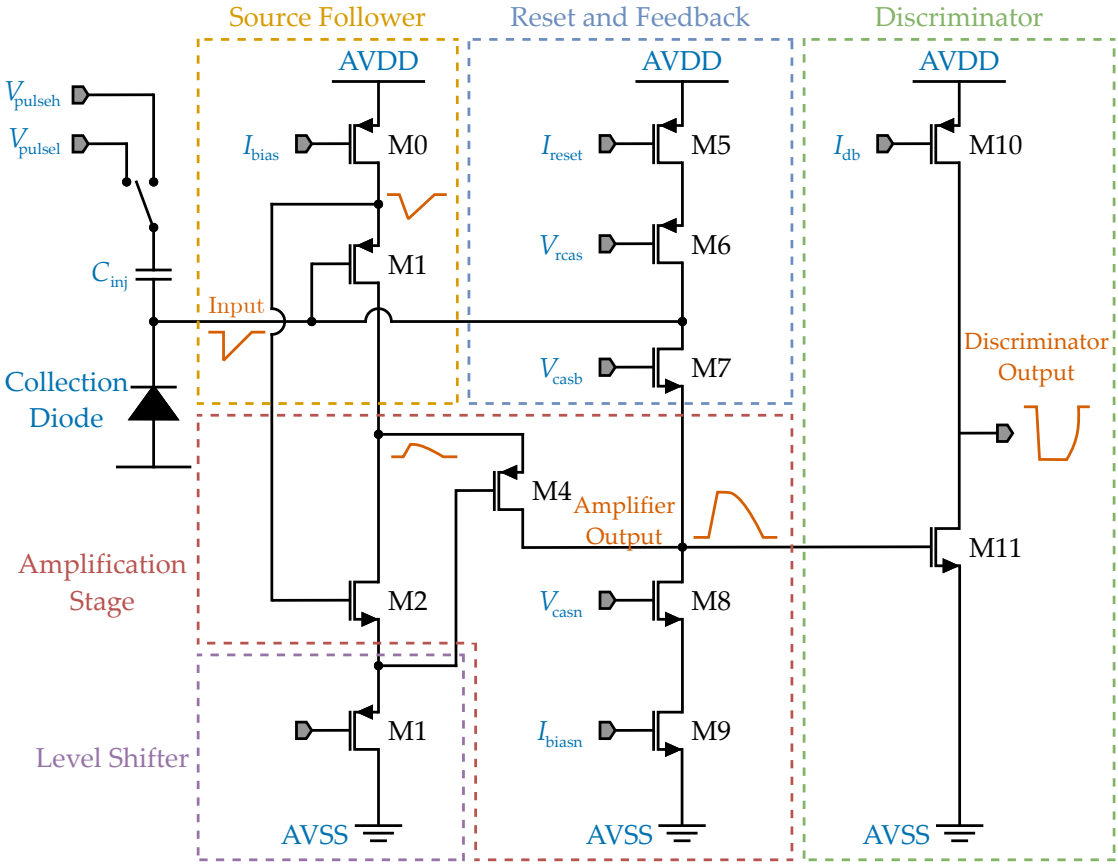

Figure 1.8: Simplified schematic of the in-pixel analog frontend. Control voltages are applied to the gates of the corresponding transistors, while bias currents are provided via current mirrors (indicated as transistors with a current supplied to the gate, e.g., M0). The orange traces illustrate the characteristic voltage signals at key nodes within the frontend circuit. Taken from [26].

pixels, each of which measures 22.5 µm · 22.5 µm, versus 18 µm · 18 µm sized pixels in a 320 · 320 pixel matrix on the bottom. The layout of the active area of the pixel itself follows the modified-with-gap design gap as depicted in Figure 1.3. This results in all the regions being roughly identical in size. Nevertheless, these regions can and mostly are viewed as individual sensors, especially in the analysis, as they can be controlled virtually independently from each other. This is because there are **D**igital **A**nalog **C**onverters (DACs) located at each region (controlling the behavior of those pixels) that can be set individually. This includes the voltages and currents for the analog frontend of each pixel, a simplified schematic of which is shown in Figure 1.8. [19, 26]

A detailed description of the working principle and the development process of the analog frontend can be found in [26] and [28]. Only the parts directly relevant to this work will be highlighted, taken from those sources. The baseline voltage at the amplifier's output is controlled by I_{reset} together with V_{casb}. Among other things, these

Region 0	Region 1	Region 2	Region 3
Standard	Larger input transistor (M1)	Larger discriminator input transistor (M11)	Larger common-source transistor (M2)
Standard	Standard	Standard	Reduced parasitic capacitance

Table 1.9: Frontend variations for the top and bottom HUs within an RSU. Taken from [29].

effectively shift the signal in relation to the discriminator's threshold, in turn influencing the detection threshold, i.e., the sensitivity, of the pixel itself. For self-testing purposes, V_{pulseh} can be used together with V_{pulsel} to inject charges into the frontend by applying a voltage step to the injection capacitance C_{inj}. Thereby, V_{pulsel} corresponds to the AVSS ground net relative to which the V_{pulseh}-DAC generates its voltage. Additionally, the biasing net can be used to apply a reverse bias voltage $V_{\text{psub}} = V_{\text{BB}} = -1.2\,\text{V}$ to the collection diode. Unavoidably, this voltage is also applied to most of the NMOS transistors of the frontend, changing its behavior. To correct for this, the standard biasing can be adjusted to keep the chip operational.

Lastly, it is noteworthy that some of the regions of a babyMOSS have slightly modified layouts of the analog frontend. These changes are noted down in Table 1.9 and were implemented to investigate their effects on the chip's performance. [26, 29]

2 Experimental Setup and Procedure

The investigations in this work are based on two different experimental setups: a testbeam campaign and lab scans. As the first babyMOSSes on an FPC carrier arrived only one week before the testbeam was scheduled, the testbeam was carried out first. Additionally, no bending of the **D**evices **U**nder **T**est (DUTs) themselves was performed before the testbeam; their functionality was only confirmed in the flat configuration. This was done to ensure a true unbent baseline measurement. As the DAQ used the same hardware, the DAQ-raiser test system will be introduced first, including the mechanical mounting jigs used for bending. Afterwards, the integrated setups will be explained and the timelines will be discussed, where the encountered sensor liftoff issues and the attempted mitigations are also mentioned.

2.1 The DAQ-Raiser Test System

The DAQ-raiser test system is comprised of three main parts, the DAQ board, the proximity board, and the babyMOSS carrier, as shown in Figure 2.1. Two functionally identical versions exist for the latter two: the flat version (PCB), and the flexible version (FPC).

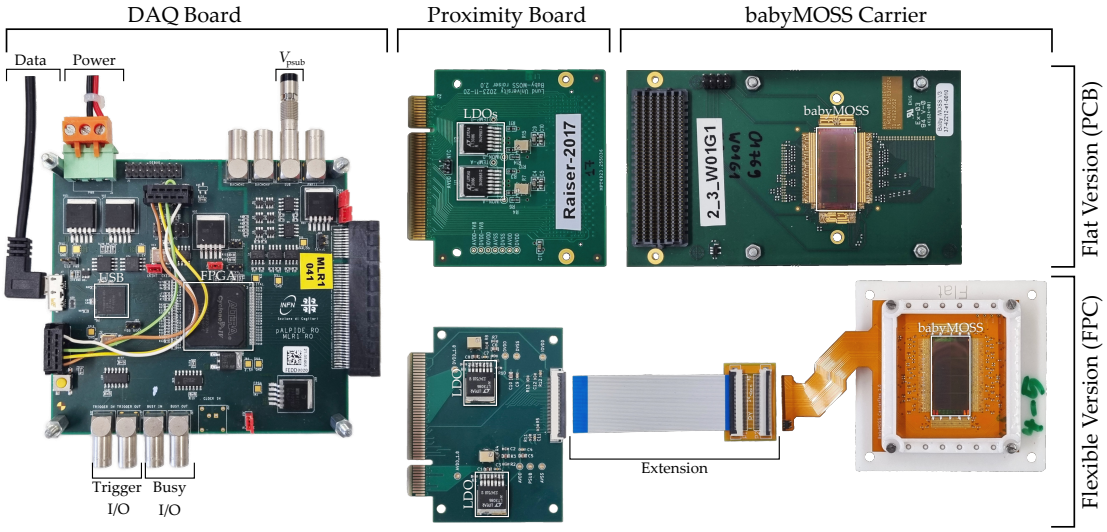

Figure 2.1: Overview of the components of the DAQ-raiser test system, both for the flat and the flexible versions.

The DAQ board is the core component of the setup. It handles all operations and is configurable to work with different DUTs. This is achieved by physically connecting jumpers on the board and programming the **F**ield **P**rogrammable **G**ate **A**rray (FPGA)

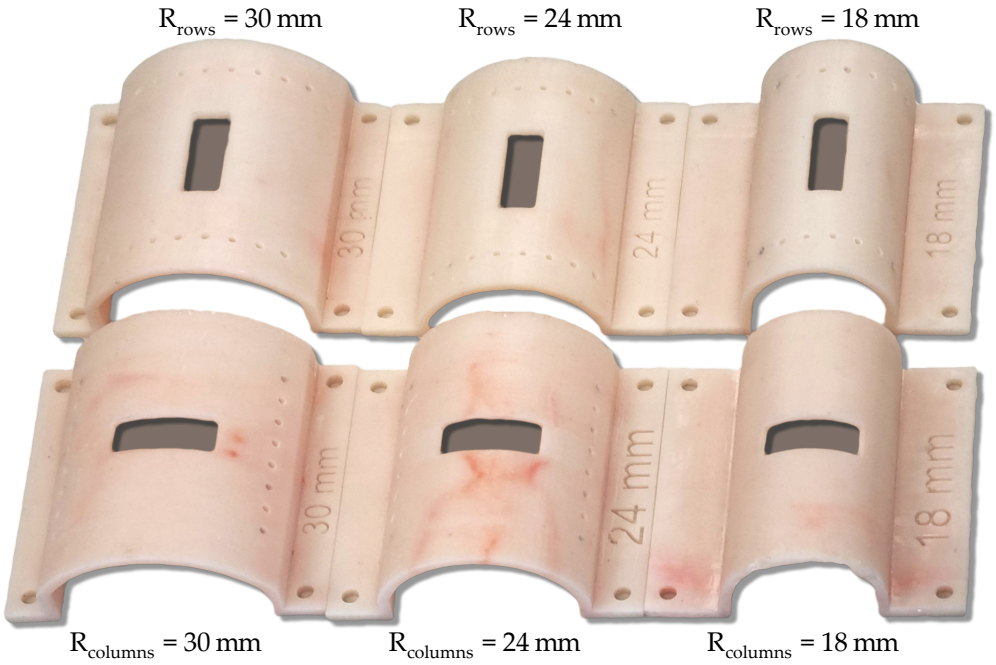

Figure 2.2: Overview of the mechanical mounting jigs used to bend the DUTs to the specified radii. The naming is also indicated.

on startup via the USB connected to a computer that is also used to execute the DAQ itself. As also indicated in Figure 2.1, the DAQ board not only takes in power, which it also provides to the rest of the system, but also the backbias voltage V_{psub}. In Figure 2.1 a $0\,\Omega$ shunt is used to set $V_{\text{psub}} = 0\,\text{V}$, but it can be replaced by a filter board connected to an external power supply to set $V_{\text{psub}} = -1.2\,\text{V}$. The trigger signal can be input into the board and also daisy-chained to connect subsequent boards in a telescope. The same goes for the busy signal, but here the status of the board itself is also transmitted. The proximity board not only serves as an adapter between the data lines of the carrier's and DAQ board's connectors, but also features two **L**ow **D**rop**o**ut Regulators (LDOs). Using trimming potentiometers also located on these boards, the LDOs are tuned to provide the exact AVDD and DVDD voltages of 1.2 V each, which the babyMOSS needs to operate.

The last component is the babyMOSS carrier. As the name suggests, the babyMOSS chip is glued and wirebonded to the PCB or FPC, where some passive components are also located. The flat version is the one commonly used in the characterization of the babyMOSS and its design was used as a template for the flexible version. One advantage of the latter are the connectors. As these are commonly used in electronics, extensions are readily available and were successfully used in different lengths to simplify operations.

Before discussing the bending, there are a few important points to note about the two different versions. The manufacturing process of the PCB version ensures the chip itself has good flatness. The same standard cannot be achieved in the FPC version. As the latter, as well as the corresponding proximity board, were custom-made to ensure flexibility for bending, slight warping can be seen even in the flat configuration. This

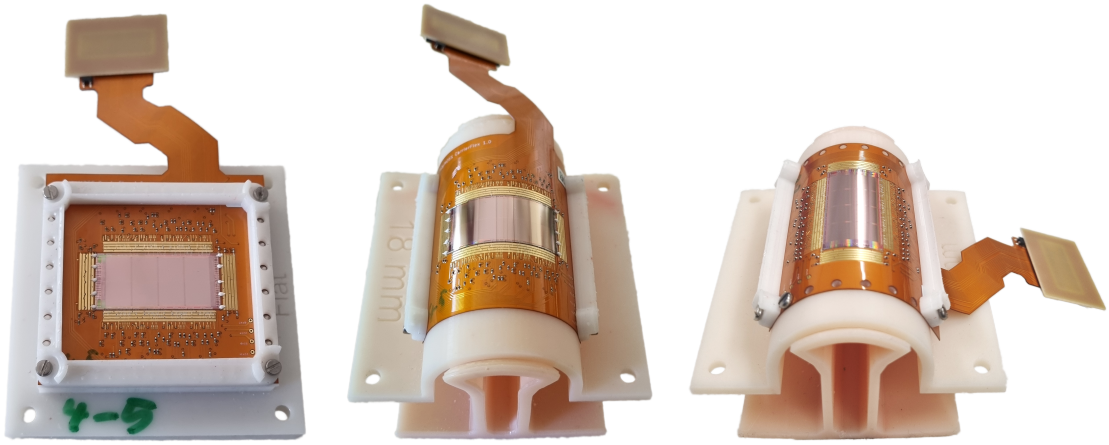

(a) babyMOSS in flat configuration.

(b) babyMOSS bent to $R_{\text{columns}} = 18\,\text{mm}$.

(c) babyMOSS bent to $R_{\text{rows}} = 18\,\text{mm}$.

Figure 2.3: Three examples of babyMOSS bent to different radii through the mounting on corresponding jigs.

is also visible in the reflections of the flat babyMOSS in the middle of Figure 2.8c. Nevertheless, this fact will be mostly neglected in the following, as the effects were deemed insignificant for the presented results. Unfortunately, due to an error, the values of some current sensing resistors on the FPC are off by a factor of five. The effects of this will be discussed in Chapter 3.

As the goal of this work was to study the effects of the bending on the babyMOSSes performance by comparing the DUTs to themselves, their shape had to be changed. This was done by manually bending the FPC carrier and securing it on dedicated mechanical mounting jigs. The radii were chosen in accordance with [30] for easier comparison. These coincide with the originally planned radii for the ITS3, as stated in [24], but not with the current design numbers as stated in [19] and shown in Figure 1.5. Furthermore, the bending in two directions was to be investigated, arriving at the six jigs shown in Figure 2.2, where the nomenclature is also introduced. Figure 2.3 shows the fully assembled jigs for the smallest radii in both directions, in addition to a babyMOSS on its flat jig, which was omitted in Figure 2.2.

2.2 The Testbeam Telescope

The testbeam, which was used to study the efficiency for the varying setups, was conducted at the **El**ektronen **S**tretcher **A**nlage (ELSA) in Bonn, which provided a 2.5 GeV electron beam. As this setup was only parasitic and the main users needed the smallest possible beam spot, some limitations for the analysis arose, which will be discussed in Section 3.2.2.

Determining the efficiency of a detector requires tracking a large number of particles passing through the DUT. This is achieved by placing the DUT between several reference layers, which are used to reconstruct the particle's paths and subsequently determine

the expected intersections with the DUT. Comparing these to the actually registered hits allows for the efficiency to be determined.

Together with a triggering and busy system, these then form a telescope. The one used in this work is shown in Figure 2.5. Additionally, a schematic representation can be found in Figure 2.4, which also features the layer's distances used in the analysis. Apart from the DUT on a FPC[1] in the middle it consists of six flat babyMOSS carriers as reference layers, forming two reference arms up- and downstream of the DUT. Additionally, the telescope featured two scintillators, similarly sized as the babyMOSSes and each connected to a **P**hoto **M**ultiplier **T**ube (PMT), which were used to trigger the telescope's readout on coincidence[2], unless any of the chips were still busy. The aluminum cage of the DUT (visible on the right of Figure 2.5) was removable, so that the DUT could be bent to different radii on site and placed back into the telescope box with minimal effort. The triggering was controlled using a dedicated triggerboard, while the DAQ itself was handled by the EUDAQ2 framework [31] controlling the DAQ boards.

The operating voltages V_{casb} of the reference layers were determined and set. For each bending configuration, the following measurements were conducted in beam:

- An efficiency scan over a range of V_{casb} settings and
- a **T**ime **o**ver **T**hreshold (ToT) scan over a range of I_{reset} settings, which will be required for other works.

Additionally, the following offline scans were conducted without beam:

- A fake hit rate scan over a range of V_{casb} settings, and
- A threshold Scan over a range of V_{casb} settings.

All of these were carried out for $V_{\text{psub}} = 0\,\text{V}$ and for $V_{\text{psub}} = -1.2\,\text{V}$ with an adjusted operating point and accordingly altered V_{casb} range. Their functionality and consequent analysis will be explained in Chapter 3. All regions of the chips were run in parallel in the aforementioned tests. For bending along the columns, especially for the smaller radius, it was noticed that the runs with high V_{casb} settings failed due to noise. Therefore, the scanned ranges were adjusted for the $R_{\text{columns}} = 18\,\text{mm}$ setup. The order of the bending configurations that were used will be explained in Section 2.4.

As previously mentioned, the beam was turned off at times, including at night. Due to the way that ELSA operates, the nightly shutdowns included the whole accelerator complex, making it necessary to adjust the beam spot and size each morning. This was not only time-consuming, but also prevented exact reproducibility of the beam conditions from one day to the next.

[1] Originally there were two DUTs, one of them as backup. As will be explained in Section 2.4, it was necessary after only the first run, which is why the original DUT will be ignored in the following discussion.

[2] This means that both scintillators must have registered a hit in a given timeframe of one another, suggesting that a particle actually traversed the telescope.

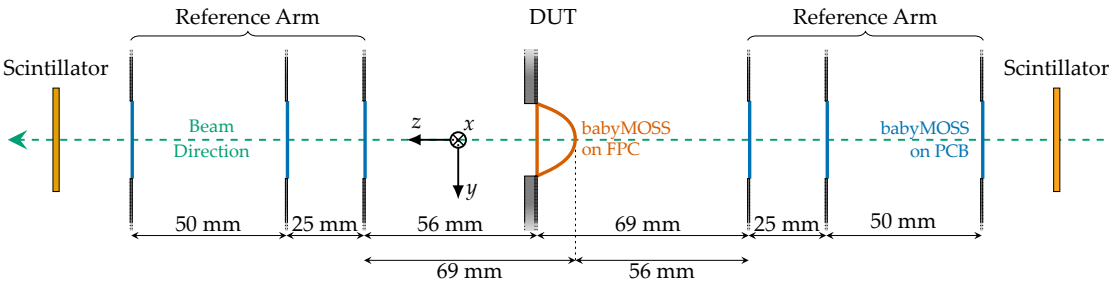

Figure 2.4: Schematic representation of the telescope used in the testbeam. The beam direction is from right to left. The distances in the z-direction have the correct relative proportions, though the rest of the graphic does not. The z-distances are given for the DUT in the flat configuration as well as the bent ones. The graphic follows the design in [26].

Figure 2.5: Photographs of the telescope used in the testbeam. The beam direction is from right to left. The telescope box is shown from the top (top-left) and from the side (bottom-left), where the latter view includes a second DUT that replaced the first after the Flat[1] measurement. On the right, a close-up of the DUT in the $R_{\text{rows}} = 18\,\text{mm}$ configuration is shown mounted inside the telescope.

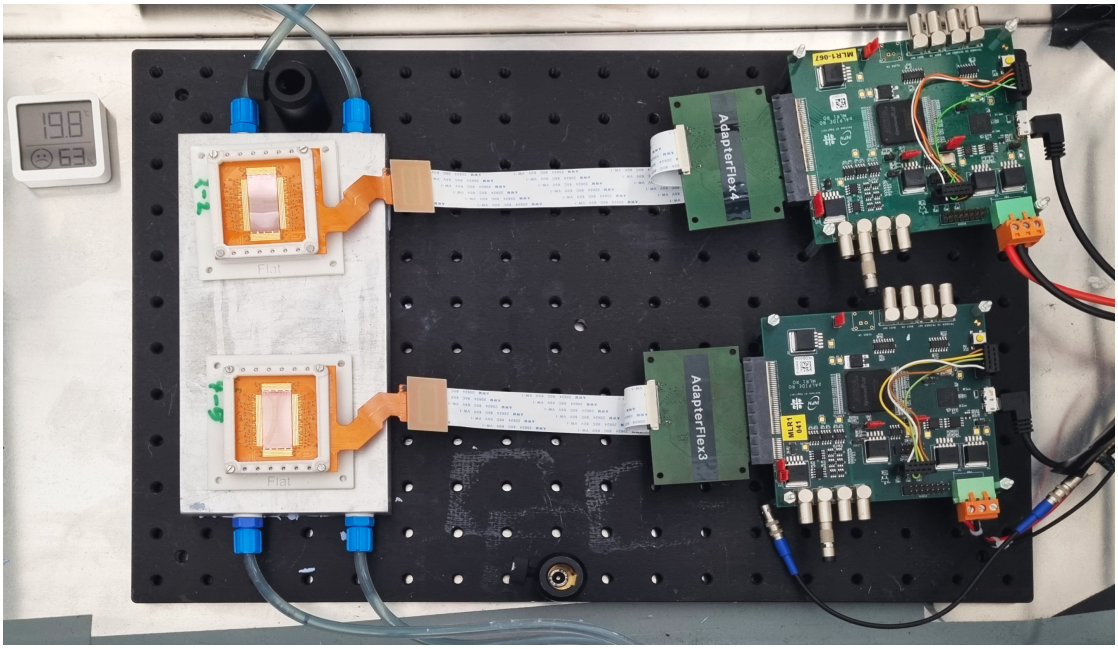

Figure 2.6: TTop-downview of the setup inside the box used in the lab scans.

2.3 The Lab Scans

To confirm the observations of the testbeam and to investigate their occurrence, an even more systematic and complete lab measurement campaign was executed. A picture of the setup, which was located in a box, can be found in Figure 2.6. Here, the following measurements were conducted for each bending configuration:

- a DAC scan,
- a fake hit rate Scan over a range of V_{casb} settings, and
- a threshold Scan over a range of V_{casb} settings.

The scans for $V_{\text{psub}} = 0\,\text{V}$ were run in parallel on both chips. The scans for $V_{\text{psub}} = -1.2\,\text{V}$, however, were only on babyMOSS-4_5_W01G1, the lower one in Figure 2.6. This is due to a known short in babyMOSS-2_2_W01G1, which prevented the usage of backbias. Again, the scans themselves will be explained in Chapter 3. To prevent interference between regions, these scans were conducted region by region, because, for example, if one region is too noisy, the scan would fail for all regions, even though only one of them exhibited problematic behavior. For this, the babyMOSSes on their jigs were placed on a heat exchanger that was connected to a chiller set to 14.0 °C. The air temperature was monitored through a small thermometer at the top left of Figure 2.6. The cables and cooling tubes were routed to the outside on the right and bottom, respectively.

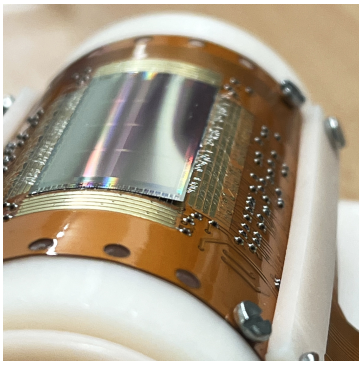

(a) Liftoff after the $R_{\text{rows}} = 18\,\text{mm}$ run.

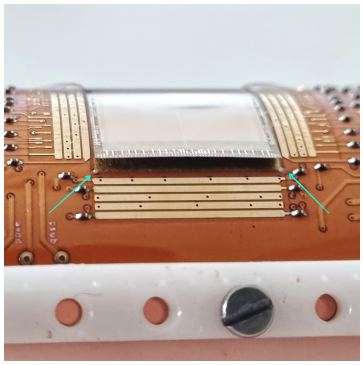

(b) Liftoff after the $R_{\text{columns}} = 18\,\text{mm}$ run. The original glue spots are indicated.

(c) Liftoff after the $R_{\text{columns}} = 18\,\text{mm}$ run, at an alternate angle.

Figure 2.7: Liftoff at the testbeam (a) and in the labscans (b) and (c).

2.4 The Full Timeline

In this section, the sequence of the events in the lab scans as well as the testbeam will be outlined. As the liftoff problems are closely connected to the timeline, these will be discussed hand in hand. A schematic overview of both timelines, including the relations of the testbeam to the lab measurement campaign, can be found in Figure 2.9, where the numbering of the multiple flat configurations is established as well.

2.4.1 Testbeam

The testbeam started out with the baseline measurements of two babyMOSS DUTs on FPC carriers in parallel. Since the plan was to bend only one of them, the other served as a backup.

After completing the Flat[1] setup, the first DUT was successfully bent into the $R_{\text{columns}} = 30\,\text{mm}$ configuration and mounted back into its cage. During the installation back into the box, the assembly tipped onto a PMT's holder in such a way that a hole was punched into the silicon sensor itself. The first DUT was rendered inoperative by the damage and the backup was needed. This is the sensor mentioned in Figure 2.9, which was subsequently successfully installed in the $R_{\text{columns}} = 30\,\text{mm}$ configuration.

Since the removal and re-mounting of the DUT seemed to pose significant danger to its well-being, as the aforementioned accident showed, it was decided to instantly go to the extreme radius, $R_{\text{columns}} = 18\,\text{mm}$, skipping the medium setting $R_{\text{columns}} = 24\,\text{mm}$.

When opening the telescope after completing the measurements for this setup, it was noticed that the chip had lifted off from the adhesive tape holding it in place on the FPC. Unfortunately, there are no good pictures of this available, but it looked similar (though not quite as extreme) as the liftoff observed in the lab scans, which can be seen in Figures 2.7b and 2.7c. As the plan originally included a flat scan after the bending, it was decided to return the chip back to the flat configuration. After this, the chip still did not sit flush against the FPC as it had at the beginning. With limited resources and a short timeframe, the chip was carefully bent in the reverse direction, relying on the

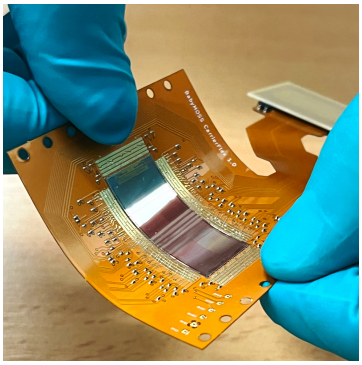

(a) Bending in the reverse direction to press the chip against FPC.

(b) Tweezers with silicon rubber tip.

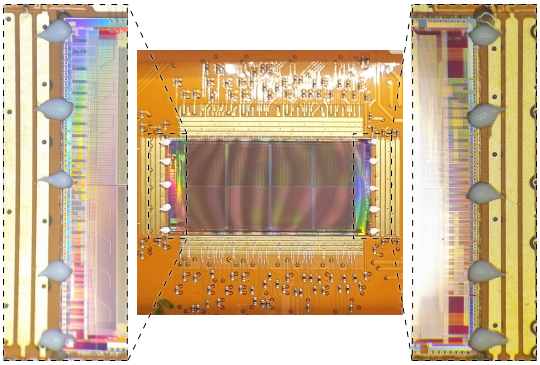

(c) Addition of non-conductive glue to the short sides to prevent further liftoff. Main part of the FPC with enlarged glue points.

Figure 2.8: Different approaches to solve the liftoff problems at separate occasions.

silicon chip's own stiffness to push it back against the tape. This remedy is shown in Figure 2.8a and was adequate at the time, and so the Flat[2] measurement was executed.

For bending in the row direction, liftoff was still considered to be a possibility, but the hope was that the probability of it occurring would be smaller. The reasoning was that the chip was now bent along the shorter direction, which meant less adhesive force would be needed to keep the chip bent. Nevertheless, the smallest radius was deemed the most interesting setup to be executed first, because, if no liftoff occurred, the larger radii could be measured afterwards. Following this consideration, the DUT was put into the $R_{\text{rows}} = 18\,\text{mm}$ configuration.

Unfortunately, after extracting the DUT liftoff could be observed again, as depicted in Figure 2.7a. Following the same procedure as after the earlier liftoff, the DUT was returned to a flat configuration (Flat[4]), concluding the testbeam. Due to time constraints, the offline scans were not executed on site but were instead performed using the lab scan setup at a temperature matching that of the testbeam area after this campaign finished.

2.4.2 Lab Scans

The general idea behind the lab scans was similar to the testbeam: bend the babyMOSSes to different radii and record the same data for each bending configuration. In an effort to prevent liftoff here, small glue droplets were added on the corners of the babyMOSSes to provide additional support. These were not fully effective, as can be seen in Figure 2.7b.

As two babyMOSSes on FPC carriers were produced as DUTs, it was decided to run them in parallel for the $V_{\text{psub}} = 0\,\text{V}$ measurements. As explained before, the $V_{\text{psub}} = -1.2\,\text{V}$ measurements were only executed for one of them – depicted in the top row of Figure 2.9. To exclude any correlations caused by bending in one direction prior to the other, one babyMOSS was bent first along the column direction while the second was bent along the row direction.

Accordingly, after a baseline measurement, the DUTs were bent to a radius of 30 mm, then 24 mm, and finally 18 mm in their respective direction. When the box was opened

for a cable change to run the $V_{\text{psub}} = -1.2\,\text{V}$ setting, liftoff was observed again for the babyMOSS, which had been in the $R_{\text{columns}} = 18\,\text{mm}$ configuration. This setting was therefore skipped, both chips were returned to flat, and the testplan continued with two flat measurements: Flat^2 and Flat^3, separated by a 24 h rest period. This was done to determine if relaxing the chips after bending had any effect.

In the meantime, strategies to combat the liftoff were developed. Instead of relying on bending the DUT in the reverse direction, tweezers with a small piece of silicon rubber on the tip were successfully tested on a mechanical dummy, carefully pushing the chip against the tape. Additionally, non-conductive silicon rubber was tested as reinforcement of the tape on the short sides. This was feasible, as the babyMOSSes were only bonded to the FPC on the long sides. The chips were supposed to be bent to a radius of 30 mm, now along the other direction, shortly after the glue-testing samples had been produced. As their glue was not cured, their feasibility could not yet be estimated.

It was decided then to proceed without gluing, as the largest radius seemed not as problematic after the experience gained in the testbeam. Thus, both chips were and the measurements executed without any liftoff problems.

As these were finished, the glue-testing samples were positively evaluated and five glue droplets were added to each of the short sides of both DUTs, as shown in Figure 2.8c. After one more day of curing the glue on the DUTs, the measurement campaign was continued where it had left off. The two babyMOSSes were bent to radii of 24 mm and 18 mm before executing three more flat measurements. Noteworthy here is that for Flat^6 the $V_{\text{psub}} = -1.2\,\text{V}$ scan was skipped as no one was available to change cables in the lab setup. At the end, the missing $R_{\text{columns}} = 18\,\text{mm}$ configuration at $V_{\text{psub}} = -1.2\,\text{V}$ was also done, after which the offline scans for the Flat^4 configuration of the testbeam were conducted.

It is also worth noting that, apart from the accident at the testbeam, all babyMOSSes remained fully functional after the measurements executed for this work.

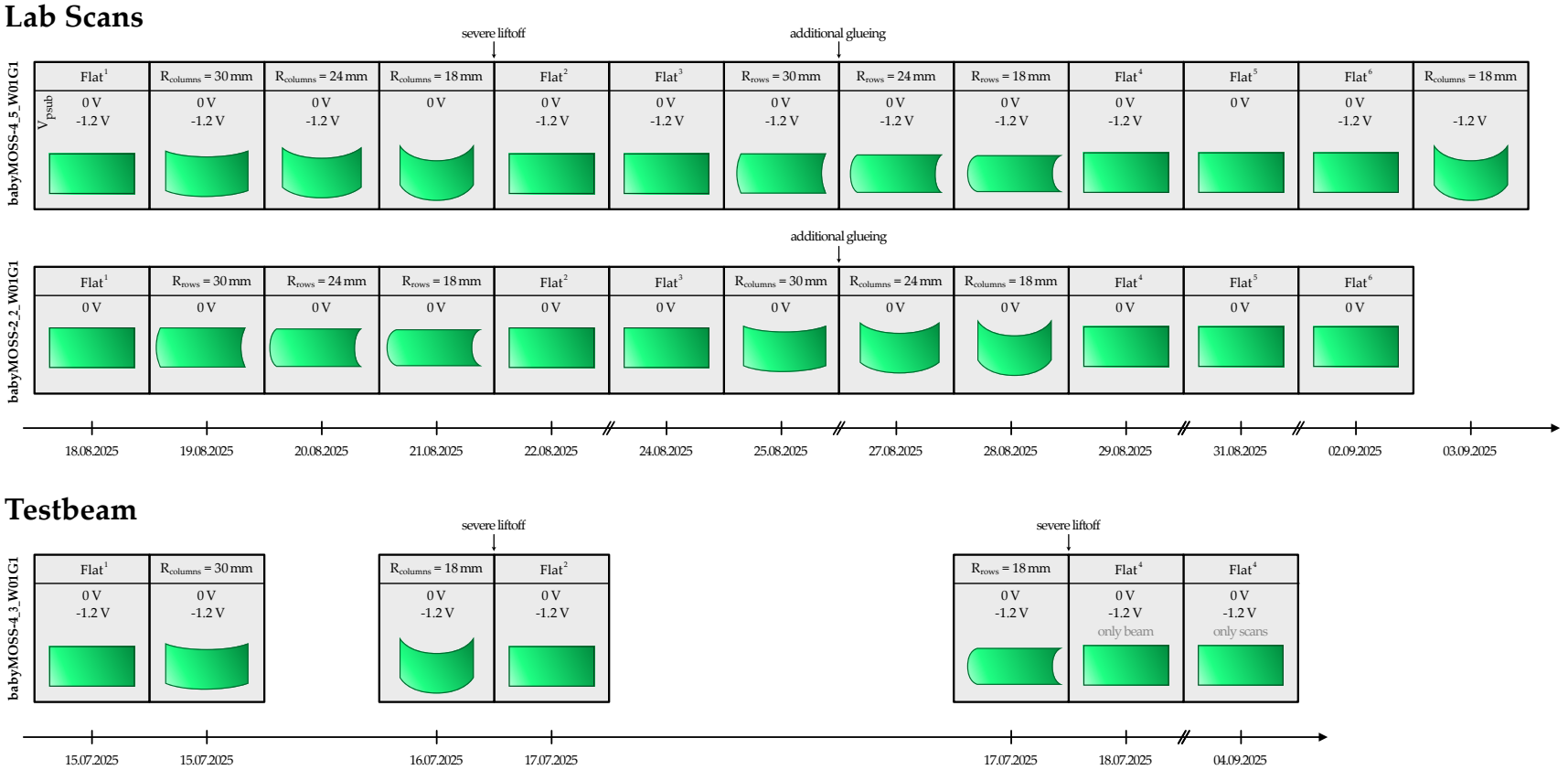

Figure 2.9: Overview of the timeline of the different setups with pictograms in the lab scans, as well as the testbeam for each chip. The names, which will identify the setups in the following, can be found at the top of each cell. The cells are aligned according to their radius, while the dates are indicated below. Importantly, the numbering of the different flat configurations is introduced here. The occurrences of the liftoff as well as the gluing are also indicated.

3 Analysis

In this chapter, the analysis pipelines for the different scans will be discussed, i.e., how the data itself is obtained and how the relevant quantities are extracted. The finished plots themselves will be introduced and subsequently discussed in Chapter 4. First, a quick overview of the offline scans is given, after which the analysis pipeline for the efficiency measurements from the testbeam will be explained. As the bent geometry of the chips themselves is relevant for the data analysis in the latter case, a few modifications to the analysis software used, namely EUDAQ2 and the **Corry**vreckan framework (corry), had to be made. Therefore, these changes, including their motivation and challenges, are presented before the full pipeline is introduced.

3.1 Offline Scans

The offline scans are self-tests of the babyMOSS, where several of the chip's functionalities can be tested with only the DAQ-Raiser Test System. The software package responsible for executing these scans, as well as their analysis, can be found at [32]. The following descriptions are based on the code found there, as well as [26].

3.1.1 DAC Scan

A DAC scan tests the in-chip DACs responsible for providing the biasing for the analog frontend of the pixel, cf. Section 1.5 and Figure 1.8. This is done by measuring the current or voltage output for each of the 256 DAC settings, which are the digital input for the DACs. As designed, this results in a linear relation, which is slightly different for each region of the babyMOSS. Two examples of this, namely for V_{casb} and I_{bias}, can be found in Figure 3.1. For the use in conversions and easier comparison between the different bending configurations, this linear dependence can be fit according to

$$\text{Output} = m_{\text{quantity}} \cdot \text{Setting} + t_{\text{quantity}}, \tag{3.1}$$

where quantity is one of V_{casb}, V_{casn}, V_{pulseh}, V_{shift}, I_{bias}, I_{biasn}, I_{db}, or I_{reset}. Subsequently, m_{quantity} and t_{quantity} will be compared in Chapter 4.

3.1.2 Fake Hit Rate Scan

The fake hit rate describes the probability that a pixel will register a hit even when no physical particle crosses it. For this, the pixel matrix (or only a predefined part of it) is read out a certain number of times n_{triggers} in the absence of a radiation source. Then, the total number of registered hits N_{hits} is counted. The resulting fake hit rate (fhr) is

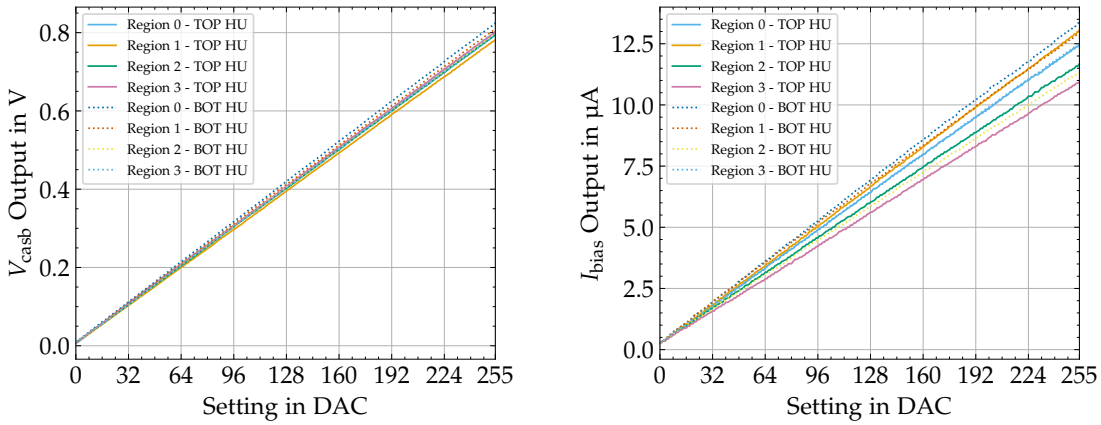

Figure 3.1: Exemplary raw data obtained by the DAC Scan: Output plotted against the DAC Setting, for V_{casb} on the left and I_{bias} on the right. See text for details.

then also normalized to one pixel by dividing by the total number of read out pixels n_{pixels}

$$\text{fhr} = \frac{N_{hits}}{n_{triggers} \cdot n_{pixels}}.$$

The contribution of noisy pixels to N_{hits} can be removed by masking them if the probability of them firing is higher than a predefined frequency threshold.

One fake hit rate scan itself is executed for a fixed operating point. In the testbeam and the lab scans, the scan was repeated multiple times while changing the V_{casb} and V_{psub} in between, the results of which are shown in Chapter 4.

Due to time constraints in the testbeam, $n_{triggers} = 100\,000$ was chosen for the scans conducted there. Due to the unsatisfactory statistical significance, this analysis was only used as a consistency check. Therefore, the masking was disabled.

In the lab scans, $n_{triggers}$ was increased by a factor of 10 to 1 000 000 in an effort to obtain higher statistical significance. After testing multiple values, a value of $0.8\,\text{trigger}^{-1}$ was selected as the frequency threshold.

3.1.3 Threshold Scan

This scan is used to determine the effective discrimination threshold applied by the entire analog frontend (as introduced in Section 1.5 and Figure 1.8) to the signal from the collection diode. For this, the injection capacitance is utilized to inject a fixed amount of charges determined by V_{pulseh} into the frontend and observe the pixel's response. These injections are repeated for 25 times for each V_{pulseh} setting, and the number of registered hits is counted. This results in a characteristic s-shaped curve (s-curve), as depicted in Figure 3.2a, the shape of which follows a Gaussian error function [33]. The mean and standard deviation of the derivative of the s-curves define the threshold and noise of each pixel, respectively. For a given operating point, these then form a distribution over the scanned pixels, an example for which can be seen in Figure 3.2b. The mean value of the threshold distribution is then considered the threshold for the whole matrix and the relevant quantity used in the following.

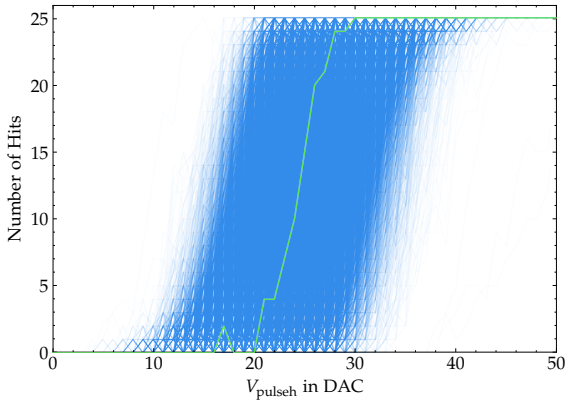

(a) Number of hits plotted against V_{pulseh} for all the pixels in one region resulting in the s-curves. A representative s-curve of a single pixel is also highlighted.

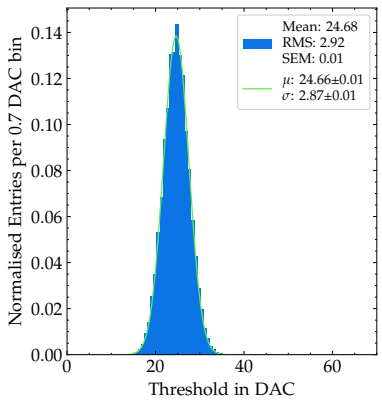

(b) Distribution of the threshold values of all the pixels in one region plotted together with a Gaussian fit.

Figure 3.2: Exemplary raw and processed data obtained by the threshold scan.

As for the fake hit rate scan, one threshold scan itself is executed for a fixed operating point and was also repeated over a range of V_{casb} and V_{psub} values. In the testbeam and the lab scans, the whole pixel matrices were usually scanned, except for the $R_{\text{columns}} = 18\,\text{mm}$ configuration in the testbeam. There, due to time constraints, only 1 in 10 rows were enabled, still yielding usable data.

3.2 Testbeam – Efficiency

As mentioned earlier, the determination of the efficiency of a sensor requires the reconstruction of particles crossing the **R**egion **O**f **I**nterest (ROI) of the DUT and the subsequent comparison to the data recorded by the DUT itself.

For this, corry [34] is typically employed, as also done in this work. The analysis pipeline is divided into multiple steps, each with a specific task. These are just differently configured runs of corry all following a general scheme. First, the captured data is loaded and related to the corresponding physical setup. For this, a geometry file is provided specifying the sensors to be loaded, including their role[1], their position, and their properties. As EUDAQ2 was used for the DAQ, the corresponding event loader in corry was utilized. This in turn uses the StdEventConverter included in EUDAQ2 to transfer the hits on the relevant layers into corry. After clustering[2], the hits' positions in 3-D space are calculated and provided to the rest of the modules used in this run. These, in turn, handle the core computations, i.e., tracking, alignment, and analysis, and their results are saved as output. Apart from the plots generated by the modules used to evaluate their performance and serving as the final results, updated masks and updated geometry files can be generated in the masking and alignment steps.

[1]This is used to determine the singular reference detector used in the alignment, the DUT itself, and more, which is not relevant in this work.

[2]This step combines neighboring pixels firing at the same time into one singular hit with an adjusted position.

These updated files are then typically passed on to the subsequent steps in the analysis pipeline.

Before explaining the specific analysis pipeline used in this work, the adaptations to the software to accommodate for the specific requirements will be discussed. The resulting forks of EUDAQ2 and corry can be found at [35] and [36], respectively.

3.2.1 Software Modifications

The Compound Regions

As explained in Section 1.5, a babyMOSS consists of eight individual pixel matrices, or regions, four of which are located on the top while the rest are located on the bottom. From an analysis point of view, the regions only differ in pixel size and are therefore identical in the top and bottom HUs, respectively. As can be seen in Figure 3.3, these regions are not located next to one another but are separated by a dead area. These dead areas are identical within one HU but differ between them. Additionally, there is a small vertical gap between both HUs.

The original version of corry treats all these regions as individual sensors. Furthermore, there is no way to apply constraints between two sensors or to combine multiple sensors into a superstructure. This would not only be useful for streamlining alignment, as the entire area of the physical sensor could be utilized, but would also be helpful for the bent geometry introduced below, as the bending is applied to the entire sensor, not

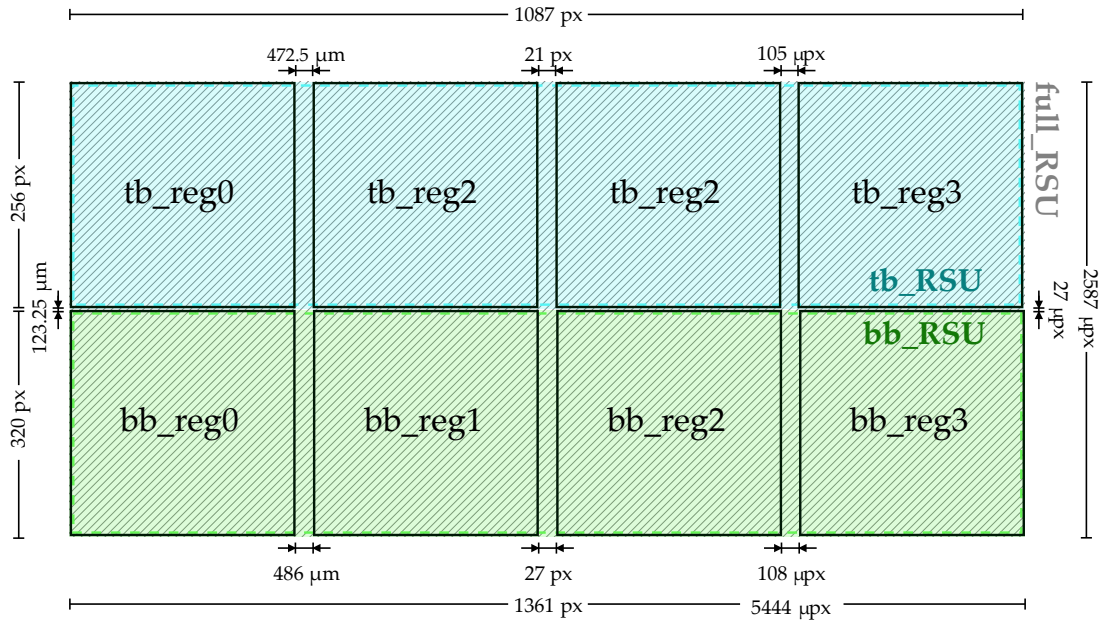

Figure 3.3: Schematic representation of the eight individual regions of a babyMOSS and the three compound regions as seen by corry. The physical dimensions of the chips taken from [29] as well as the sizes of pixel matrices are indicated. Note that the pixel size is different for the upper and lower regions, as indicated in Figure 3.4. The shaded area and the sizes given in µpx correspond to the full_RSU

to the regions individually.

Implementing constraints between sensors or such a superstructure would entail a substantial change to corry's core framework; therefore, it was decided to employ a workaround instead. The StdEventConverter was modified to present corry with a total of three compound sensors that represent the physical shape by artificially creating larger sensors encompassing the individual regions. Then, the hits of the individual regions will get placed at the corresponding offset positions in the larger sensor. Creating these for both HUs was straightforward. When examining the distances between the regions, as provided in [29], it was observed that these values were perfect multiples of their respective pixel pitches. Therefore, the tb_RSU and bb_RSU are effectively just a long version of their respective first region, where the x-coordinates of the hits in the other three regions are offset by the right amount to depict the physical shape of the chip. This can be seen in Figure 3.3 as well.

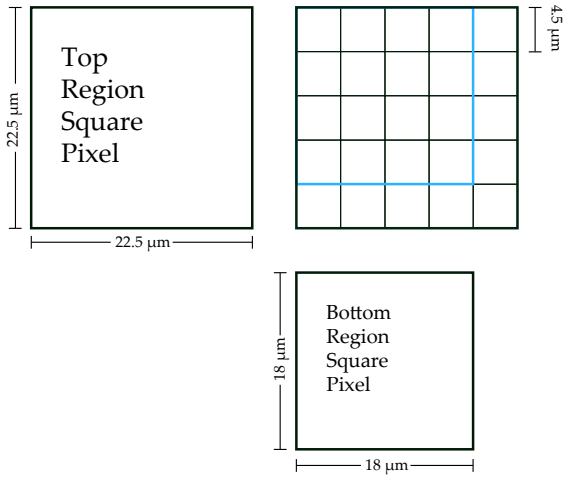

Figure 3.4: Schematic representation of the oversampling processes used for the implementation of the full_RSU.

Integrating all eight regions of both HUs together proved to be more difficult. The main challenge was the difference in pixel pitch: 22.5 µm for the top regions and 18 mm on the bottom. The problem arising from this is that if only one of the pitches is used, the other pixel edges cannot be mapped exactly. This would entail a change in shape and the offsetting of the cluster positions by an amount varying pixel to pixel that is on the order of 10 µm in the worst case. As a solution, oversampling was employed as depicted in Figure 3.4. There, the pixel pitch of the corresponding compound sensor – the full_RSU – is reduced to 4.5 µm, forming small pixels called micro pixels (µpx). This enables it to map the edges of the original sensors one-to-one. If a hit in one of the top or bottom regions is registered, the corresponding 5 µpx · 5 µpx or 4 µpx · 4 µpx area is activated. After applying clustering, the correct positions are retrieved.

All three compound sensors were successfully tested in corry. The individual sensors can thereby be recovered by either selecting an appropriate ROI or by replacing them with the individual sensors placed at the correct position. The full_RSU has three main drawbacks:

Firstly, the distance between the two sensors cannot be mapped exactly; an error of 1.5 µm still remains. If the top and bottom HUs of the telescope are roughly aligned, as they usually are, this has little to no effect. However, this can be problematic when using mixed setups or for large vertical offsets.

Secondly, the sensor parameters cannot be varied across the entire region of the full_RSU. For example, the pixel pitch must be set to 4.5 µm to accommodate oversam-

pling, rather than the physical values, and the intrinsic spatial resolution of the pixel can only be set to a single constant value. If these are not relevant for the modules used in the analysis, for example, if the layers are only for straight-line tracking, this is not problematic.

Lastly, the significant increase in the number of pixels can negatively impact the computational performance. Experience with the full_RSU shows, though, that a tradeoff between this and an increase in the pipeline's efficiency must be considered.

In total, the full_RSU must be used with caution in the analysis. Nevertheless, excellent use of it can be made in testbeam operations, e.g., to produce hitmaps (see e.g. Figure 3.8) for the alignment of the telescope or beam, as well as quick studies of the telescope's performance.

Then again, the tb_RSU and bb_RSU do not suffer from these three drawbacks. Due to this and the beam conditions, which will be explained in Section 3.2.2, the bb_RSU will be used in the following.

Reimplementation of cartesian_bent

This modification to corry is the most directly relevant one to this work. Its purpose is to describe the bent geometry of the DUT by the definition of a new coordinate system, named cartesian_bent, which transforms the local (row and column) pixel positions onto a cylinder of a given radius and direction. Fortunately, it was not necessary to begin the work from scratch. For bent ALPIDE testbeams [30], this had already been implemented and was available. However, this was last updated in 2022 and was unable to work with the current version of corry due to breaking changes introduced to its core since then.

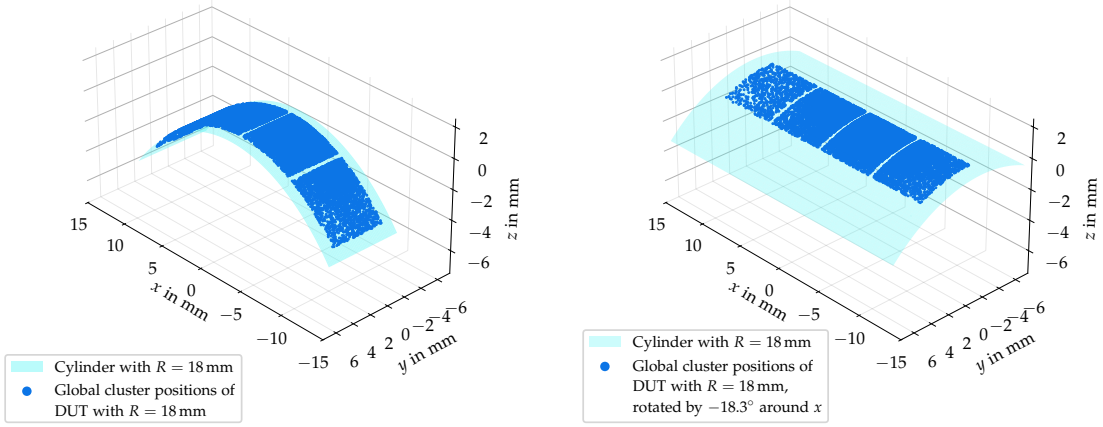

(a) Bending along the column direction.

(b) Bending along the row direction.

Figure 3.5: Cluster positions using the cartesian_bent coordinate systems, for two directions.

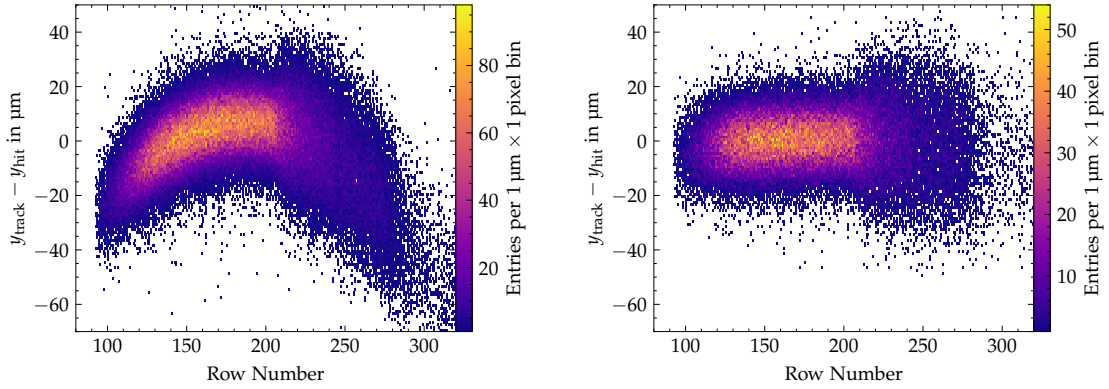

(a) After the DUT alignment *without* the adjusted initial condition.

(b) After the DUT alignment *with* the adjusted initial condition

Figure 3.6: Distribution of the y-residuals plotted against the row number.

For this work, the code was adapted and manually patched; the result of this effort can be found at [36]. To confirm that this coordinate system works, some cluster positions were plotted together with a cylinder of expected radius and direction, which is depicted in Figure 3.5.

The bending along the columns, cf. Figure 3.5a, behaved as expected, having the flat part in the middle of the sensor, which is also the center of all transformations in corry.

The bending along the rows, cf. Figure 3.5b, also worked immediately after the implementation, but behaved slightly differently. This is due to the fact that the flat part of the bending is at the upper edge of the bb_RSU, i.e., the side with the highest row number[3]. Thus, the sensor needs to be rotated by 18.3° to correspond to the expected physical configuration, as indicated in the legend of Figure 3.5b.

To illustrate the importance of this rotation, the alignment of the $R_{\text{row}} = 18\,\text{mm}$ DUT configuration will be discussed as a forward reference. In general, one needs to provide an initial guess for the alignment algorithm, which then optimizes the distribution of the track residuals to obtain an accurate position and rotation. The algorithm used for this task is described in [34] as fairly robust against initial misalignment. When not correcting for the 18.3° rotation, the algorithm converged, although it only reached a local minimum, i.e., the alignment was not successful. This can be seen in Figure 3.6a, where the y-residuals show a clear correlation to the rows. When using the adjusted initial guess with the 18.3° rotation, the alignment succeeded without problems, as seen in Figure 3.6b.

Residual versus Angle Correlations

The last modification is technically the simplest, although it was key in making the analysis possible. After the alignment of the reference layers, the first DUT was to be aligned. However, its alignment could not reach the desired and expected level.

[3]The rows increase with y, which is why the chip's upper edge referenced in the text is the lower one in Figure 3.5a.

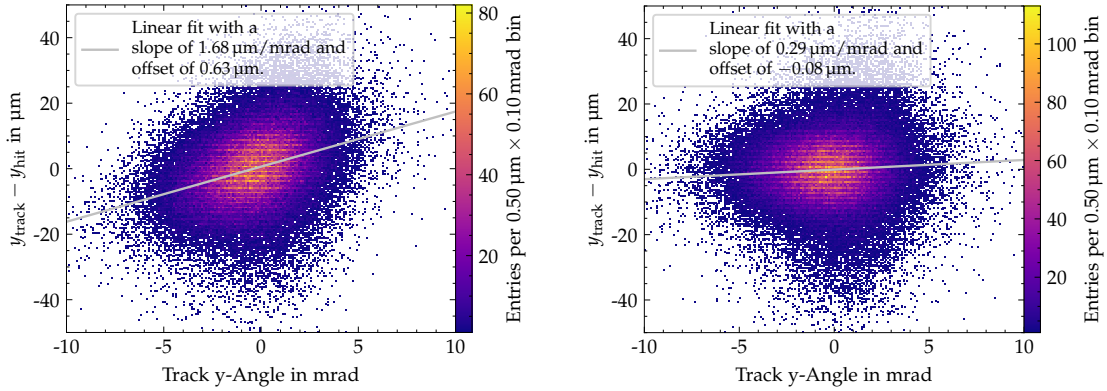

(a) The DUT at the initial z position based on the available data.

(b) The DUT at a corrected z position based on the other plot.

Figure 3.7: Residuals in y plotted against the track angle in two cases.

To investigate this, new plots were introduced, correlating the residuals to the track angle, i.e., the angle of the track to the normal of the sensor's surface. These showed a correlation as depicted in Figure 3.7a. This not only confirmed that the z-coordinate provided in the geometry, which cannot be automatically aligned, was slightly off, but also offered a way to estimate the error. From a simple geometric argument, an additional offset of 1.66 mm could be inferred to the initial z-position, the result of which can be seen in Figure 3.7b. This finally yielded an alignment that was deemed acceptable, as discussed in Section 4.4, and the analysis could be continued.

It is also noteworthy that the distances given in Figure 2.4 are the corrected ones. The reason for this offset was determined to be that the schematics of the assembly used to hold the DUT were not fully accurate[4].

3.2.2 The Full Pipeline

Before discussing the used corry pipeline in more detail, it is sensible to consider the limitations caused by the beam conditions. There are two main factors contributing to this, which have already been mentioned in Chapter 2, but will be repeated here.

Firstly, the beam spot was fairly small at the main users' request, as can also be seen in Figure 3.8. Additionally, the beam itself had to be realigned daily. This meant that, in total, only two regions received sufficient statistics for an efficiency analysis across all setups, namely regions 1 and 2 of the BOT HU. In Figure 3.8 the ROIs used for the analysis are shown as examples. The size and position of these were similar in the other setups and were substantially influenced by small shifts in the mounting of the reference layers in relation to one another. The reason for this is that the tracking requires hits on all reference layers, effectively requiring all active areas to be aligned to form tracks.

[4]These could not be measured as the telescope box had to remain at the testbeam site due to radiation safety, and was therefore not accessible.

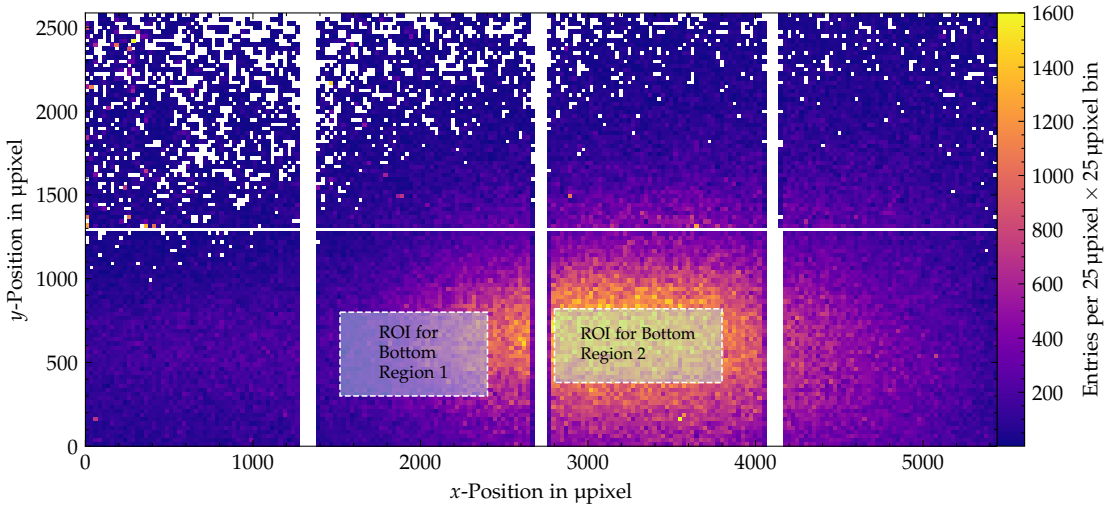

Figure 3.8: Hitmap of the DUT in the Flat^2 configuration, where also the ROIs used in the analysis are indicated. The hitmap was generated using the full_RSU.

The general idea of the pipeline was to perform the masking and alignment of the telescope for one intermediate V_{casb} setting with $V_{\text{psub}} = 0\,\text{V}$. The masks and alignment were then applied to all the V_{casb} and $V_{\text{psub}} = 0\,\text{V}$ settings to perform the analysis. An overview of the ten total steps of the analysis pipeline is provided in Figure 3.9, which also outlines the essential module parameters. In the following, only the most important points will be mentioned.

The analysis pipeline starts with standard masking and prealignment steps. Then, a total of five steps is dedicated to aligning the reference layers only. For each of these, tracking is performed and given to the AlignmentMillipede module, which iteratively optimizes the layer's positions and rotations utilizing the residual distributions. From one step to the next, the accuracy requirements are increased, ultimately delivering optimal alignment after the fifth. After this, only two iterations of the DUT alignment are performed. These are enough, as only one DUT itself is aligned, leaving the references unchanged, and the algorithm converges after only one iteration. The alignment obtained from these steps is then used for the analysis step. Using a radius of 50 µm to associate the hits on the DUT to an intersecting track and requiring a maximum $\chi^2/\#\text{ndof} = 3$, the efficiency is obtained for each ROI. This last analysis step is then repeated for all other V_{casb} and V_{psub} values.

The alignment and efficiency results will be discussed in Chapter 4, although no statement about the spatial resolution will be made.

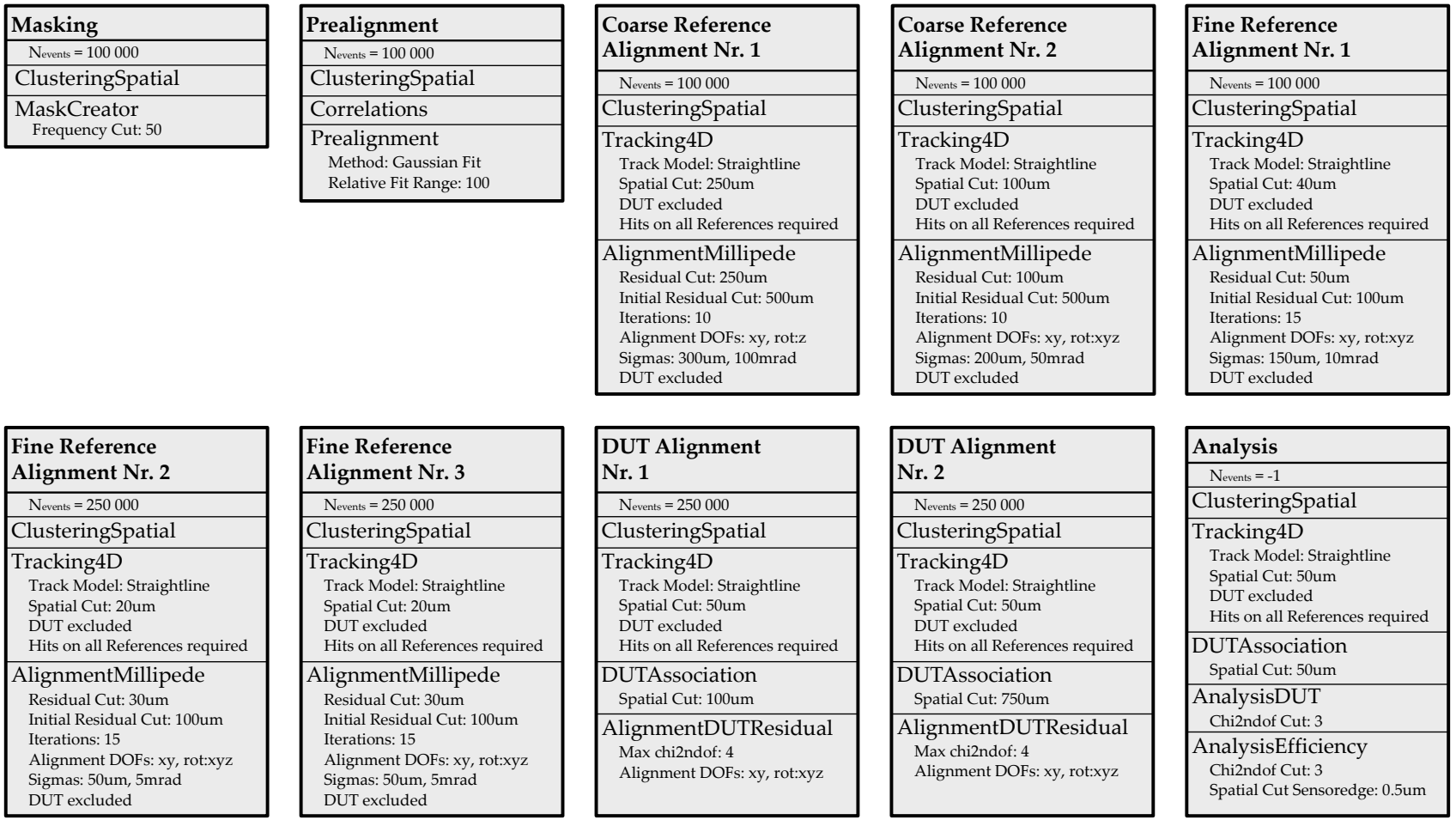

Figure 3.9: Overview of the ten steps of the analysis pipeline, including the important parameters.

4 Results and Discussion

The results obtained in this work will be presented and discussed in the following sections.

It shall be noted here that the order is switched in regard to the execution, i.e., the offline scans will be discussed first. After this, the quality of the alignment is assessed before finally presenting the effects on the efficiency.

Generally, for the offline scans, the main points will be introduced for only one region or HU as an example. All the plots can be found in Appendices A and B, where they are ordered by their chip ID, and a list of the figures is given at the beginning of each chapter.

4.1 DAC Scans

Plotting the deviations of the slope (m) and the offset (t) to the ones of the Flat[2] configuration[1], for all bending configurations results in figures such as 4.1. As explained in Section 3.1.1, these are the relevant quantities extracted from the DAC scan. The plots are produced for each HU and V_{psub} setting individually, but the behavior of all four regions is depicted. The absolute values used for the normalization are also indicated.

Systematic deviations are visible in the slope. All the different flat configurations lie together in a small spread around zero, whereas a definite decrease can be seen for the $R_{\text{columns}} = 30\,\text{mm}$ configuration, which increases for subsequent radii, i.e., tighter bending. A similar hierarchy can be observed for the bending configurations along the rows, although the initial value for $R_{\text{rows}} = 30\,\text{mm}$ lies above the spread of the flat configurations. As the magnitude of this deviation is smaller than the one seen for the column radii, the other configurations cross the spread of the flat configurations for decreasing radii, such that the value for $R_{\text{rows}} = 18\,\text{mm}$ lies below zero.

The general shape is also applicable to all other DACs and setups, albeit with two major limitations. Firstly, the spread of the configurations in comparison to the systematic deviations is sometimes observed to be less consistent, such as in Figure A.2.1. Secondly, it is also observed that for the current DACs, the hierarchy in the row configurations is reversed, although the magnitude of the changes is even smaller. Nevertheless, the shape is fairly consistent between the same DAC type, i.e., currents or voltages, in the same chip and setting.

The last observation also holds for the offset. However, the shape of the curves in the plot differs substantially between the different chips, backbias settings, and DAC

[1] This was chosen instead of Flat[1], as its DAC scan failed for babyMOSS-4_5_W01G1 with $V_{\text{psub}} = 0\,\text{V}$ and to ensure good comparability to the other setups.

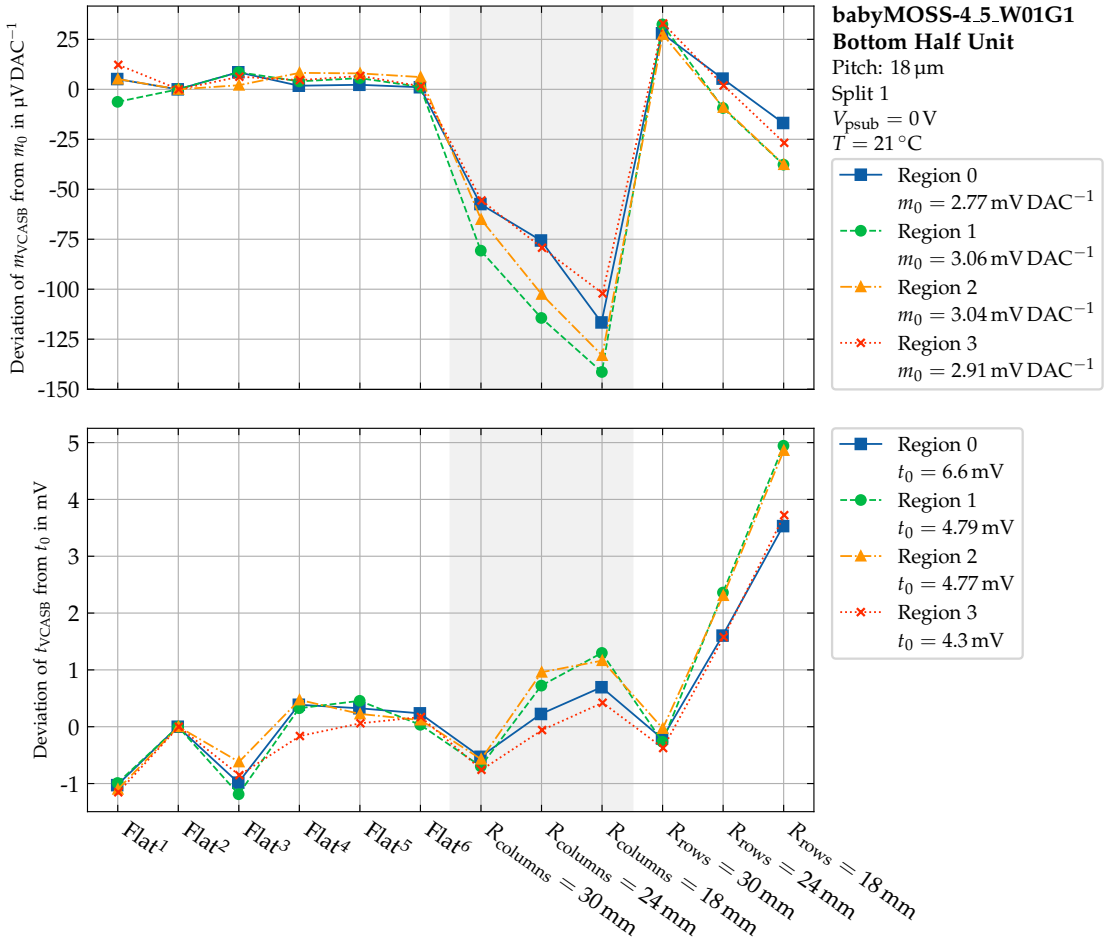

Figure 4.1: Changes of slope and offset for the V_{casb}-DAC plotted for the different bending configurations, babyMOSS-4_5_W01G1 with $V_{psub} = 0\,V$.

types. Therefore, no general statement can be made in this regard. Lastly, the operating point of the babyMOSSes was kept constant only in terms of the DAC settings. This means that the physical values of the frontend's biasing end were subject to change as the properties of the DACs shift, as presented here. The attempted partial corrections for this will also be discussed in the following two sections. Nevertheless, only the immediately involved DACs can be corrected, i.e., V_{casb} and – if applicable – V_{pulseh}. The influence of the shift in the other DACs cannot be compensated for in the analysis.

4.2 Threshold

Plotting the (mean) threshold against the applied V_{casb} values for each configuration yields many curves exhibiting the expected general trend, only slightly shifted relative to one another, cf., for example, Figure A.2.17. As these differences are relevant for this work, the absolute deviation of the threshold from that of the Flat[1] for each V_{casb} is considered, as depicted in Figure 4.2.

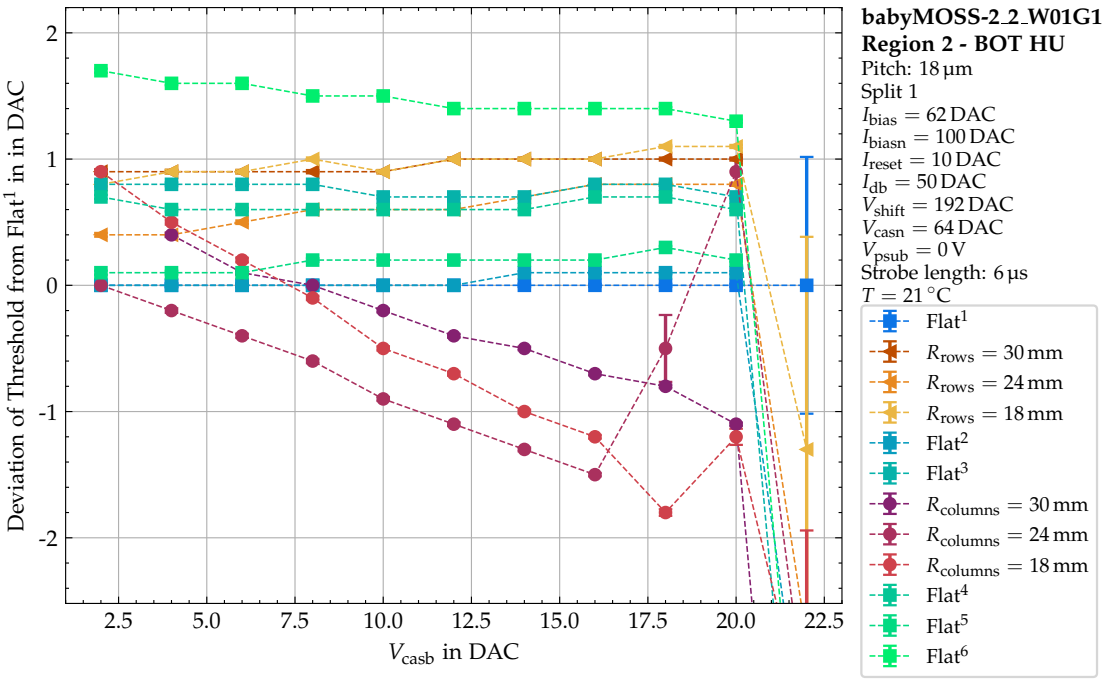

Figure 4.2: Deviation of threshold from Flat^1 plotted against V_{casb}, both given in DAC units, for region 2 of the BOT HU of babyMOSS-2_2_W01G1 with $V_{psub} = 0\,V$.

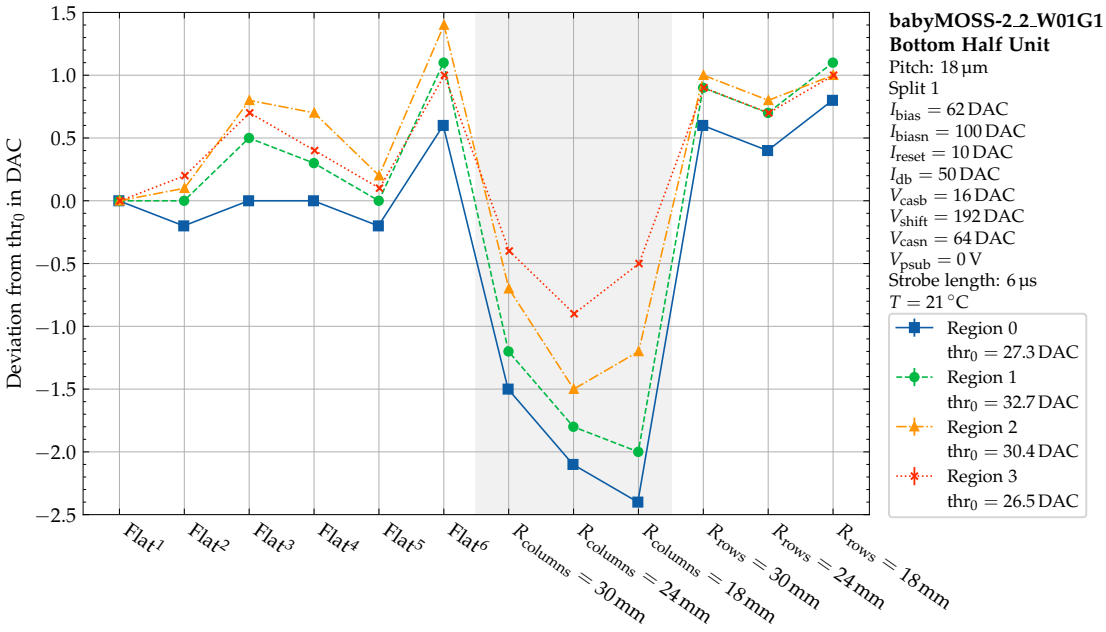

Figure 4.3: Deviation of threshold from thr$_0$ in DAC plotted against each configuration for $V_{casb} = 16\,DAC$ and the bottom HU of babyMOSS-2_2_W01G1 with $V_{psub} = 0\,V$.

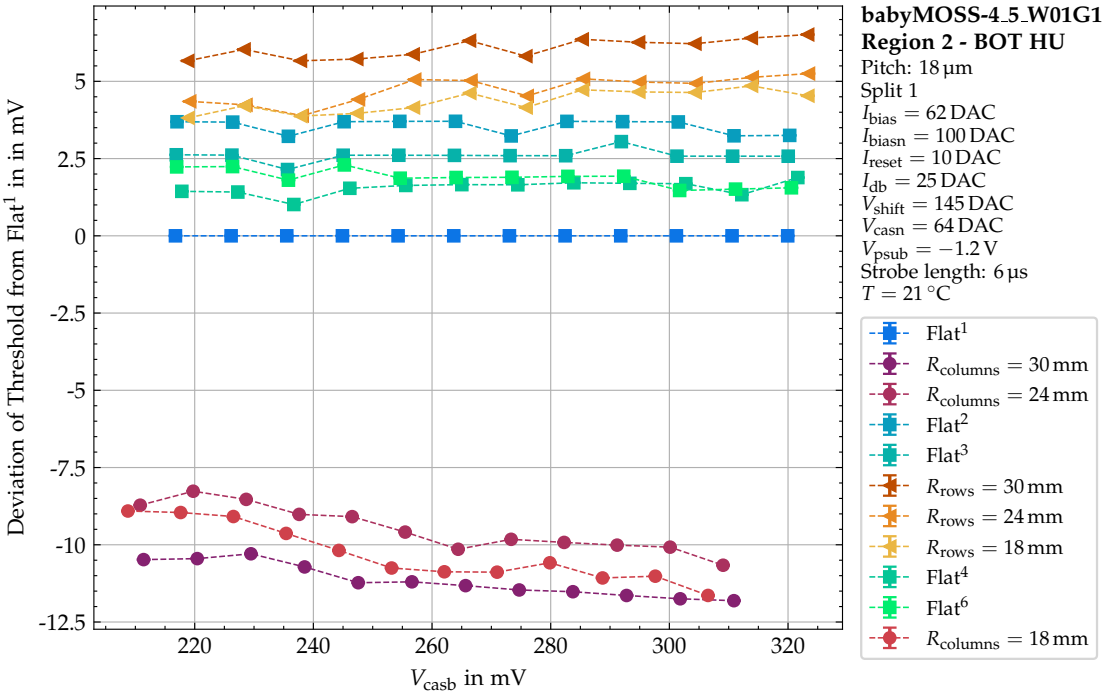

Figure 4.4: Deviation of threshold from Flat[1] plotted against V_{casb}, after both were converted into mV, for region 2 of the BOT HU of babyMOSS-4_5_W01G1 with $V_{psub} = -1.2\,V$.

Apart from some noisy outliers for the highest V_{casb} values, a clear trend is evident. The flat configurations form a relatively wide spread, for all of which the measured threshold is higher than the baseline measurement. Relative to this, bending along the column direction seems to decrease the threshold, although this effect diminishes and even slightly reverses for small V_{casb} values. If the DUT is bent along the rows, on the other hand, the threshold appears to increase slightly, yet there the Flat[6] configuration still lies higher. These statements are true for the general bending direction, but the hierarchy between the radii is not present, i.e., the middle radius is lower than the other two.

To illustrate this point further, a representative V_{casb} value can be selected, for which the deviation can be plotted against the configurations for all four regions of a HU at once, in this case resulting in Figure 4.3. Not only are the observations previously stated visible, but they also match those for the other regions in the same HU. Furthermore, these observations hold true for the threshold scans of all three babyMOSSes with $V_{psub} = 0\,V$.

With a backbias of $V_{psub} = -1.2\,V$ applied, the behavior of the scanned V_{casb} range is stabilized, cf. Figure A.2.29. The direction of the deviations is similar to that for the higher V_{casb} values with $V_{psub} = -1.2\,V$ discussed above. Their magnitude, however, is noticeably reduced.

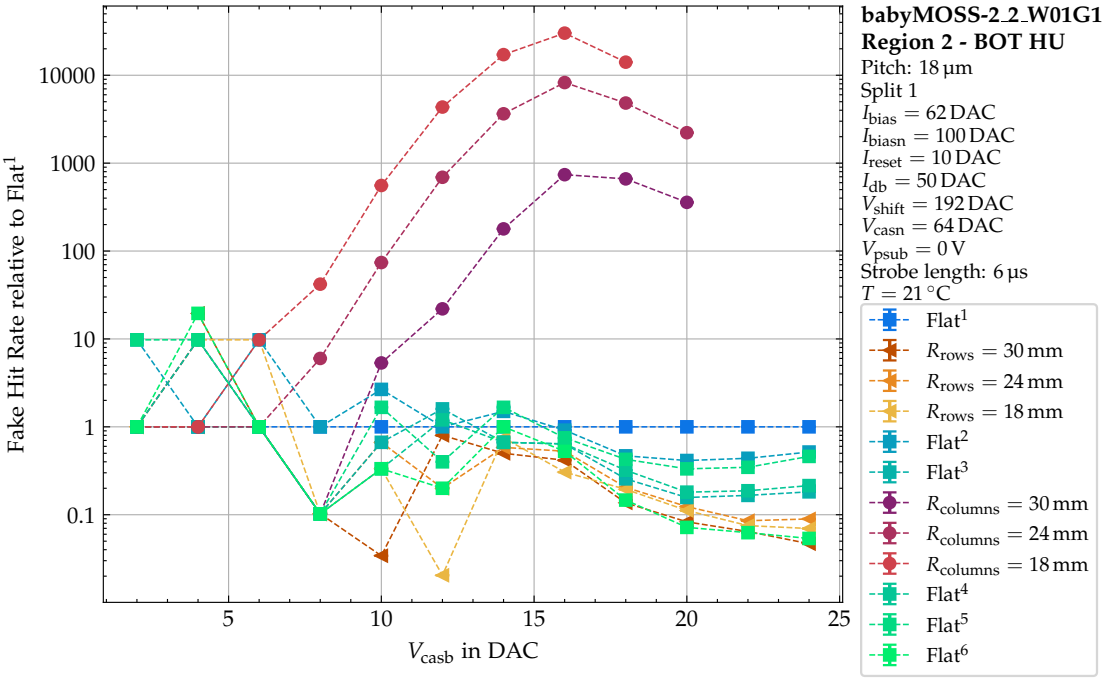

Figure 4.5: Fake hit rate relative to Flat[1] plotted against V_{casb} given in DAC units, for region 2 of the BOT HU of babyMOSS-2_2_W01G1 with $V_{psub} = 0\,V$.

Now, the threshold and V_{casb} values can each be converted into mV using the conversions obtained by the DAC scans[2]. It is essential to note that this conversion is performed directly for each bending configuration, using the values obtained from the scan, as shown, for example, in Figure A.2.20. This increases the separation of the different bending directions from the spread of the flat configurations across the board, with the effect being far more prominent at $V_{psub} = -1.2\,V$. To visualize this better, a plot of the deviations can be produced again, similar to Figure 4.2. This time, though, a linear interpolation of the measurements for the Flat[1] configuration is required, as the V_{casb} values now differ from one another, resulting in plots such as Figure 4.4. Comparing this plot to its counterpart with $V_{psub} = 0\,V$, the increased separation between bent and flat configurations with the application of backbias becomes obvious. This increase is partially expected with respect to the observations in Section 4.1. This is the case because the scanned V_{casb} range for $V_{psub} = -1.2\,V$ is higher than for $V_{psub} = 0\,V$ and thus the changes in the slope have a larger effect in the former case.

4.3 Fake Hit Rate

The plots for the fake hit rate follow the same paradigm as the ones in the previous section. Again, the raw plots show the expected general trend, but the variations are of interest. Due to the nature of the fake hit rate, the raw plots are semi-logarithmic, which is the reason why the relative deviations from Flat[1], not the absolute ones, are considered, as in Figure 4.5.

[2]For the conversion of the threshold values, the V_{pulseh} DAC is used, which is explained in Section 3.1.3

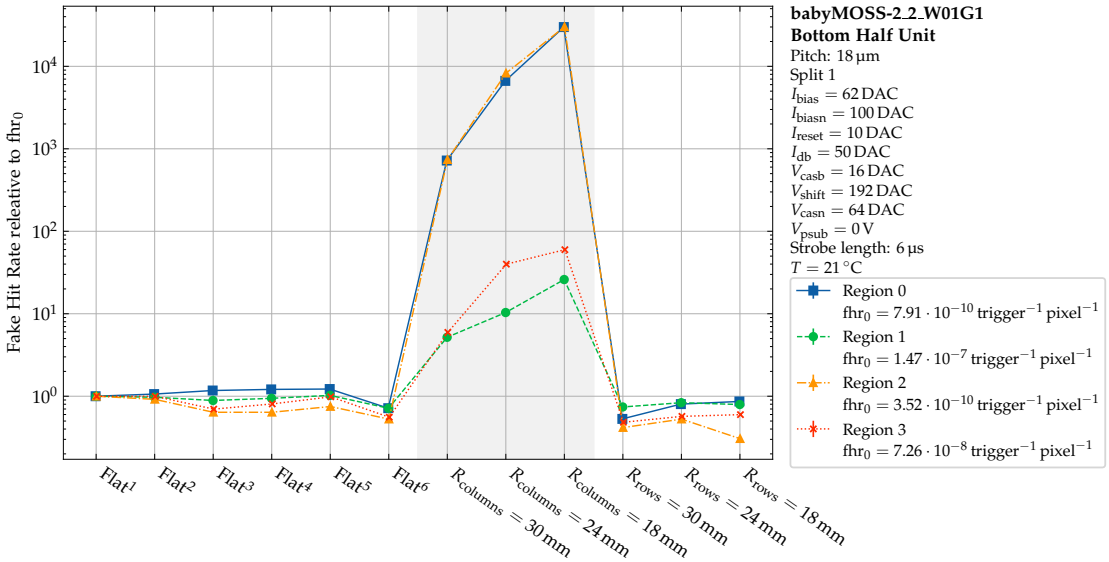

Figure 4.6: Fake hit rate relative to fhr_0 plotted against each configuration for $V_{casb} = 16\,DAC$ and the bottom HU of babyMOSS-2_2_W01G1 with $V_{psub} = 0\,V$.

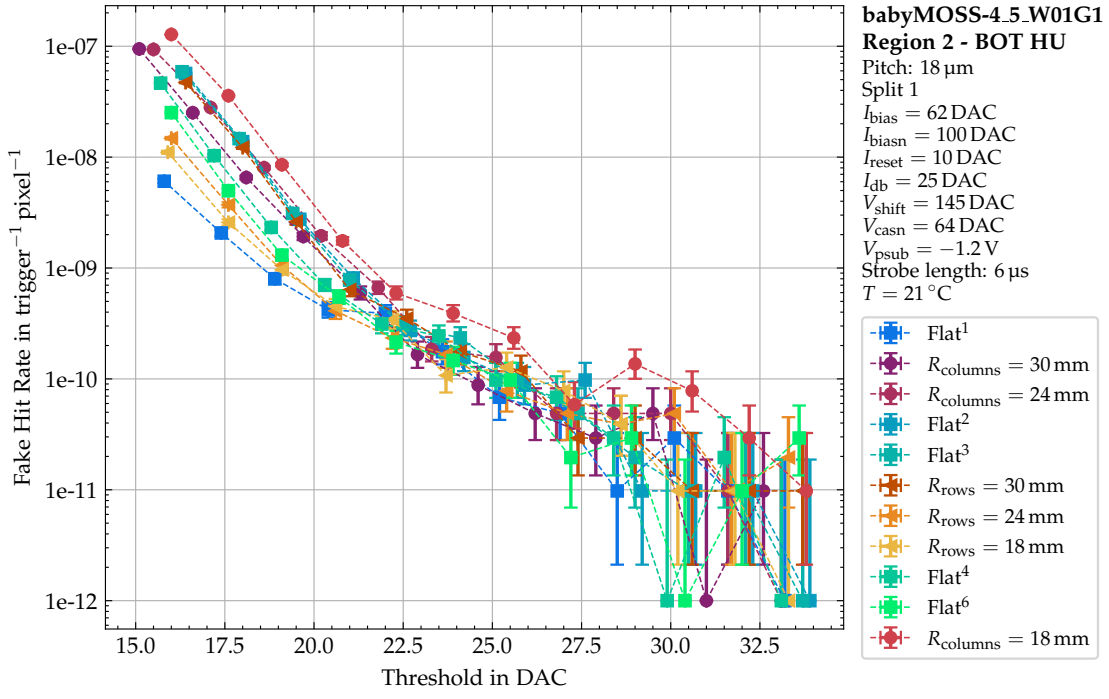

Figure 4.7: Fake hit rate plotted against the threshold in DAC, for region 2 of the BOT HU of babyMOSS-4_5_W01G1 with $V_{psub} = -1.2\,V$.

The systematic trends observed here generally go in the other direction, i.e., the fake hit rate increases for bending along the columns and decreases for bending along the rows. Nevertheless, the V_{casb} dependence remains similar, showing a decrease in the deviations for lower values. From Figure 4.6, which has been created in a similar manner to Figure 4.3, it can be seen that here the expected hierarchy for bending along the columns is observed, that is, a steady increase with a decrease in radius. For the other direction, no significant hierarchy can be observed, especially when comparing with the other setups, although the general shape remains consistent.

The effects of applying backbias, which include slight stabilization and reduction of deviations, are less pronounced in this case. One example of this is the comparison of Figure A.2.39 to Figure A.2.40, where for the fake hit rate, systematic deviations are still visible that cannot be seen for the threshold.

As the measurement of the fake hit rate is independent of any DAC, only the V_{casb} values can be converted into mV. Once more, the effect of this conversion is significantly smaller than for the threshold measurements; almost none can be discerned in the corresponding plots. An exception to this are the plots for a few regions that can be seen, for example, when comparing Figure A.1.17 to Figure A.1.18. There, the configurations that are bent along the columns move closer to the spread of the flat configurations for region 0 of the TOP HU and region 3 of the BOT HU.

Lastly, the fake hit rate can be plotted against the threshold obtained for each V_{casb} value. This delivers plots such as Figure 4.7. Generally, the separation of the data corresponding to different bending directions is not as prominent as in the other plots. In some cases, such as depicted in Figure 4.7, all configurations together form a spread, with the hierarchy being almost neutralized. As can be seen in Appendix A, other cases exist where the separation of bending along the column direction from all the others remains prominent. Although the cancellation seems to perform better with the application of backbias, no systematic correlations can be discerned.

4.4 Alignment

Before discussing the efficiency results, the quality of the alignment is to be assessed using the residual distributions of selected setups. A quick theoretical calculation gives a reference for comparison apart from the simulations introduced below. For this, a perfect binary pixel detector with pitch p being hit by a uniform particle beam is considered. This results in a constant hit position probability

$$\mathbb{P}_{\text{pixel}}(x_{\text{real hit}}) = \frac{1}{p} \begin{cases} 1, & \text{for } |x_{\text{real hit}}| < p/2 \\ 0, & \text{else} \end{cases},$$

where $x_{\text{real hit}}$ is the position of the hit relative to the pixel's center. The tracking of the particle's paths also underlies statistical processes, namely, multiple scattering. The resulting distribution of the differences between the reconstructed and actual hit positions $\delta = x_{\text{track}} - x_{\text{real hit}}$ is modeled by a Gaussian centered around zero,

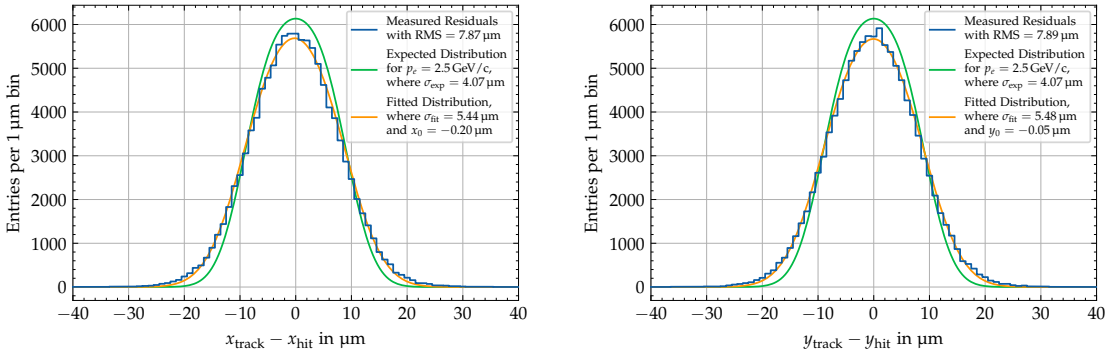

Figure 4.8: Residual distributions in x and y for Flat^2 at $V_{casb} = 15\,\mathrm{DAC}$ plotted with the expected and fitted distributions.

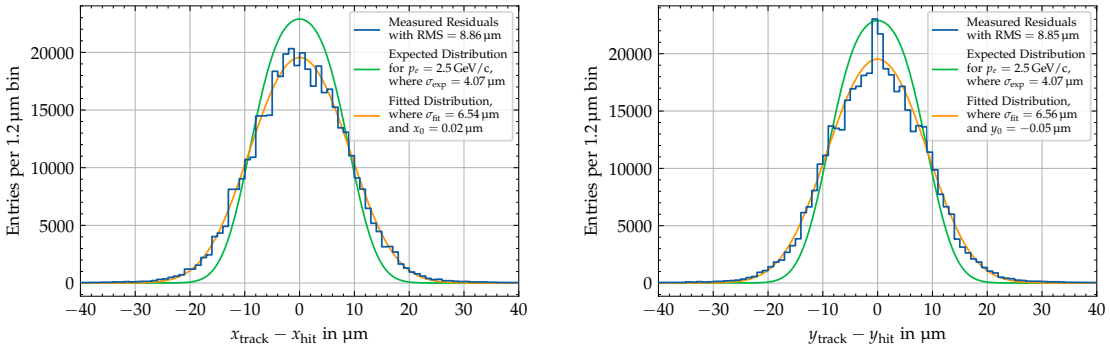

Figure 4.9: Residual distributions in x and y for a simulation of the telescope with a flat DUT, using [37], plotted with the expected and fitted distributions.

characterized by its standard deviation σ_{track}

$$\mathbb{P}_{track}(\delta) = \frac{1}{\sqrt{2\pi}\cdot\sigma_{track}} \cdot \exp\left(-\frac{\delta^2}{2\sigma_{track}^2}\right). \text{ [20, 21]}$$

Convoluting both of them results in a theoretical residual distribution of

$$\mathbb{P}_{res}(\Delta) = \frac{1}{2p}\left[\mathrm{erf}\left(\frac{p/2+\Delta}{\sqrt{2}\cdot\sigma_{track}}\right) + \mathrm{erf}\left(\frac{p/2-\Delta}{\sqrt{2}\cdot\sigma_{track}}\right)\right],$$

where erf is the gaussian error function and Δ the x or y residual. Using $\sigma_{track} = \sigma_{exp} = 4.07\,\mu m$ obtained from [38], this distribution is shown together with the measured residuals in Figures 4.8 to 4.11. Additionally, this distribution was fitted to the data with σ_{track} and an offset x_0 or y_0 as the free parameters. In both of these cases, the normalization was adjusted to correspond to the total number of entries as well as the binning of the histogram.

Firstly, a flat setup, specifically Flat^2, is considered in Figure 4.8. The distributions in x and y are very similar, being centered around zero and their RMS being within 20 nm of each other. Nevertheless, the expected distribution is narrower than the experimental data. This is especially obvious when comparing the fitted value of $\sigma_{track} = \sigma_{fit} \approx 5.4\,\mu m$ to the expected value, where a difference of around 1.4 µm can be observed.

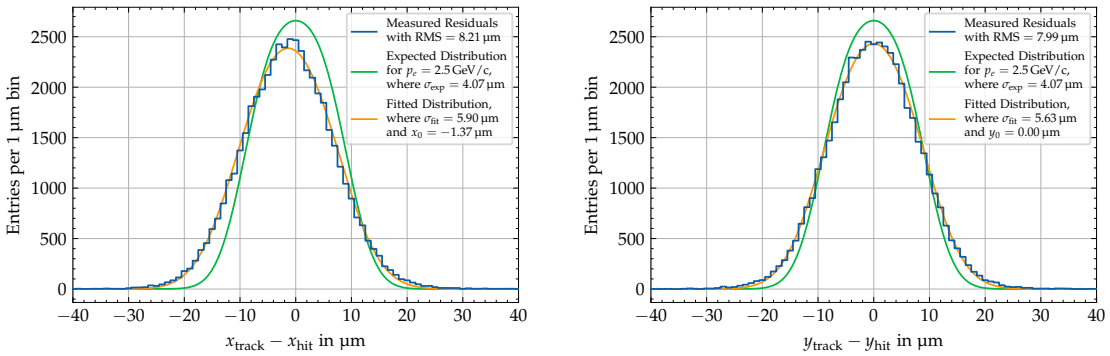

Figure 4.10: Residual distributions in x and y for $R_{\mathrm{columns}} = 18\,\mathrm{mm}$ at $V_{\mathrm{casb}} = 10\,\mathrm{DAC}$ plotted with the expected and fitted distributions.

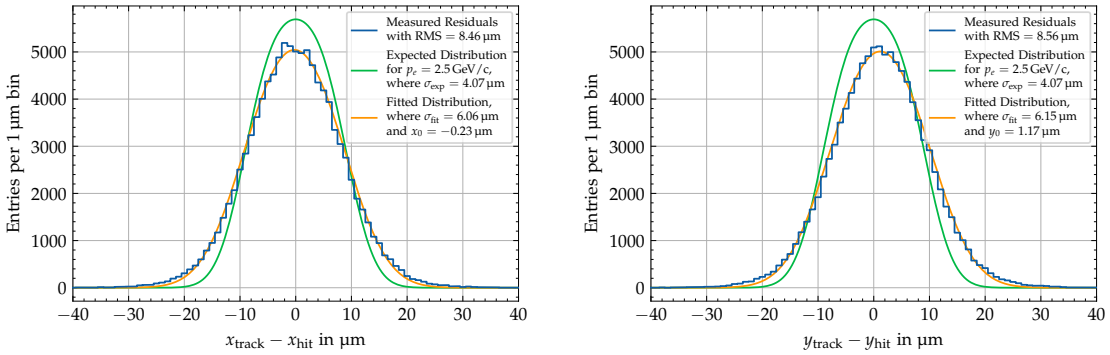

Figure 4.11: Residual distributions in x and y for $R_{\mathrm{rows}} = 18\,\mathrm{mm}$ at $V_{\mathrm{casb}} = 16\,\mathrm{DAC}$ plotted with the expected and fitted distributions.

As even multiple attempts failed to improve the analysis chain further, this discrepancy was investigated using a simulation of the telescope. This was executed using [37] with the appropriate geometry. The resulting distributions depicted in Figure 4.9 turned out to be even wider than the previously shown ones. This fact alone is not unexpected, as charge sharing and an in-pixel efficiency elevated near the center should improve the spatial resolution of the real experimental compared to a perfect binary pixel detector, as simulated [20, 21]. However, it shows that some other statistical process has likely been omitted in the previous theoretical consideration.

The distributions for both smallest radii are shown in Figures 4.10 and 4.11. The distributions *not* in the bending directions look fairly similar to the ones observed in Figure 4.8, albeit with a slightly higher width. Conversely, in the bending directions, the width increases further, but a significant offset of slightly over 1 µm can also be observed. Interestingly, these offsets are also in opposite directions. To illustrate this point further, the residual profiles of the aforementioned bending configurations can be plotted together. The relevant ones correlating the x-residuals with the columns and the y-residuals with the rows are depicted in Figures 4.13 and 4.14. Apart from the shift also observed in the residual distributions, a correlation of the residuals with the position both in the bending direction can be observed. Although the trend goes in the same direction in both cases, the height in the plot is substantially different. The latter

	Flat[1]	R_{columns} $= 30\,\text{mm}$	R_{columns} $= 18\,\text{mm}$	Flat[2]	R_{rows} $= 18\,\text{mm}$	Flat[4]	Sim. Flat
Reg. #	2	2	1	2	2	2	-
RMS_x	8.02 µm	8.02 µm	8.21 µm	7.87 µm	8.46 µm	7.97 µm	8.86 µm
RMS_y	7.97 µm	8.02 µm	7.99 µm	7.89 µm	8.56 µm	7.83 µm	8.85 µm
$\sigma_{\text{spatial, }x}$	6.91 µm	6.91 µm	7.13 µm	6.73 µm	7.41 µm	6.86 µm	7.87 µm
$\sigma_{\text{spatial, }y}$	6.86 µm	6.91 µm	6.88 µm	6.75 µm	7.53 µm	6.69 µm	7.86 µm

Table 4.12: RMSs of the residual distributions and the resulting approximate spatial resolutions in x and y for each setup, as well as a simulation of the telescope with flat DUT. The region that was used in the DUT alignment and analyzed here is also indicated. The approximate spatial resolution was calculated according to $\sigma_{\text{spatial}} = \sqrt{\text{RMS}^2 - \sigma_{\text{track}}^2}$, with $\sigma_{\text{track}} = 4.07\,\mu\text{m}$ [38].

observation corresponds to the different offset of the residual distributions. The other two setups, i.e., the one bent along the other direction and the flat reference, are mostly flat and centered around zero.

The reason for this seems to lie in a difference between the physical shape of the DUT and the one it is assumed to be in the coordinate transformations. The shape of the correlations suggests a simple deviation in the radius. However, this could not yet be confirmed through adjustments of the radius before running the alignment of the DUT, nor estimated from the presented plots.

Comparing the RMSs of the residual distributions of all the setups, as shown in Table 4.12, shows that the rest of the setups lie between what has been shown above. Since this work is not concerned with deriving the detector's spatial resolution from these distributions, the alignment obtained here was deemed adequate for the efficiency analysis.

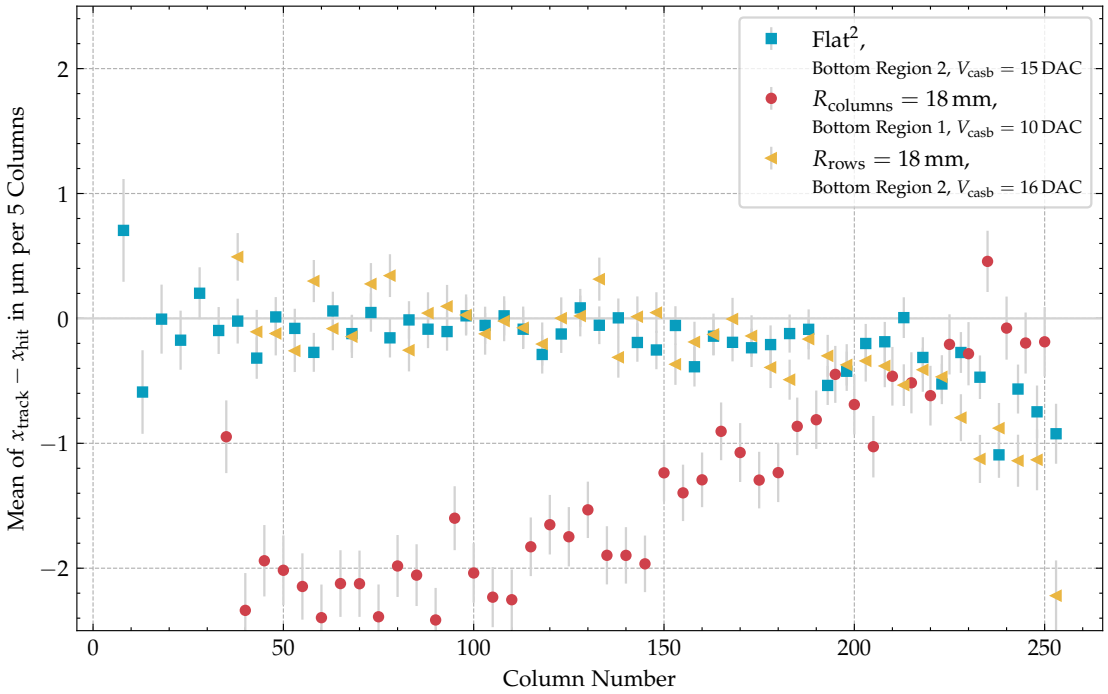

Figure 4.13: Residual profiles in x plotted against the column number for three different bending configurations. The analyzed region and the used V_{casb} value are also indicated for each.

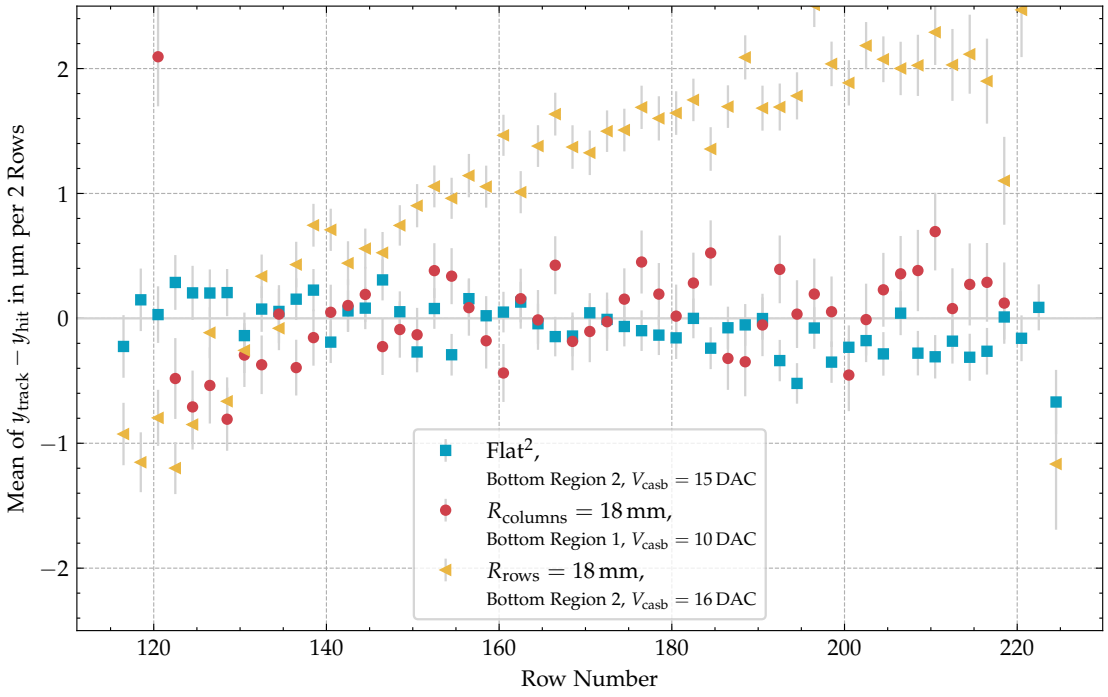

Figure 4.14: Residual profiles in y plotted against the row number for three different bending configurations. The analyzed region and the used V_{casb} value are also indicated for each.

4.5 Efficiency

Finally, after the alignment has been validated, the efficiency results can be discussed. Plotting the measured efficiency against the V_{casb} value for which it was obtained yields plots such as Figure 4.15. As an example, region 1 of the BOT HU with $V_{\text{psub}} = 0\,\text{V}$ is shown; the results from other measurements can be found in Appendix B. Especially in the plot shown here, the same hierarchy as discussed in the previous chapter can be observed. All the flat configurations lie close together, forming a band, the spread of which is considered the systematic uncertainty from the repeatability of the measurement. The efficiency increases with bending in the column direction, whereas it decreases with bending in the row direction. The same general trend is also seen for region 2 of the BOT HU, cf. Figure B.0.3. However, there is no significant distinction between $R_{\text{columns}} = 30\,\text{mm}$ and $R_{\text{columns}} = 18\,\text{mm}$. Also, the separation of $R_{\text{rows}} = 18\,\text{mm}$ from the spread of the flat configurations is reduced.

With the application of backbias, the deviations get smaller, even diminishing for the highest V_{casb} values scanned. As depicted in Figure B.0.4, for region 2 of the BOT HU, the $R_{\text{rows}} = 18\,\text{mm}$ configuration even partially lies within the spread of the flat configurations.

Using a smooth interpolation of the threshold scans executed during the testbeam, the efficiency can be plotted against the corresponding threshold value. As can be seen from Figure 4.16, this reduces the deviations for the different setups, in this case, even significantly. For the other chips and backbias settings, this reduction is not as pronounced, although it is still clearly visible.

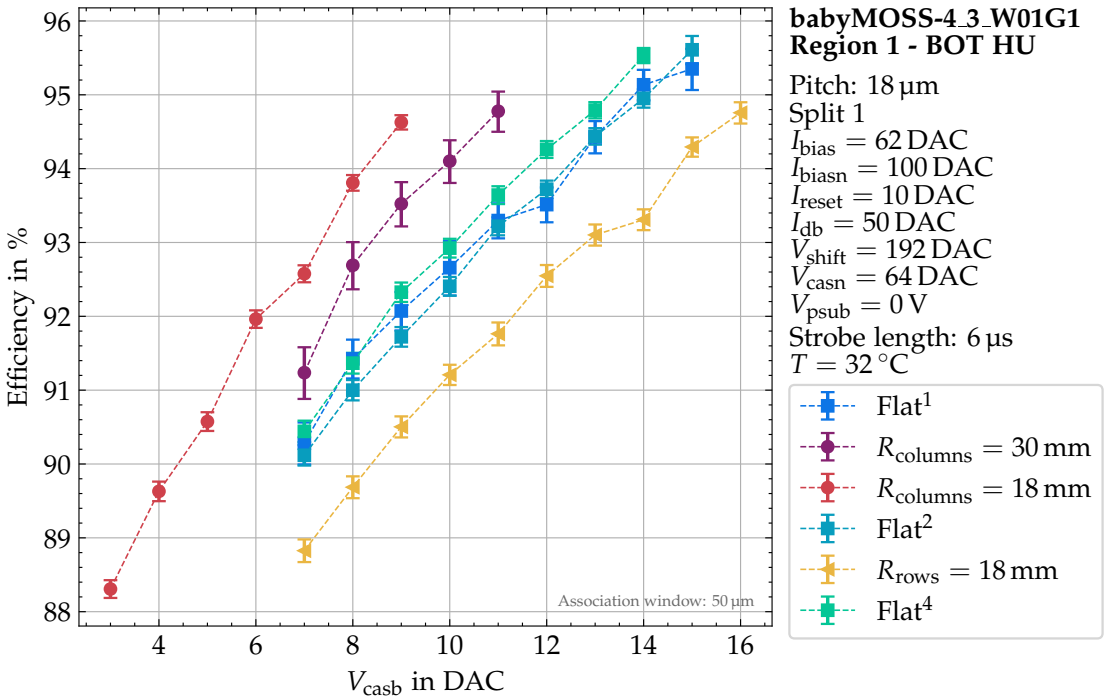

Figure 4.15: Efficiency plotted against V_{casb} in DAC, for region 1 of the BOT HU of babyMOSS-4_3_W01G1 with $V_{\text{psub}} = 0\,\text{V}$.

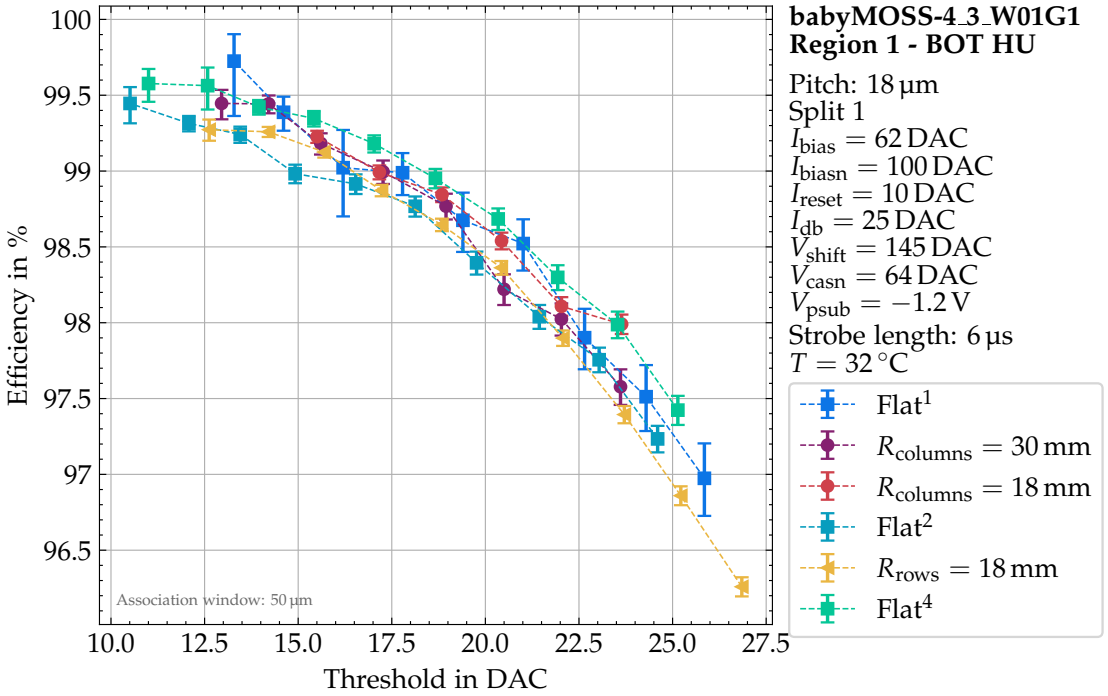

Figure 4.16: Efficiency plotted against threshold in DAC units, for region 1 of the BOT HU of babyMOSS-4_3_W01G1 with $V_{psub} = -1.2$ V.

As explained before, no complete set of DAC scans is available, which is the reason why the V_{casb} values cannot be converted into mV.

The profiles of the efficiency against the rows and columns are ultimately considered. These were investigated as a previous testbeam showed an increase in the efficiency with shallower incidence angles. Of specific interest are only the profiles for the smallest bent radii in the directions of bending. These are depicted for a representative V_{casb} value in Figures 4.17 and 4.18. The other axis, as well as the same plots for the Flat^2 configuration, can also be found in Appendix B. In all of these, no correlations between the efficiency and row or column numbers can be observed. On the one hand, this was expected. Both analyzed regions are located in the middle. In addition, the ROIs additionally limit the distance from the middle. This means that the incoming particles hit the sensors at nearly vertical incidence angle over the whole ROI. Subsequently, no geometric effects from bending on the efficiency are expected. On the other hand, this indicates that no other position-dependent effects on the efficiency are present —- at least for the bottom regions 1 and 2.

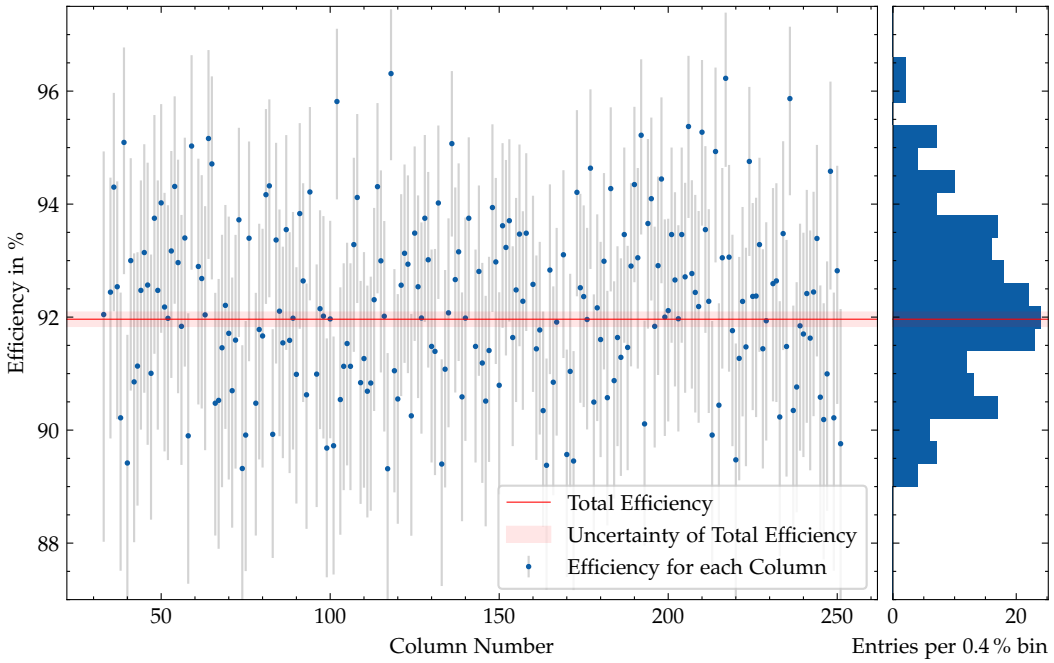

Figure 4.17: Efficiency of the column plotted against the corresponding column number for $R_{\text{columns}} = 18\,\text{mm}$, $V_{\text{casb}} = 10\,\text{DAC}$, region 1 of the BOT HU of babyMOSS-4_3_W01G1 with $V_{\text{psub}} = 0\,\text{V}$. The efficiency distribution and the mean of the whole region are also indicated.

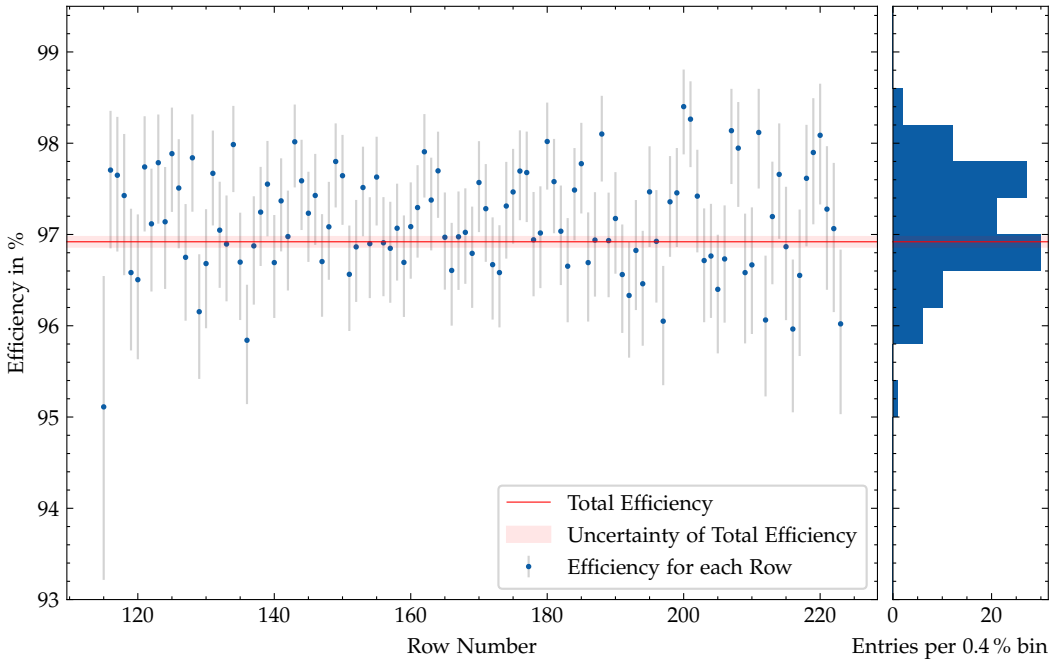

Figure 4.18: Efficiency of the row plotted against the corresponding row number for $R_{\text{rows}} = 18\,\text{mm}$, $V_{\text{casb}} = 16\,\text{DAC}$, region 2 of the BOT HU of babyMOSS-4_3_W01G1 with $V_{\text{psub}} = 0\,\text{V}$. The efficiency distribution and the mean of the whole region are also indicated.

5 Conclusion and Outlook

This work established the concept of testing the influence of bending on the performance of MAPS. Small-scale prototypes – the babyMOSSes – were mounted onto FPCs. These then could be bent into different radii and directions by mounting them on suitable jigs, without causing permanent functional damage to the chips themselves. At the same time, the available software was modified to accommodate the bent DUT for the testbeam. This yielded sufficiently good alignment to carry out an efficiency analysis. Nevertheless, more fundamental changes to the coordinate transformation and alignment algorithm are necessary to eliminate the remaining misalignment caused by deviations in the chip's shape from a perfect cylinder with the expected radius.

Changes in the chips' performance were observed in every investigated metric with bending. The effects were more prominent for bending along the columns than for bending along the rows. While their exact magnitude depended on the applied backbias and – if applicable – V_{casb} values, these changes partially recovered when unbending the chip but did not consistently reach their initial baseline values.

Firstly, all the DACs used for biasing the analog frontend exhibited changes in their behavior. This was systematically observed in the slope of the calibration curves, whereas the behavior of the offset was not consistent.

Secondly, the threshold, fake hit rate, and efficiency measurements were also subject to change under bending. The threshold decreased for bending along the columns, and increased for bending along the rows. These deviations occur in opposite directions for both the fake hit rate and efficiency measurements. However, when plotting both against the corresponding threshold values, the deviances did not cancel out.

Additionally, the effects of the changes in the performance of the DACs were attempted to be compensated. For this the immediately involves voltages, V_{casb} and V_{pulseh} for the threshold scans, were converted into mV. This actually increased the separation between the different bending directions. Nevertheless, this does not rule out the influence of all the other biases of the frontend; therefore, these results need to be viewed with critical judgment.

Lastly, unbending the chips seems to restore the original operating point almost completely. This suggests that the observed effects are reversible, and no permanent damage from bending is expected.

Altogether, it is shown that the operating point shifts in terms of the DAC units. Still, there seems to be ample headroom to compensate for this in operation.

Despite that, it would be of interest to eliminate the influence of changes in the performance of the DACs and investigate whether the same effects on the threshold, fake hit rate, and efficiency could be observed. For this, a new measurement campaign

should be conducted, where the operating point should be held constant in terms of the physical quantities, rather than the DAC units as done in this work.

Furthermore, it is suspected that the changes observed also depend on the orientation of the physical layout of the analog frontend, as supported by [30]. Therefore, the tests presented here and those suggested above should be repeated for the next generation of prototypes, as their layout will be closer to that of chips, which will be installed in ITS3.

Acknowledgments

First of all, I would like to thank my supervisor, Berkin Ulukutlu, for the amazing support he provided throughout my thesis and his never-ending patience. Then, I would like to thank Prof. Dr. Laura Fabbietti for giving me this opportunity and welcoming me into her group, which offered me a comfortable and productive environment. I found that all members were always willing to offer advice or help out when needed. I would like to specifically mention Dr. Roman Gernhäuser, who, on more than one occasion, provided essential ideas that moved the project forward.

Lastly, but perhaps most importantly, I would like to thank my friends who accompanied me throughout the entire journey; in particular, Julian Saure, Alpin Gencer, and Anna Fleindl, all of whom took the time to read my thesis and provide me with additional insightful feedback.

Bibliography

[1] "LHC Machine". In: *JINST* 3 (2008). Ed. by L. Evans and P. Bryant, S08001. DOI: 10.1088/1748-0221/3/08/S08001.

[2] *Facts and figures about the LHC | CERN*. URL: https://home.cern/resources/faqs/facts-and-figures-about-lhc (visited on 10/02/2025).

[3] E. Lopienska. *The CERN accelerator complex, layout in 2022 - CERN Document Server*. 2022. URL: https://cds.cern.ch/record/2800984/files/?ln=de (visited on 10/03/2025).

[4] *Light ions at the LHC: first results from oxygen–oxygen and neon–neon collisions*. Oct. 2025. URL: https://ep-news.web.cern.ch/content/light-ions-lhc-first-results-oxygen-oxygen-and-neon-neon-collisions (visited on 10/13/2025).

[5] *LHC report: xenon in action*. Oct. 2017. URL: https://home.cern/news/news/accelerators/lhc-report-xenon-action (visited on 10/13/2025).

[6] *First ever oxygen and neon LHC collisions are studied by CMS | CMS Experiment*. July 2025. URL: https://cms.cern/news/first-ever-oxygen-and-neon-lhc-collisions-are-studied-cms (visited on 10/13/2025).

[7] O. Brüning et al. "70 years at the high-energy frontier with the CERN accelerator complex". In: *Nat. Rev. Phys.* 6.10 (Oct. 2024). Publisher: Nature Publishing Group, pp. 628–637. DOI: 10.1038/s42254-024-00758-5.

[8] *ALICE*. Sept. 2025. URL: https://home.cern/science/experiments/alice (visited on 10/02/2025).

[9] *ATLAS*. Sept. 2025. URL: https://home.web.cern.ch/science/experiments/atlas (visited on 10/02/2025).

[10] *CMS*. Sept. 2025. URL: https://home.cern/science/experiments/cms (visited on 10/02/2025).

[11] *Lhcb*. Sept. 2025. URL: https://home.web.cern.ch/science/experiments/lhcb (visited on 10/02/2025).

[12] *CERN experiments observe particle consistent with long-sought Higgs boson*. July 2012. URL: https://home.web.cern.ch/news/press-release/cern/cern-experiments-observe-particle-consistent-long-sought-higgs-boson (visited on 10/02/2025).

[13] G. Apollinari et al. *High Luminosity Large Hadron Collider HL-LHC*. 2015. DOI: 10.5170/CERN-2015-005.1.

[14] *Updated schedule for CERN's accelerators*. Oct. 2024. URL: https://home.cern/news/opinion/accelerators/updated-schedule-cerns-accelerators (visited on 10/02/2025).

[15] *BMFTR-Forschungsschwerpunkt ALICE*. URL: https://lhc-deutschland.de/lhc_deutschland/fsp_alice/index_ger.html (visited on 10/02/2025).

[16] "ALICE upgrades during the LHC Long Shutdown 2". In: *JINST* 19.05 (May 2024), P05062. DOI: 10.1088/1748-0221/19/05/P05062.

[17] K. Aamodt et al. "The ALICE experiment at the CERN LHC". In: *JINST* 3 (2008), S08002. DOI: 10.1088/1748-0221/3/08/S08002.

[18] B. Abelev et al. "Technical Design Report for the Upgrade of the ALICE Inner Tracking System". In: *J. Phys. G* 41 (2014), p. 087002. DOI: 10.1088/0954-3899/41/8/087002.

[19] *Technical Design report for the ALICE Inner Tracking System 3 - ITS3 ; A bent wafer-scale monolithic pixel detector - CERN Document Server*. URL: https://cds.cern.ch/record/2890181/files/?docname=ALICE-TDR-021&version=all (visited on 10/02/2025).

[20] L. Rossi et al. *Pixel Detectors: From Fundamentals To Applications*. Particle acceleration and detection. Springer, 2006. ISBN: 978-3-540-28333-1.

[21] H. Kolanoski and N. Wermes. *Teilchendetektoren*. Springer, 2016. DOI: 10.1007/978-3-662-45350-6.

[22] W. Snoeys. "Monolithic CMOS Sensors for high energy physics — Challenges and perspectives". In: *Nucl. Instrum. Methods Phys. Res., Sect. A* 1056 (Nov. 2023), p. 168678. DOI: 10.1016/j.nima.2023.168678.

[23] W. Snoeys et al. "A process modification for CMOS monolithic active pixel sensors for enhanced depletion, timing performance and radiation tolerance". In: *Nucl. Instrum. Methods Phys. Res., Sect. A* 871 (Nov. 2017), pp. 90–96. DOI: 10.1016/j.nima.2017.07.046.

[24] L. Musa. *Letter of Intent for an ALICE ITS Upgrade in LS3*. 2019. DOI: 10.17181/CERN-LHCC-2019-018.

[25] *Upgrade of the ALICE Inner Tracking System during LS3: study of physics performance*. 2023. URL: https://cds.cern.ch/record/2868015/files/.

[26] O. Abdelrahman et al. *Characterisation of the first wafer-scale prototype for the ALICE ITS3 upgrade: the monolithic stitched sensor (MOSS)*. Oct. 2025. DOI: 10.48550/arXiv.2510.11463.

[27] P. Double and R. Turchetta. *Wafer-scale CMOS X-ray imaging for medical apps*. Aug. 2012. URL: https://eetimes.com/wafer-scale-cmos-x-ray-imaging-for-medical-apps/ (visited on 10/20/2025).

[28] F. Piro et al. "A Compact Front-End Circuit for a Monolithic Sensor in a 65-nm CMOS Imaging Technology". In: *IEEE Trans. Nucl. Sci.* 70.9 (Sept. 2023), pp. 2191–2200. DOI: 10.1109/TNS.2023.3299333.

[29] *MOSS User Manual · Wiki · MOSS Testing · GitLab*. Jan. 2024. URL: https://gitlab.cern.ch/groups/alice-its3-wp3/moss-testing/-/wikis/Moss%20user%20manual (visited on 10/20/2025).

[30] M. J. Rossewij et al. *Electrical/piezoresistive effects in bent Alpide MAPS*. Mar. 2024. DOI: 10.48550/arXiv.2403.12298.

[31] Y. Liu et al. "EUDAQ2—A flexible data acquisition software framework for common test beams". In: *JINST* 14.10 (Oct. 2019), P10033. DOI: 10.1088/1748-0221/14/10/P10033.

[32] *ALICE ITS3 WP3 / MOSS Testing / SW · GitLab*. Apr. 2025. URL: https://gitlab.cern.ch/alice-its3-wp3/moss-testing/sw (visited on 10/25/2025).

[33] G. A. Rinella et al. "Digital Pixel Test Structures implemented in a 65 nm CMOS process". In: *Nucl. Instrum. Methods Phys. Res., Sect. A* 1056 (Nov. 2023), p. 168589. DOI: 10.1016/j.nima.2023.168589. (Visited on 10/02/2025).

[34] D. Dannheim et al. "Corryvreckan: a modular 4D track reconstruction and analysis software for test beam data". In: *JINST* 16.03 (Mar. 2021). Publisher: IOP Publishing, P03008. DOI: 10.1088/1748-0221/16/03/P03008.

[35] P. Mann. *Philipp Mann / EUDAQ2 · GitLab*. July 2025. URL: https://gitlab.cern.ch/pmann/eudaq (visited on 10/25/2025).

[36] P. Mann. *Philipp Mann / Corryvreckan ITS3 · GitLab*. 2025. URL: https://gitlab.cern.ch/pmann/corryvreckan (visited on 10/25/2025).

[37] B. Ulukutlu. *bulukutlu/telescopeSimulator*. Sept. 2025. URL: https://github.com/bulukutlu/telescopeSimulator (visited on 10/28/2025).

[38] M. Mager. *The Telescope Optimiser*. 2016. URL: https://mmager.web.cern.ch/telescope/tracking.html#part=e&p=2.5&x=%5B-5,0,5,7.5,14.95,20,22.5,27.5,32.5%5D&XX0=%5B,0.0005,0.0005,0.0005,0.0005,0.0005,0.0005,0.0005,%5D&sy=%5B,0.00052,0.00052,0.00052,0.00052,0.00052,0.00052,0.00052,%5D&en=%5B0,1,1,1,0,1,1,1,0%5D&ymc=%5BNaN,0,0,0,0,0,0,0,0%5D&ym=%5BNaN,0,0,0,0,0,0,0,0%5D&scaley=0.0005 (visited on 10/28/2025).

List of Figures

List of Tables

A Offline Scans

A.1 babyMOSS-2_2_W01G1

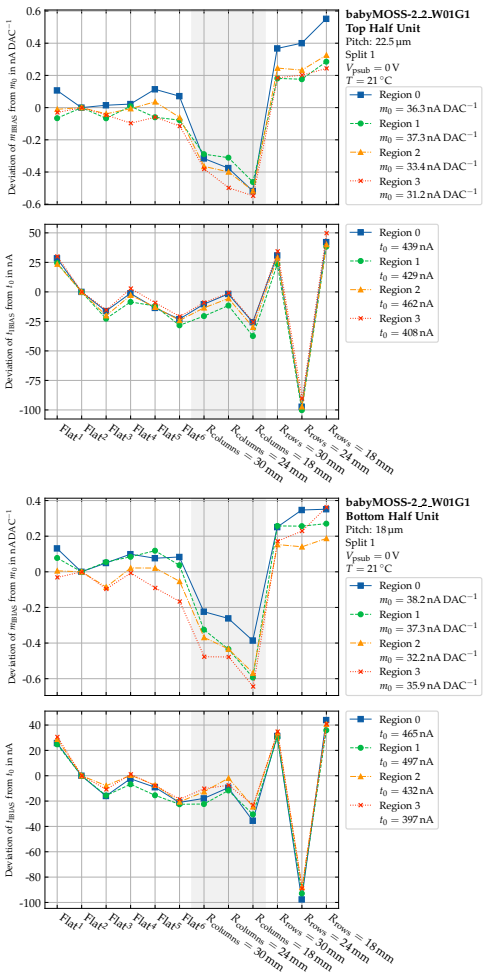

Figure A.1.1: Changes of slope and offset for the I_{bias}-DAC vs. configuration, for babyMOSS-2_2_W01G1 with $V_{\text{psub}} = 0\,\text{V}$.

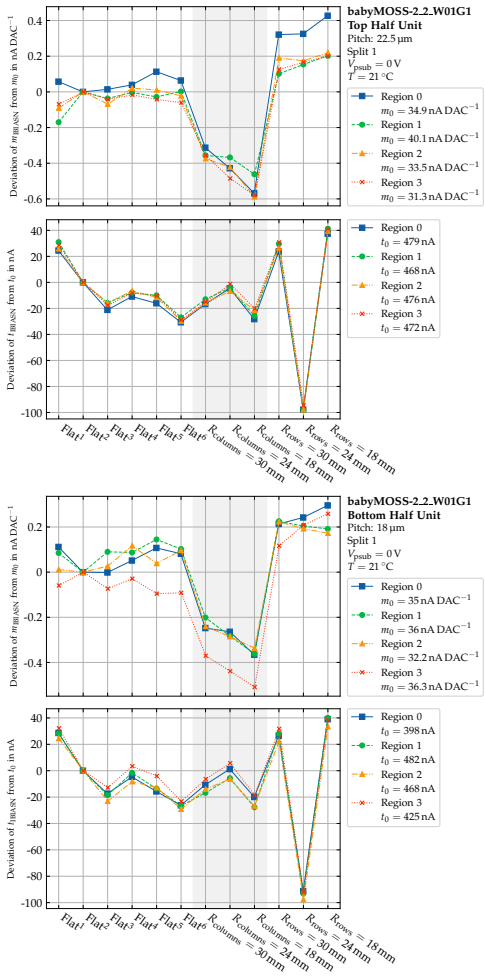

Figure A.1.2: Changes of slope and offset for the I_{biasn}-DAC vs. configuration, for babyMOSS-2_2_W01G1 with $V_{\text{psub}} = 0\,\text{V}$.

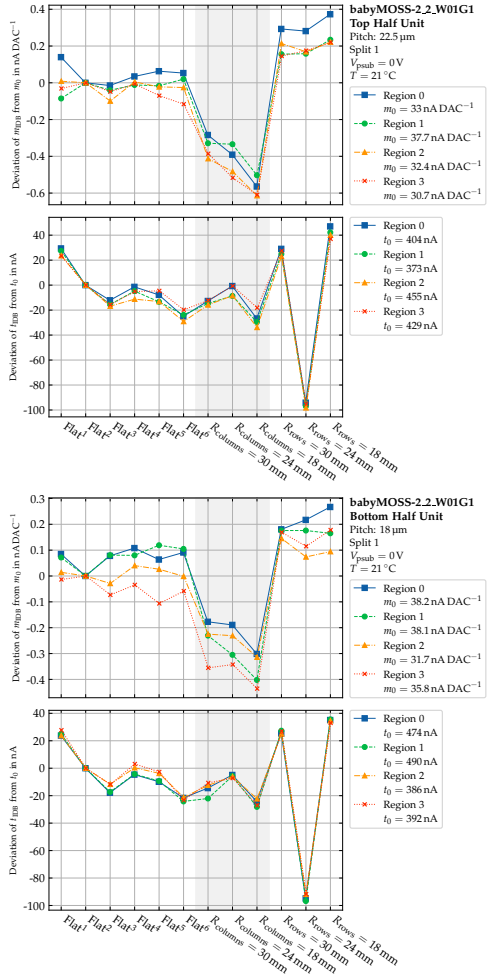

Figure A.1.3: Changes of slope and offset for the I_{db}-DAC vs. configuration, for babyMOSS-2_2_W01G1 with $V_{\text{psub}} = 0\,\text{V}$.

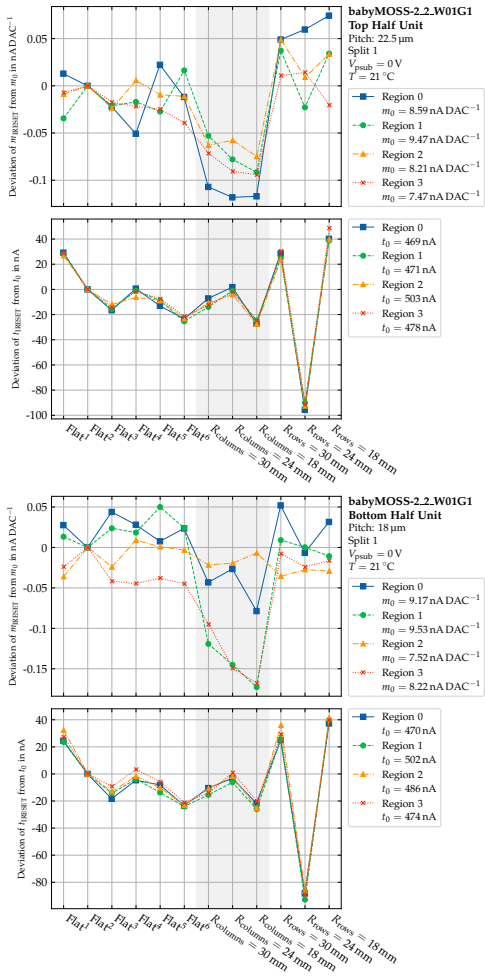

Figure A.1.4: Changes of slope and offset for the I_{reset}-DAC vs. configuration, for babyMOSS-2_2_W01G1 with $V_{\text{psub}} = 0\,\text{V}$.

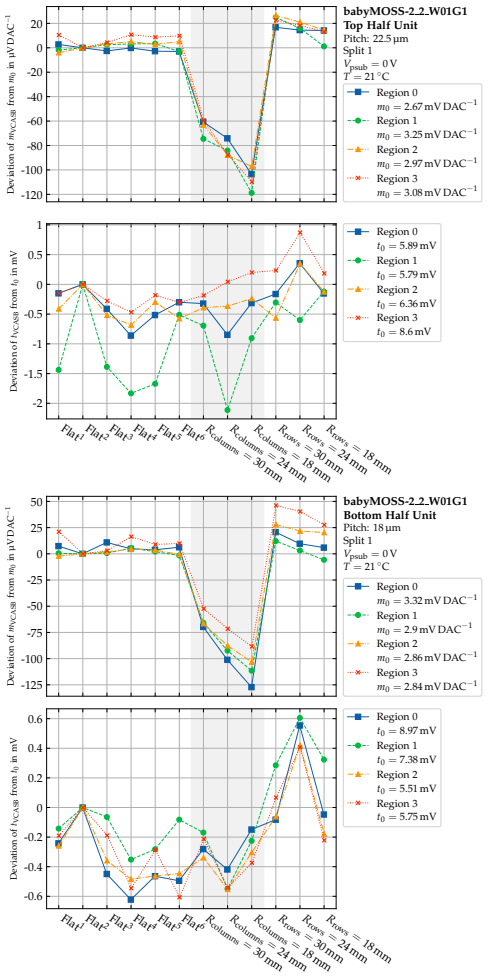

Figure A.1.5: Changes of slope and offset for the V_{casb}-DAC vs. configuration, for babyMOSS-2_2_W01G1 with $V_{\text{psub}} = 0\,\text{V}$.

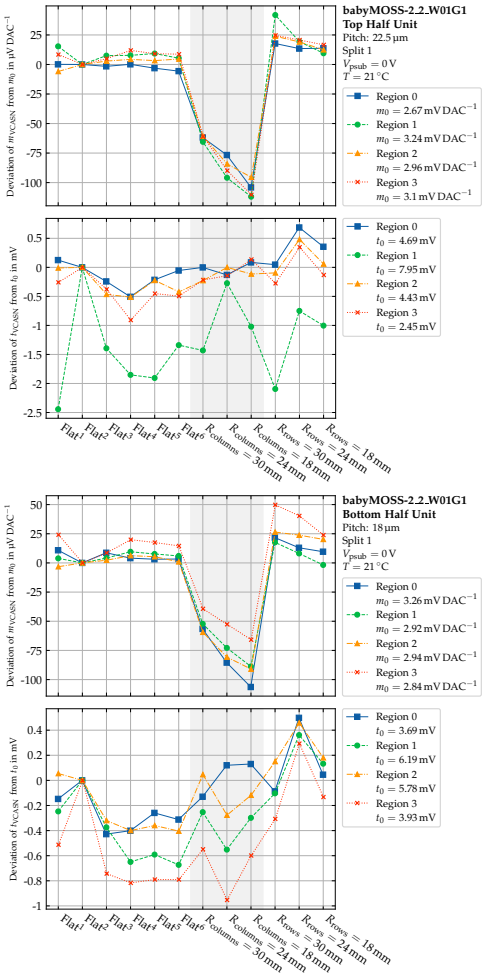

Figure A.1.6: Changes of slope and offset for the V_{casn}-DAC vs. configuration, for babyMOSS-2_2_W01G1 with $V_{\text{psub}} = 0\,\text{V}$.

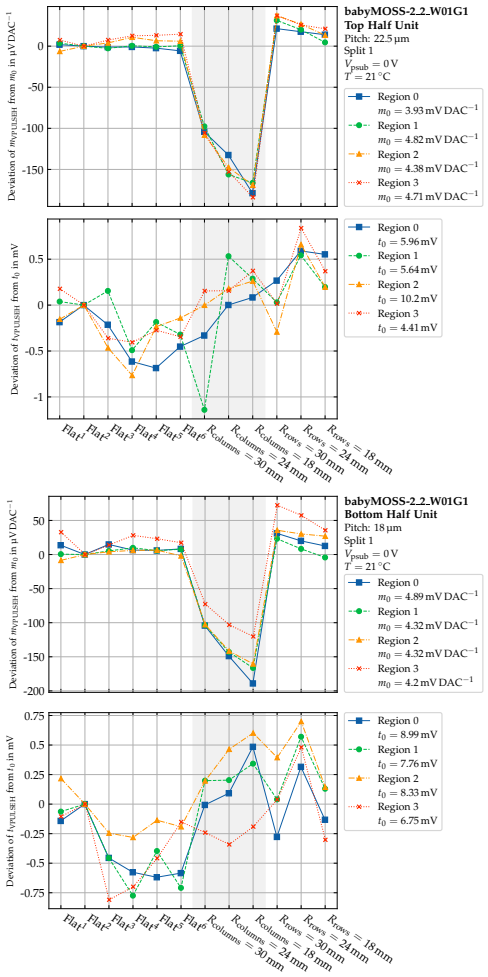

Figure A.1.7: Changes of slope and offset for the V_{pulseh}-DAC vs. configuration, for babyMOSS-2_2_W01G1 with $V_{\text{psub}} = 0\,\text{V}$.

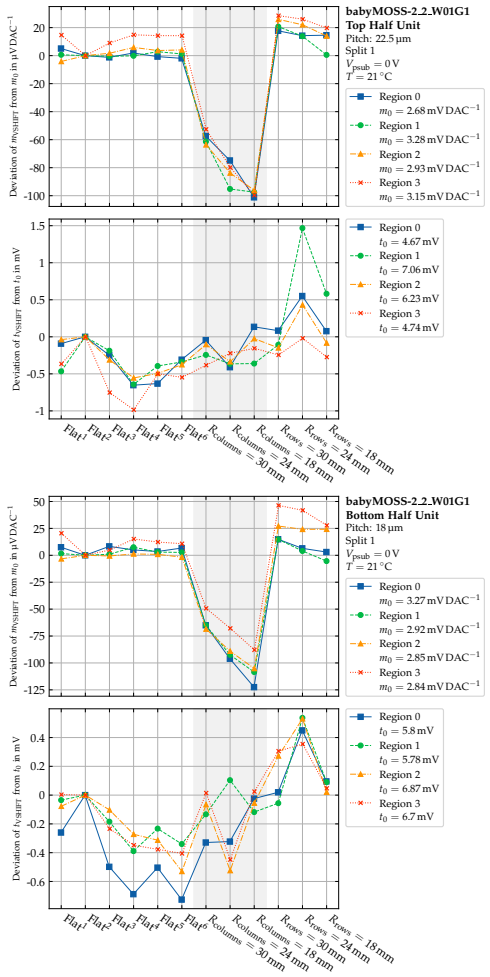

Figure A.1.8: Changes of slope and offset for the V_{shift}-DAC vs. configuration, for babyMOSS-2_2_W01G1 with $V_{\text{psub}} = 0\,\text{V}$.

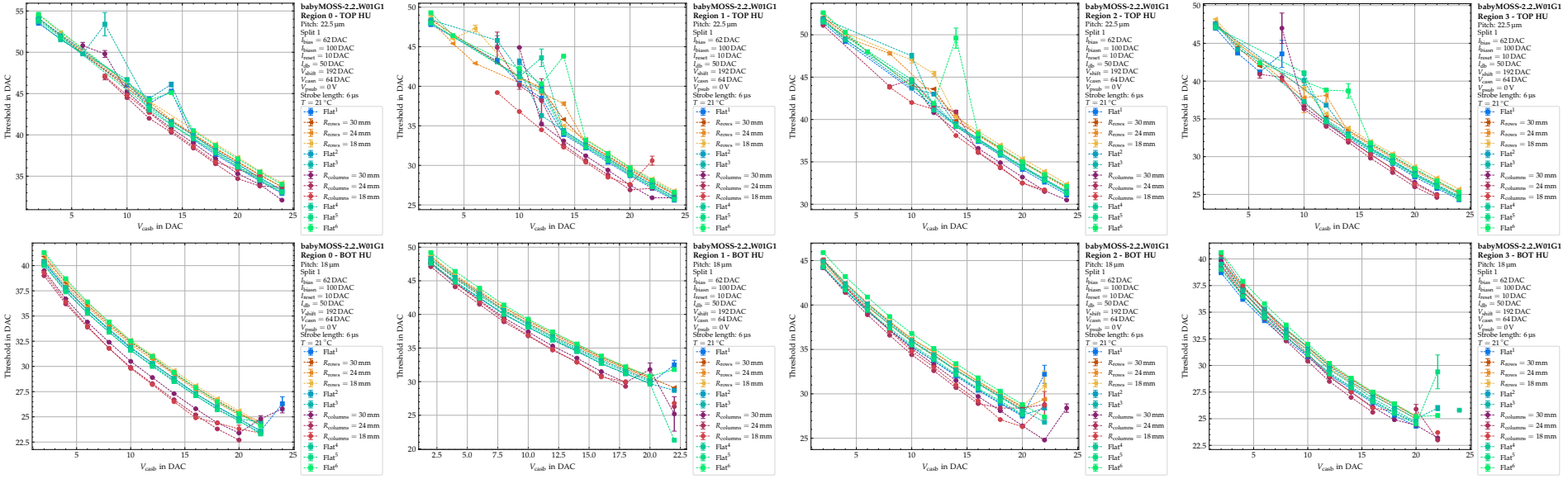

Figure A.1.9: Threshold in DAC vs. V_{casb} in DAC, for babyMOSS-2_2_W01G1 with $V_{\text{psub}} = 0\,\text{V}$.

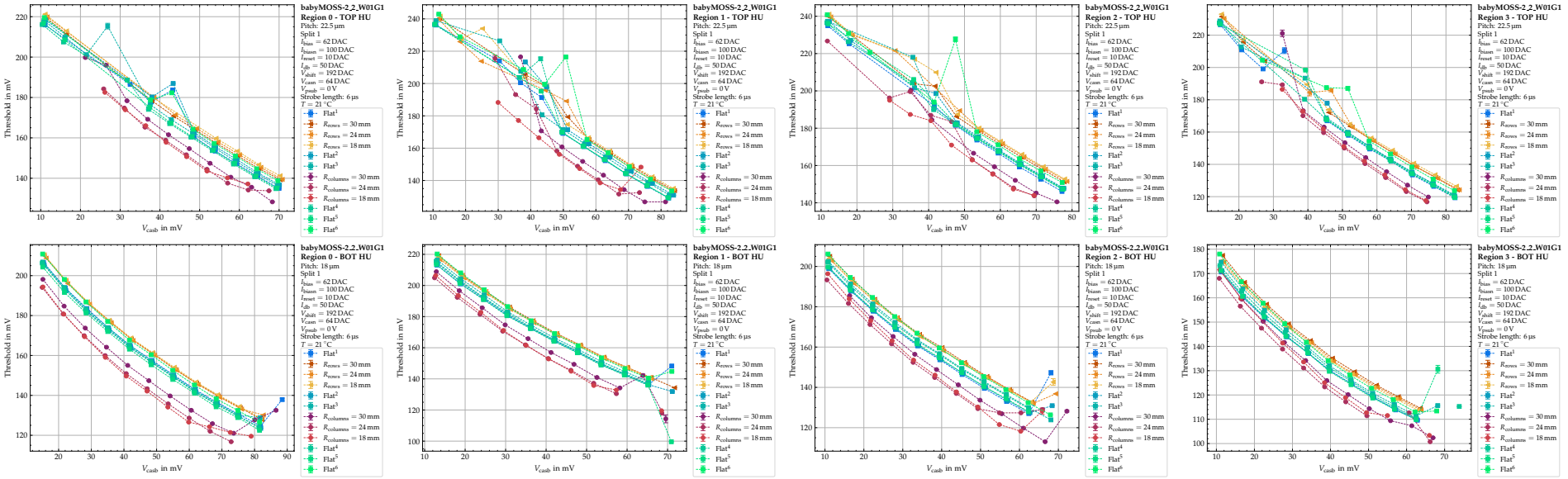

Figure A.1.10: Threshold in mV vs. V_{casb} in DAC, for babyMOSS-2_2_W01G1 with $V_{\text{psub}} = 0\,\text{V}$.

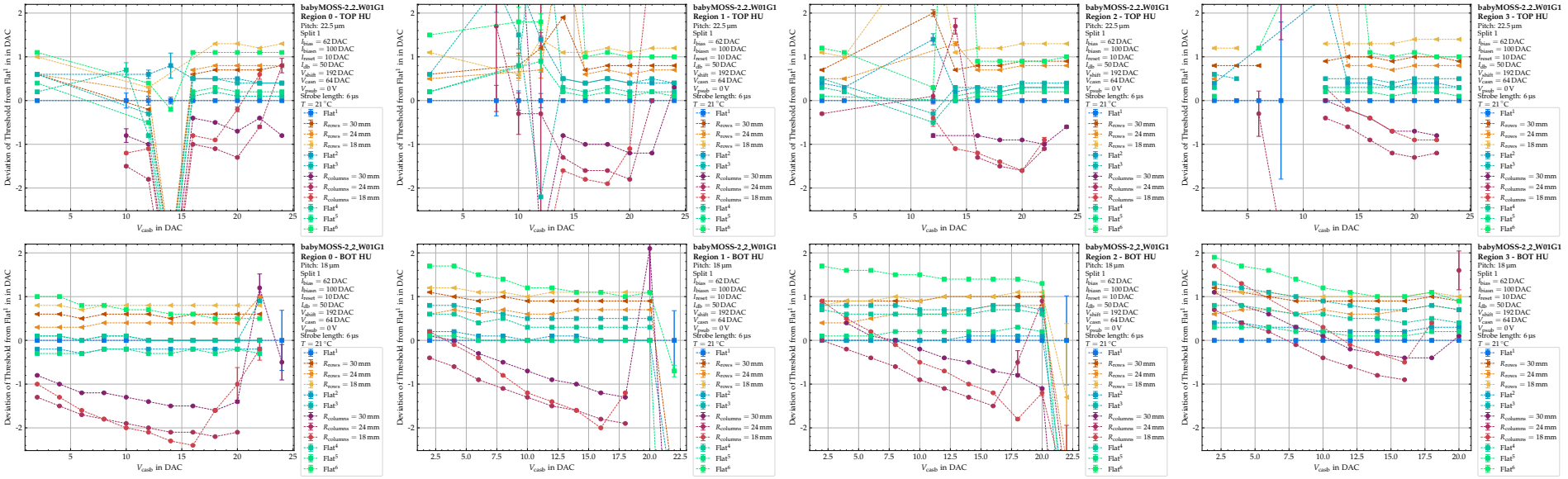

Figure A.1.11: Deviation of Threshold from Flat^1 in DAC vs. V_{casb} in DAC, for babyMOSS-2_2_W01G1 with $V_{\text{psub}} = 0\,\text{V}$.

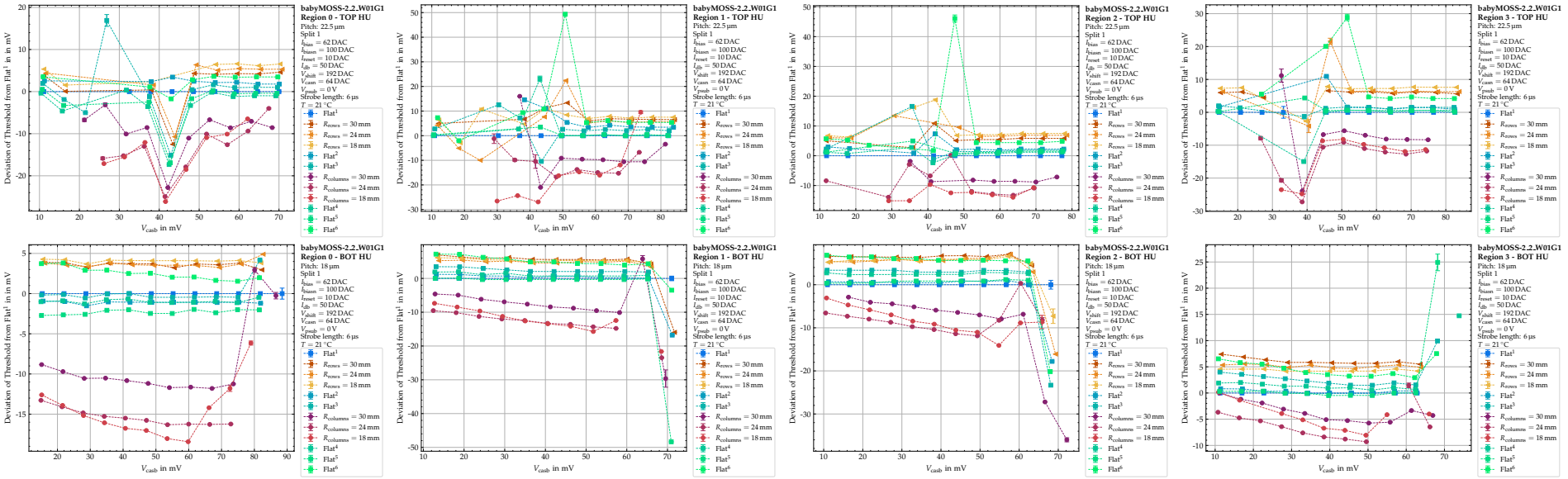

Figure A.1.12: Deviation of Threshold from Flat^1 in mV vs. V_{casb} in mV, for babyMOSS-2_2_W01G1 with $V_{\text{psub}} = 0\,\text{V}$.

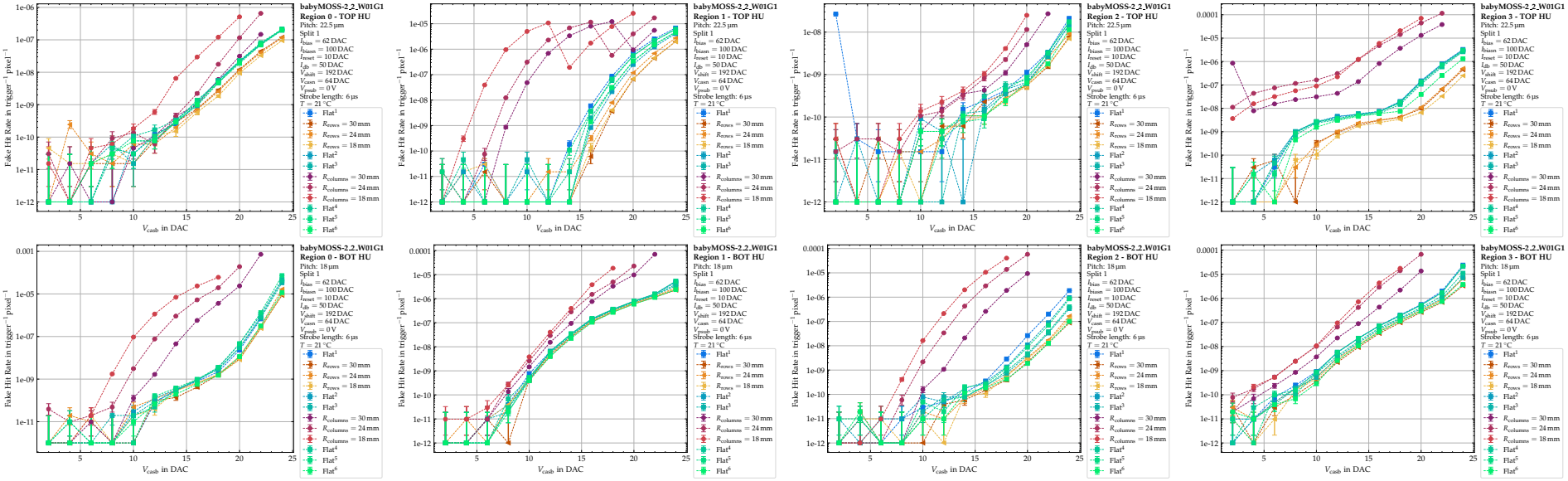

Figure A.1.13: Fake hit rate in trigger^{-1} pixel^{-1} vs. V_{casb} in DAC, for babyMOSS-2_2_W01G1 with $V_{\text{psub}} = 0\,\text{V}$.

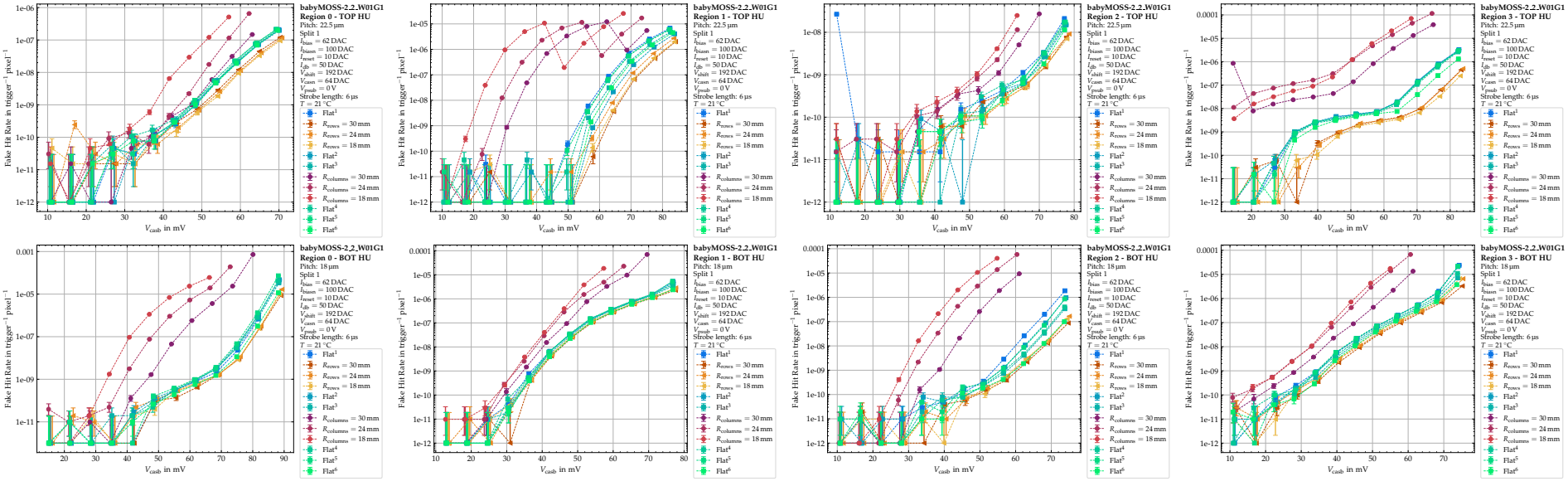

Figure A.1.14: Fake hit rate in trigger^{-1} pixel^{-1} vs. V_{casb} in mV, for babyMOSS-2_2_W01G1 with $V_{\text{psub}} = 0\,\text{V}$.

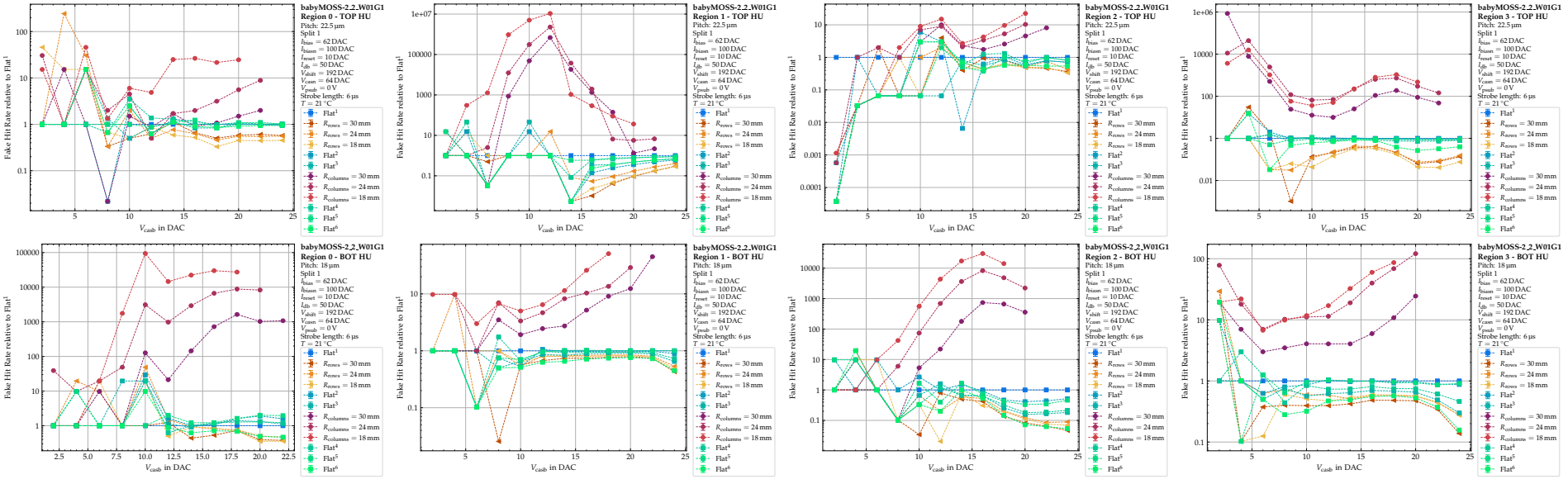

Figure A.1.15: Fake hit rate relative to Flat^1 vs. V_{casb} in DAC, for babyMOSS-2_2_W01G1 with $V_{\text{psub}} = 0\,\text{V}$.

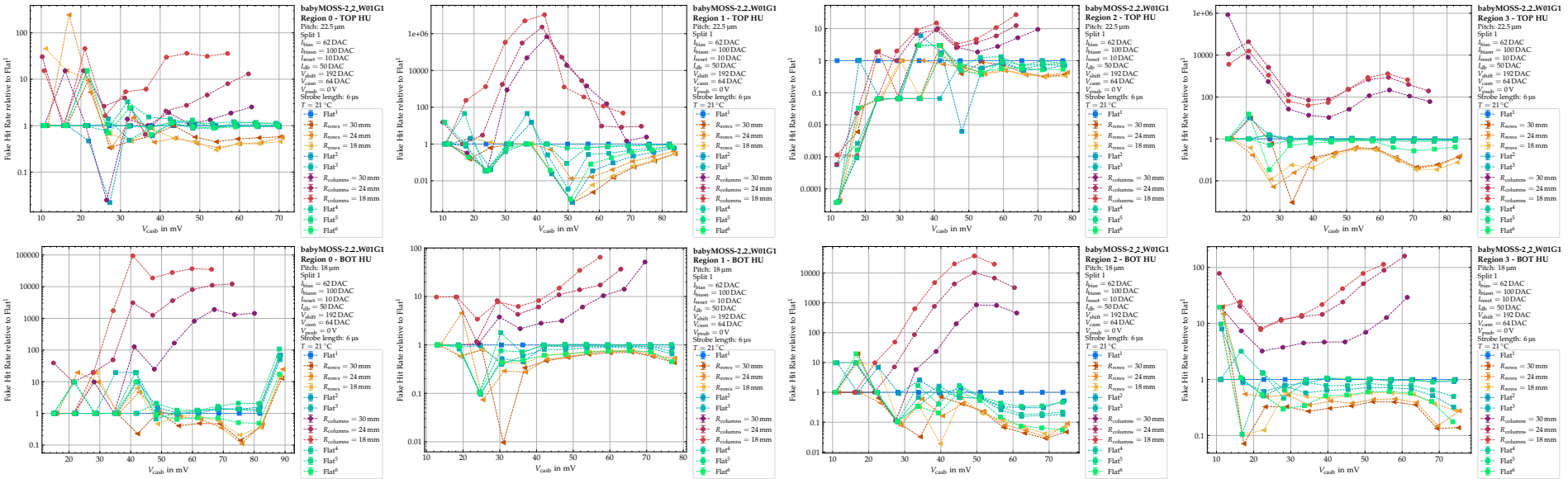

Figure A.1.16: Fake hit rate relative to Flat^1 vs. V_{casb} in mV, for babyMOSS-2_2_W01G1 with $V_{\text{psub}} = 0\,\text{V}$.

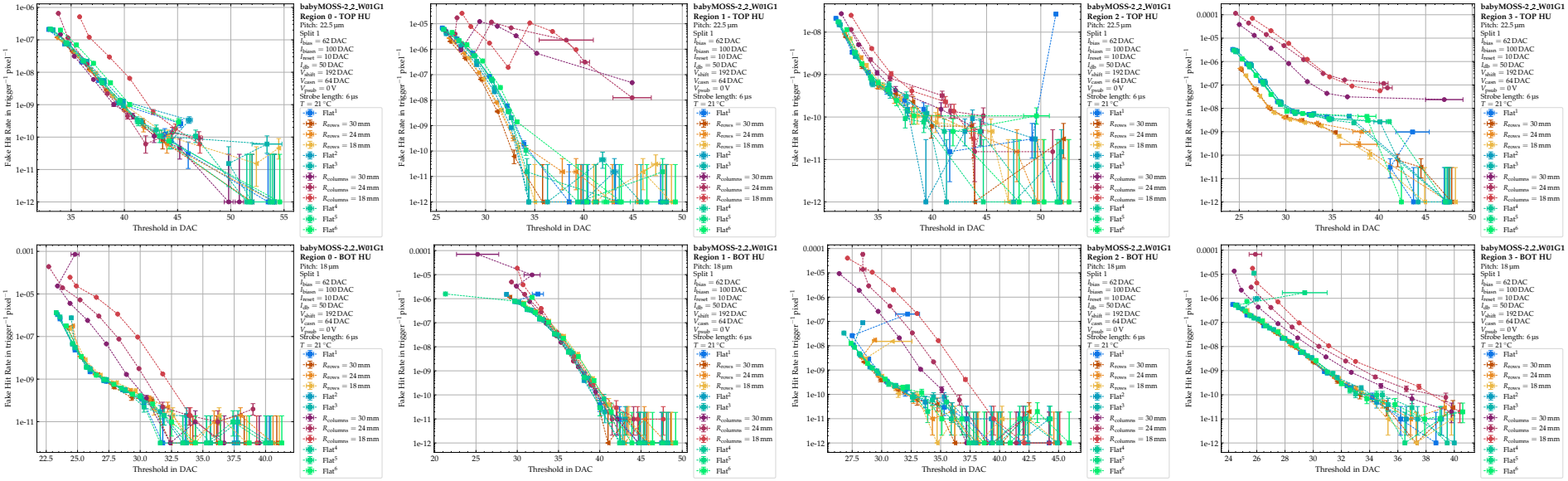

Figure A.1.17: Fake hit rate in trigger^{-1} pixel^{-1} vs. Threshold in DAC, for babyMOSS-2_2_W01G1 with $V_{\text{psub}} = 0\,\text{V}$.

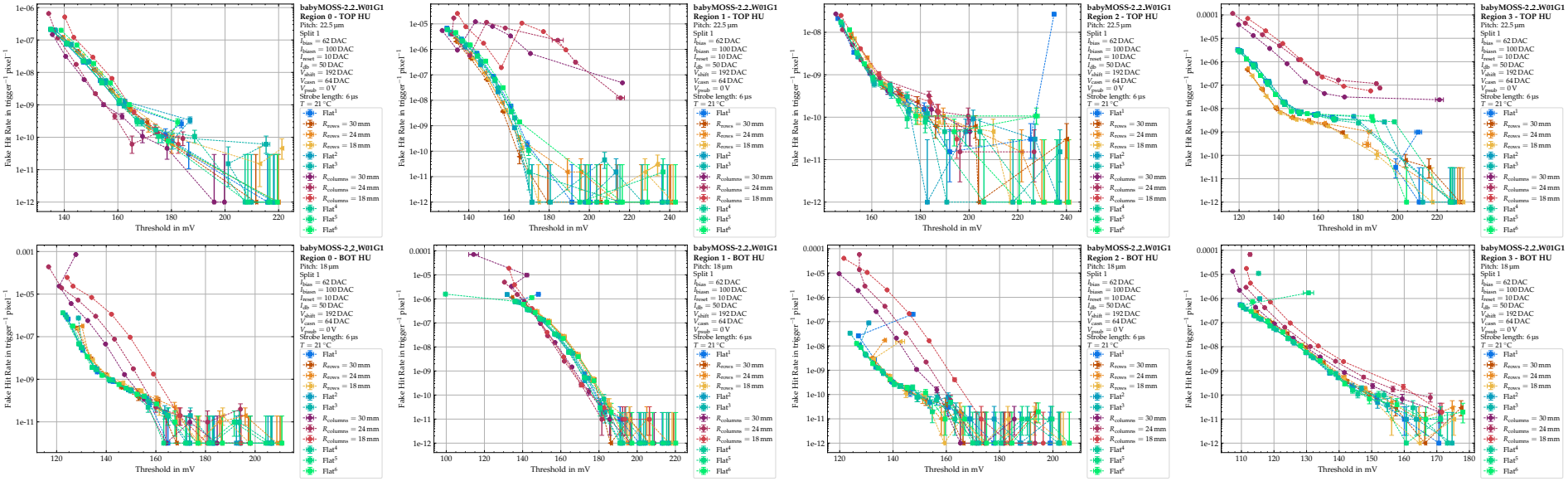

Figure A.1.18: Fake hit rate in trigger^{-1} pixel^{-1} vs. Threshold in mV, for babyMOSS-2_2_W01G1 with $V_{\text{psub}} = 0\,\text{V}$.

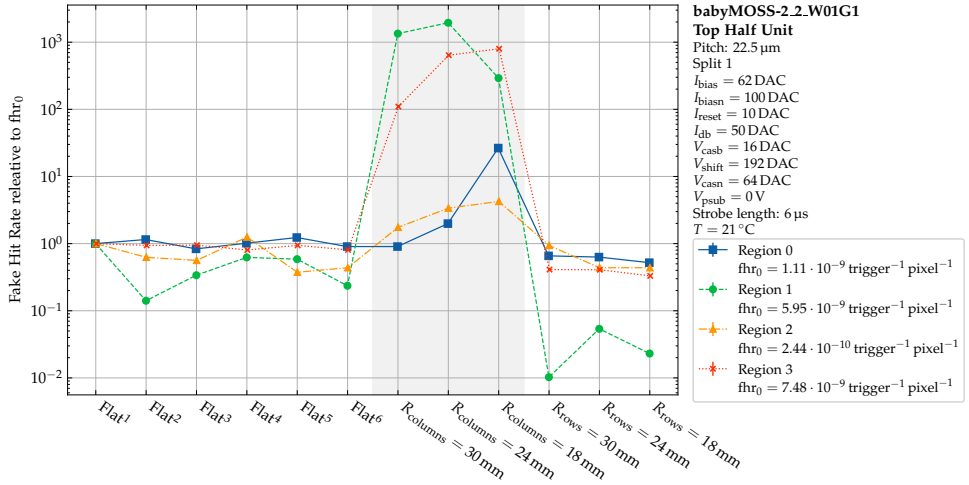

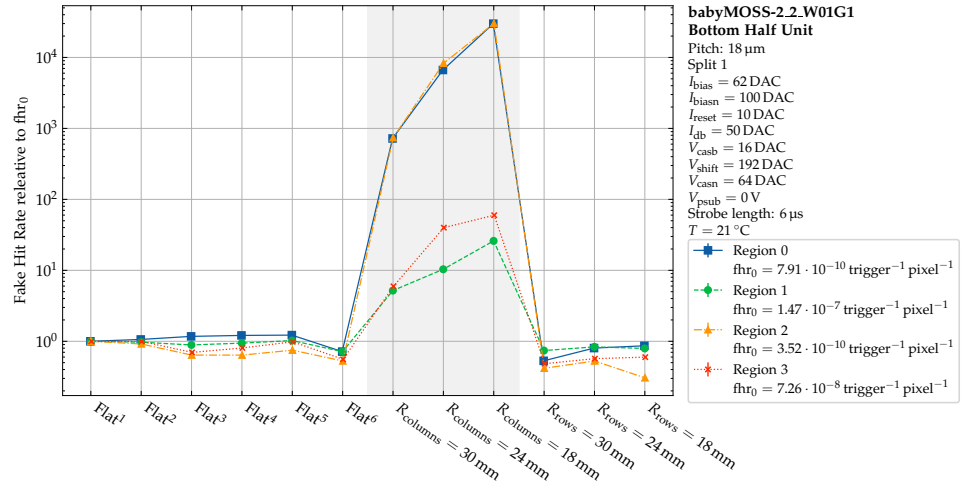

Figure A.1.19: Fake hit rate relative to fhr$_0$ vs. configuration, for $V_{casb} = 16\,\text{DAC}$, babyMOSS-2_2_W01G1 with $V_{psub} = 0\,\text{V}$.

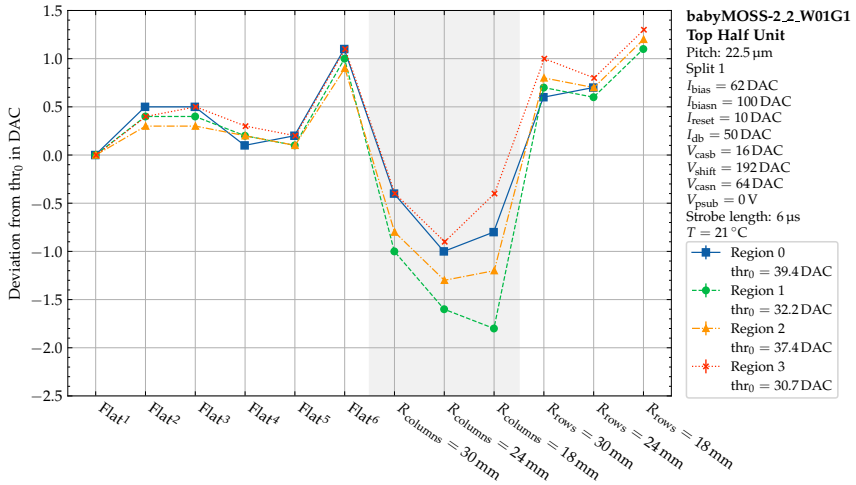

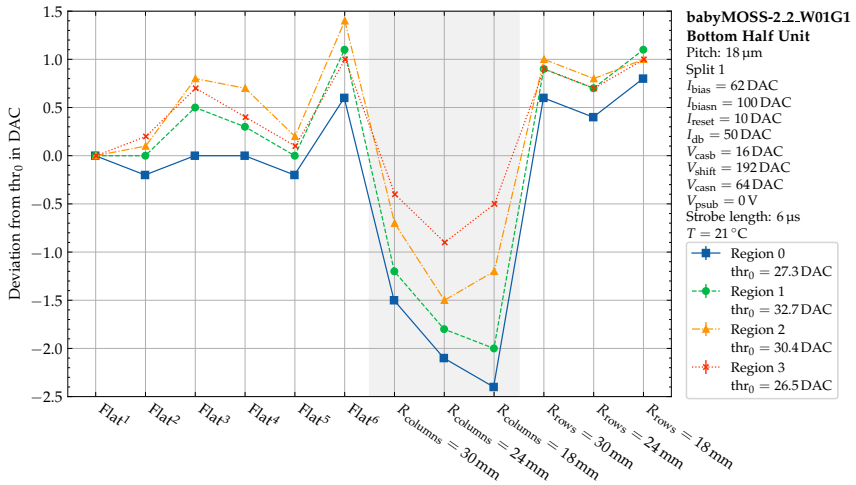

Figure A.1.20: Deviation of Threshold from thr$_0$ in DAC vs. configuration, $V_{casb} = 16\,\text{DAC}$, babyMOSS-2_2_W01G1 with $V_{psub} = 0\,\text{V}$.

A.2 babyMOSS-4_5_W01G1

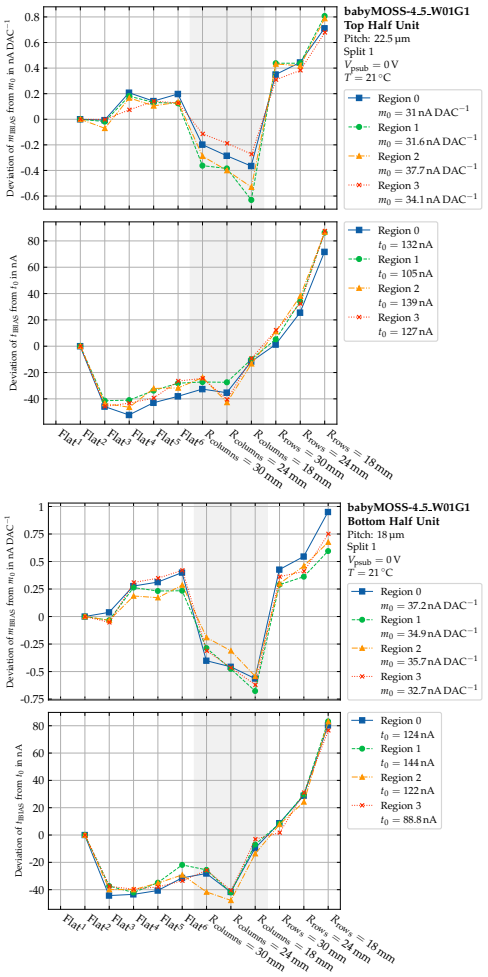

Figure A.2.1: Changes of slope and offset for the I_{bias}-DAC vs. configuration, for babyMOSS-4_5_W01G1 with $V_{\text{psub}} = 0\,\text{V}$.

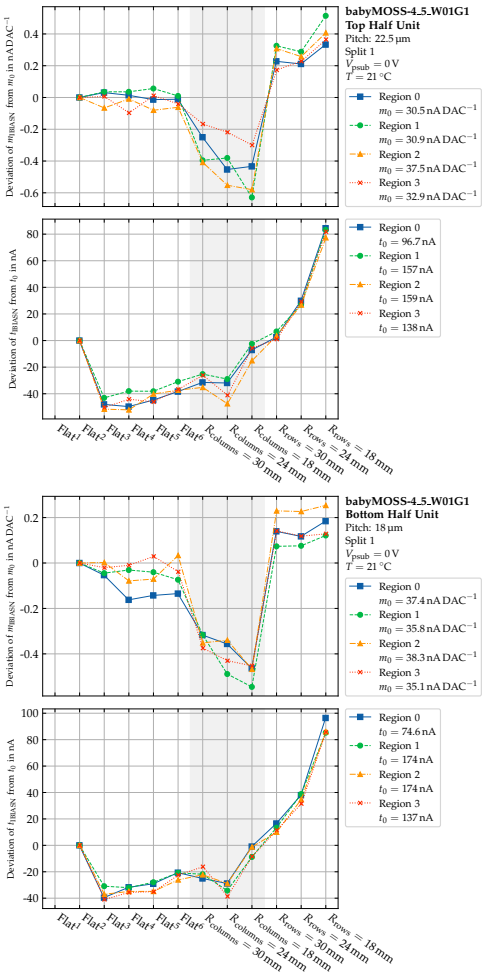

Figure A.2.2: Changes of slope and offset for the I_{biasn}-DAC vs. configuration, for babyMOSS-4_5_W01G1 with $V_{\text{psub}} = 0\,\text{V}$.

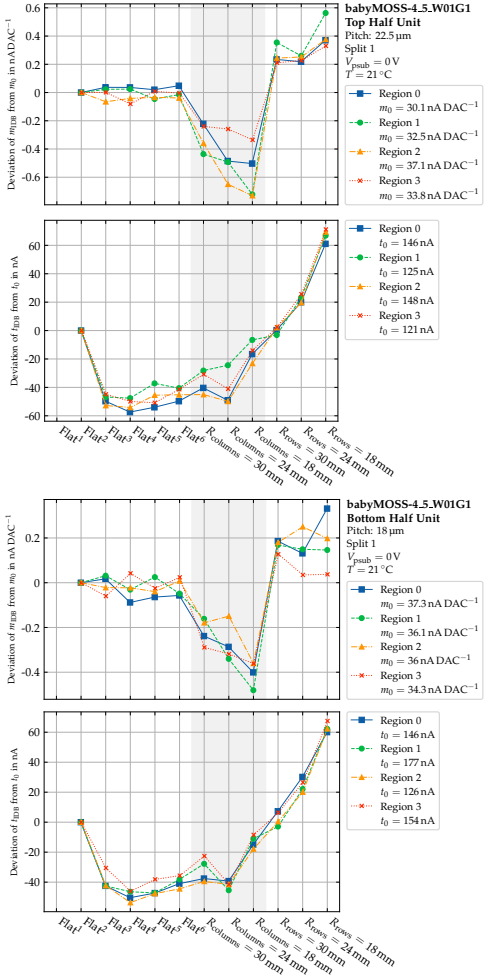

Figure A.2.3: Changes of slope and offset for the I_{db}-DAC vs. configuration, for babyMOSS-4_5_W01G1 with $V_{\text{psub}} = 0\,\text{V}$.

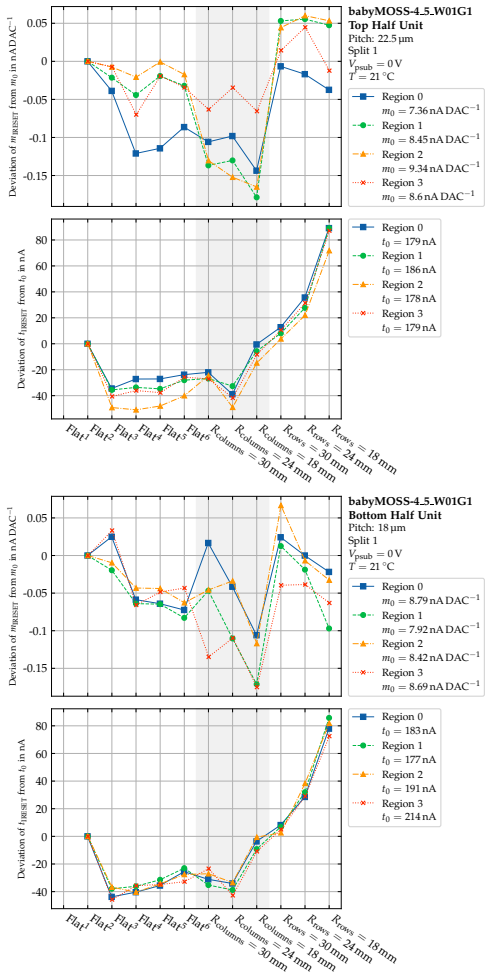

Figure A.2.4: Changes of slope and offset for the I_{reset}-DAC vs. configuration, for babyMOSS-4_5_W01G1 with $V_{\text{psub}} = 0\,\text{V}$.

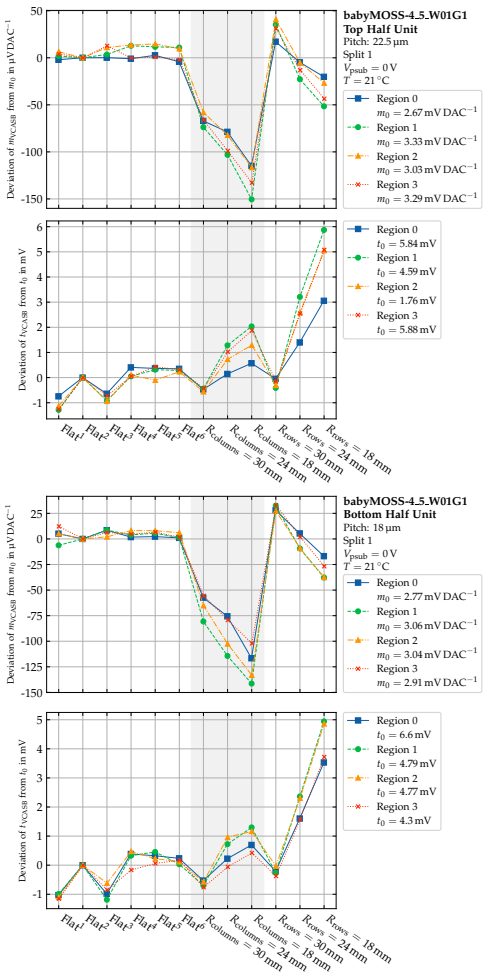

Figure A.2.5: Changes of slope and offset for the V_{casb}-DAC vs. configuration, for babyMOSS-4_5_W01G1 with $V_{\text{psub}} = 0\,\text{V}$.

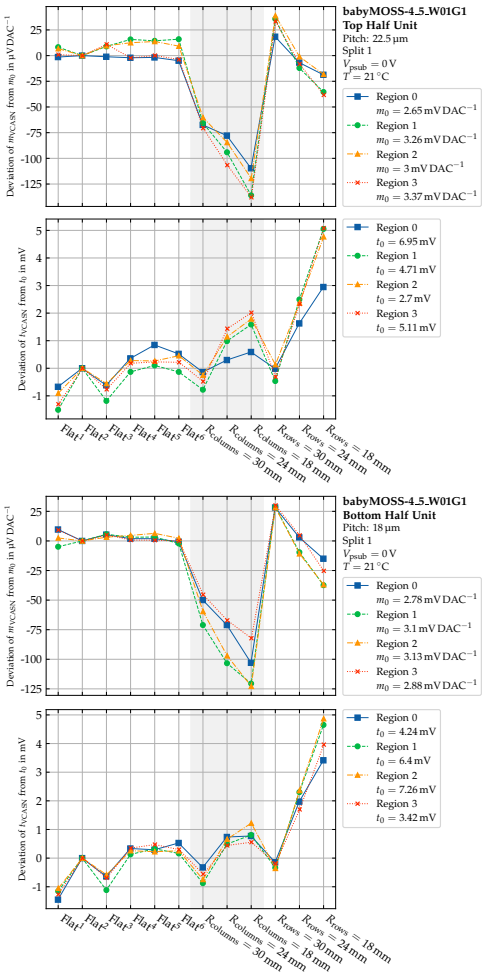

Figure A.2.6: Changes of slope and offset for the V_{casn}-DAC vs. configuration, for babyMOSS-4_5_W01G1 with $V_{\text{psub}} = 0\,\text{V}$.

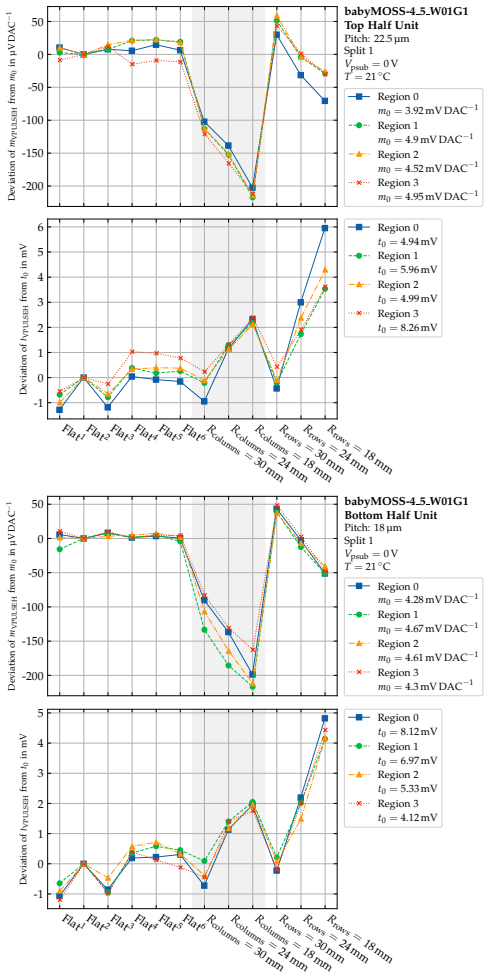

Figure A.2.7: Changes of slope and offset for the V_{pulseh}-DAC vs. configuration, for babyMOSS-4_5_W01G1 with $V_{\text{psub}} = 0\,\text{V}$.

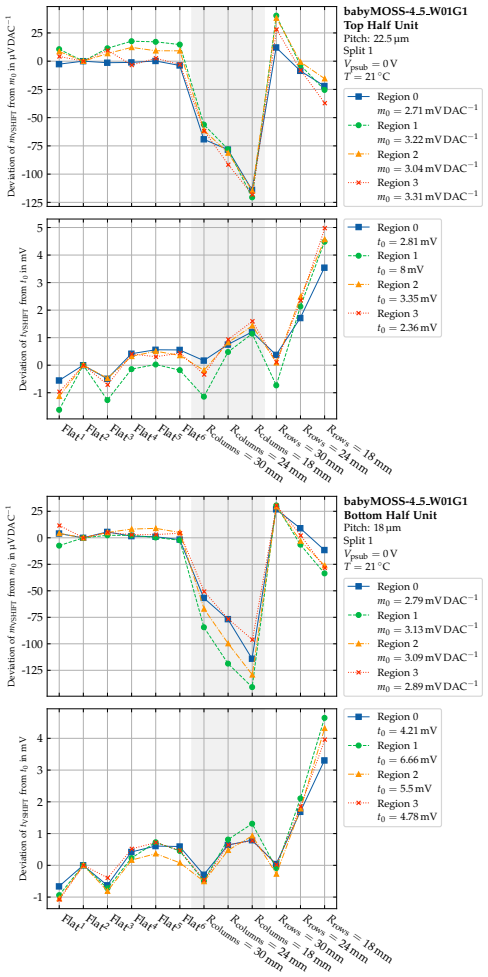

Figure A.2.8: Changes of slope and offset for the V_{shift}-DAC vs. configuration, for babyMOSS-4_5_W01G1 with $V_{\text{psub}} = 0\,\text{V}$.

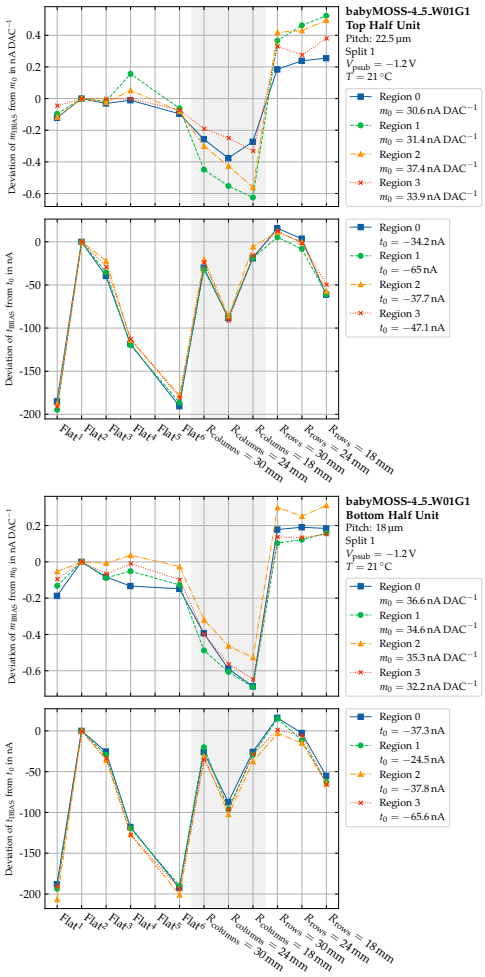

Figure A.2.9: Changes of slope and offset for the I_{bias}-DAC vs. configuration, for babyMOSS-4_5_W01G1 with $V_{\text{psub}} = -1.2\,\text{V}$.

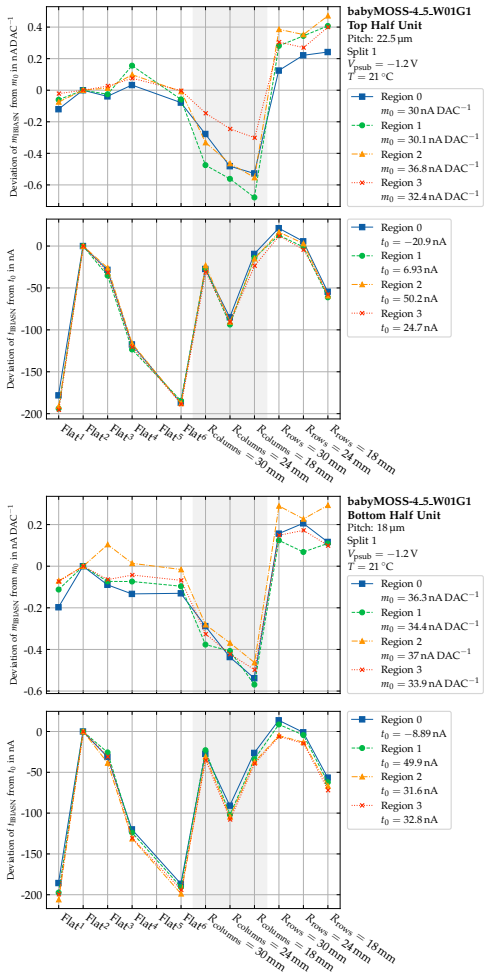

Figure A.2.10: Changes of slope and offset for the I_{biasn}-DAC vs. configuration, for babyMOSS-4_5_W01G1 with $V_{\text{psub}} = -1.2\,\text{V}$.

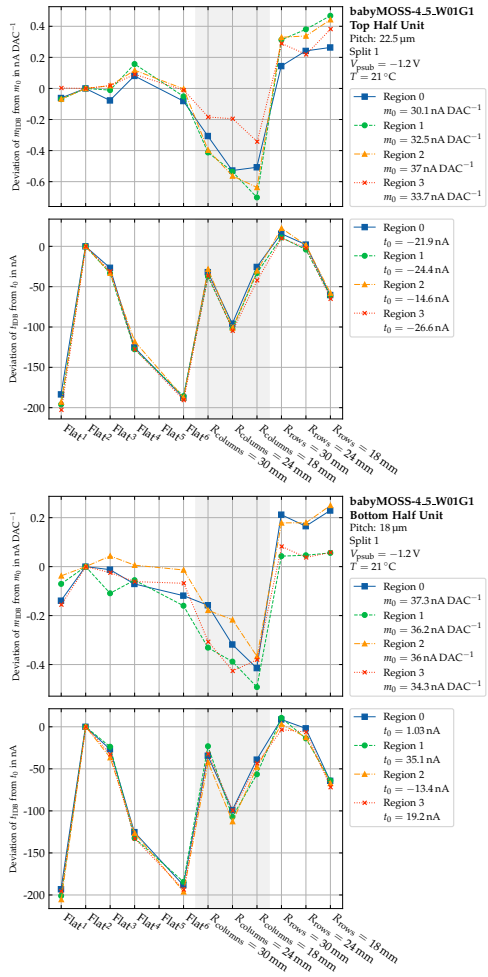

Figure A.2.11: Changes of slope and offset for the I_{db}-DAC vs. configuration, for babyMOSS-4_5_W01G1 with $V_{\text{psub}} = -1.2\,\text{V}$.

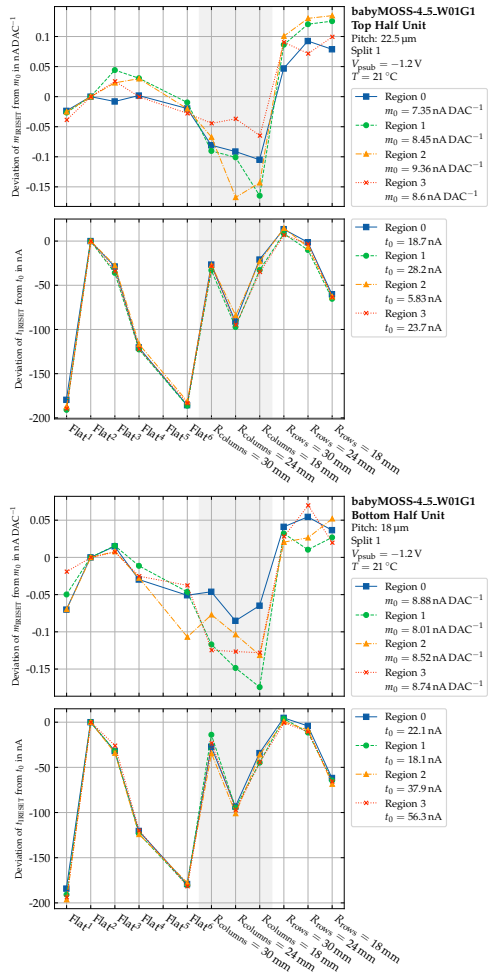

Figure A.2.12: Changes of slope and offset for the I_{reset}-DAC vs. configuration, for babyMOSS-4_5_W01G1 with $V_{\text{psub}} = -1.2\,\text{V}$.

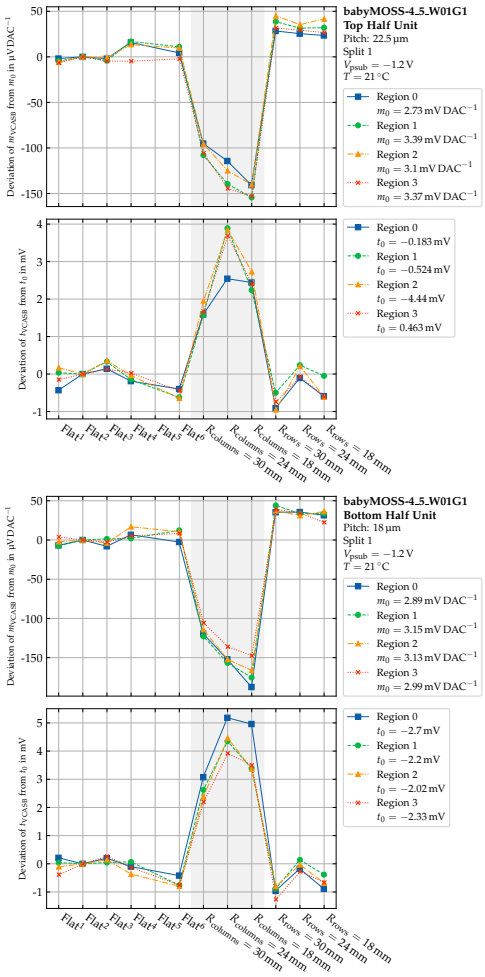

Figure A.2.13: Changes of slope and offset for the V_{casb}-DAC vs. configuration, for babyMOSS-4_5_W01G1 with $V_{psub} = -1.2$ V.

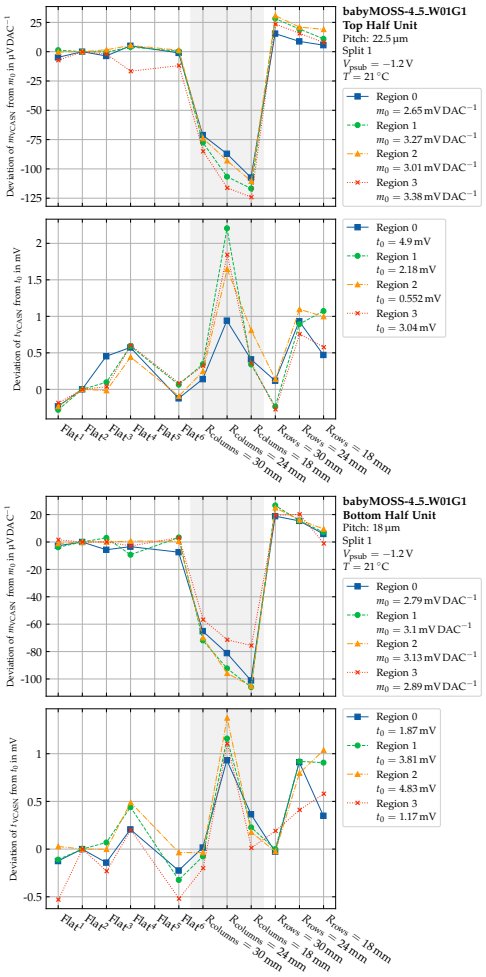

Figure A.2.14: Changes of slope and offset for the V_{casn}-DAC vs. configuration, for babyMOSS-4_5_W01G1 with $V_{psub} = -1.2$ V.

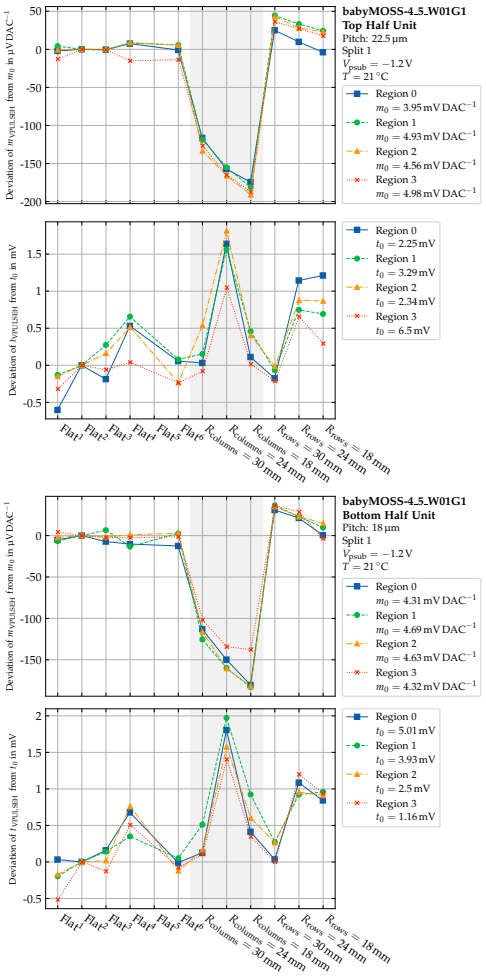

Figure A.2.15: Changes of slope and offset for the V_{pulseh}-DAC vs. configuration, for babyMOSS-4_5_W01G1 with $V_{psub} = -1.2$ V.

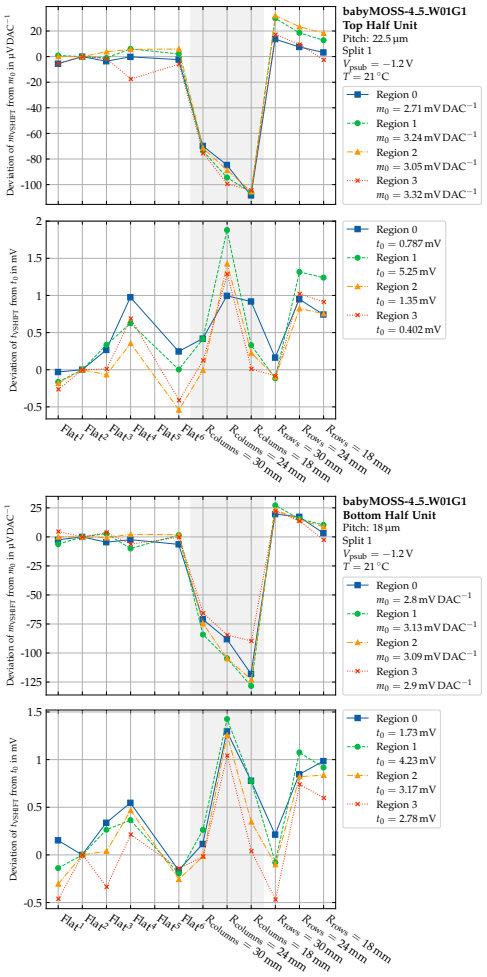

Figure A.2.16: Changes of slope and offset for the V_{shift}-DAC vs. configuration, for babyMOSS-4_5_W01G1 with $V_{psub} = -1.2$ V.

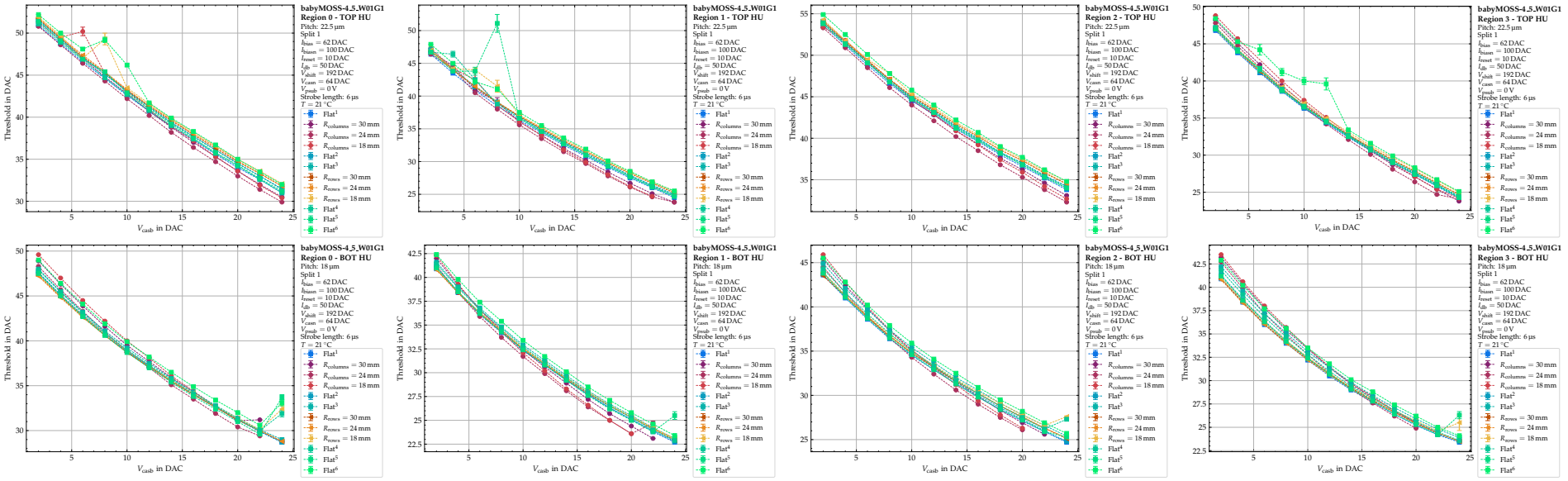

Figure A.2.17: Threshold in DAC vs. V_{casb} in DAC, for babyMOSS-4_5_W01G1 with $V_{\text{psub}} = 0\,\text{V}$.

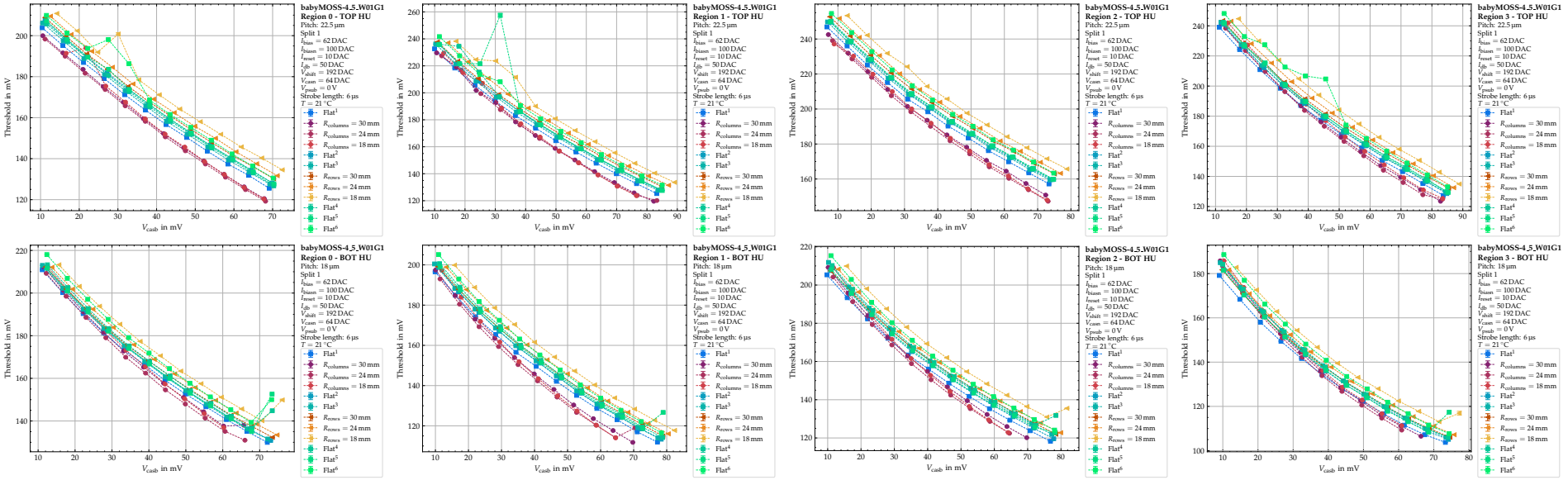

Figure A.2.18: Threshold in mV vs. V_{casb} in DAC, for babyMOSS-4_5_W01G1 with $V_{\text{psub}} = 0\,\text{V}$.

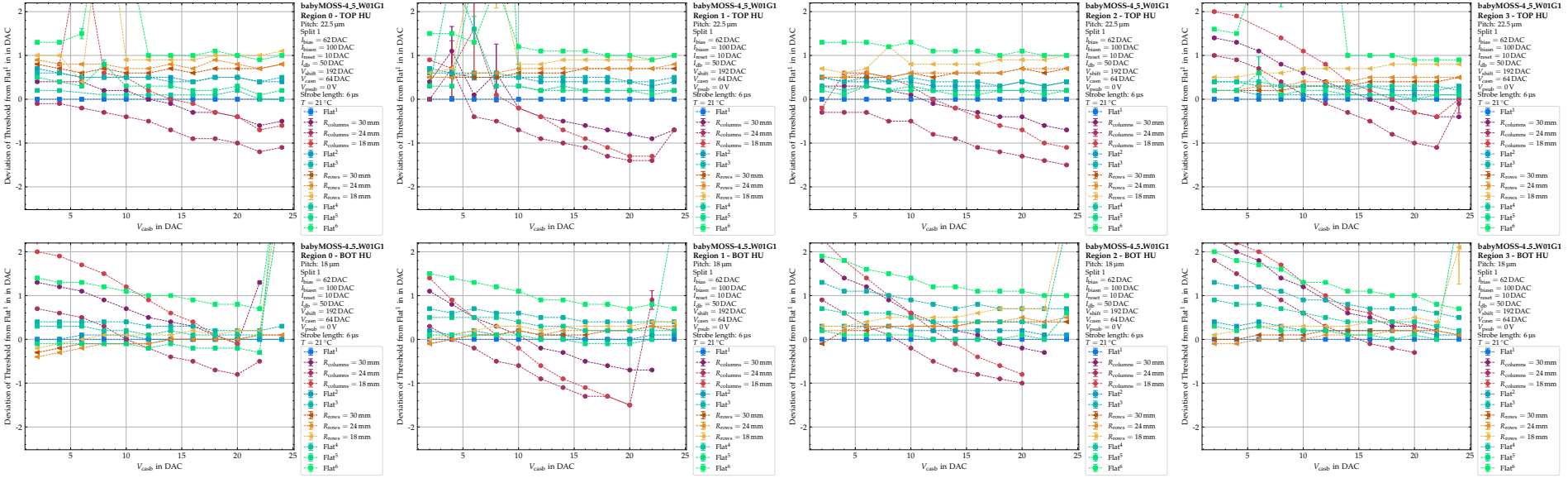

Figure A.2.19: Deviation of Threshold from Flat^1 in DAC vs. V_{casb} in DAC, for babyMOSS-4_5_W01G1 with $V_{\text{psub}} = 0\,\text{V}$.

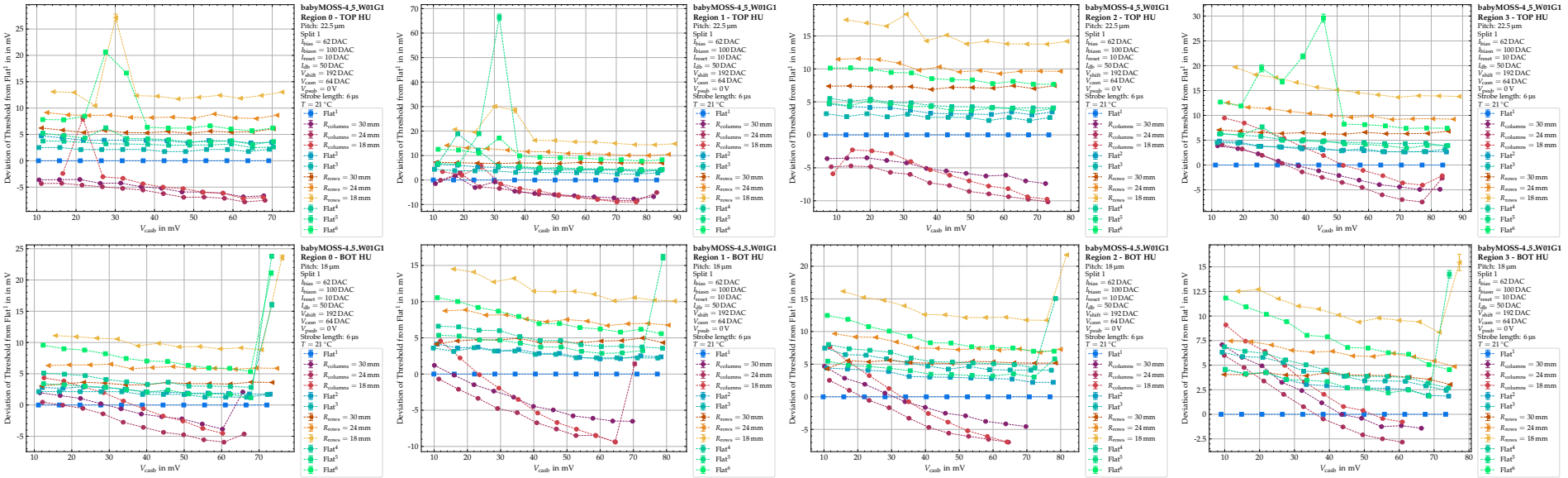

Figure A.2.20: Deviation of Threshold from Flat^1 in mV vs. V_{casb} in mV, for babyMOSS-4_5_W01G1 with $V_{\text{psub}} = 0\,\text{V}$.

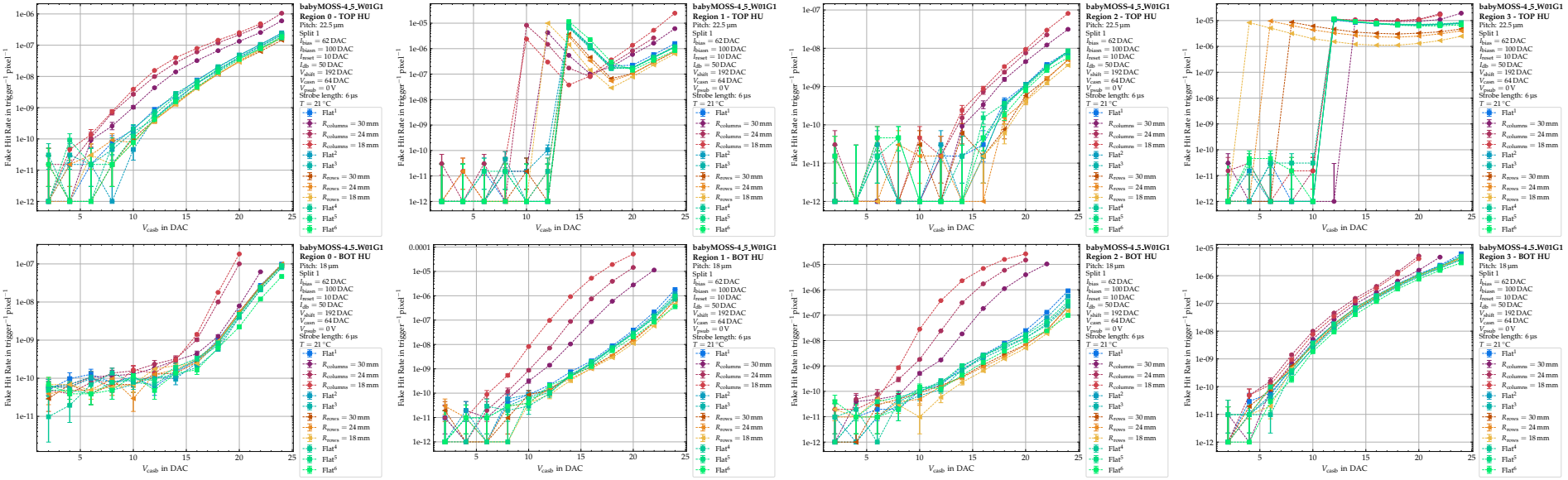

Figure A.2.21: Fake hit rate in trigger^{-1} pixel^{-1} vs. V_{casb} in DAC, for babyMOSS-4_5_W01G1 with $V_{\text{psub}} = 0\,\text{V}$.

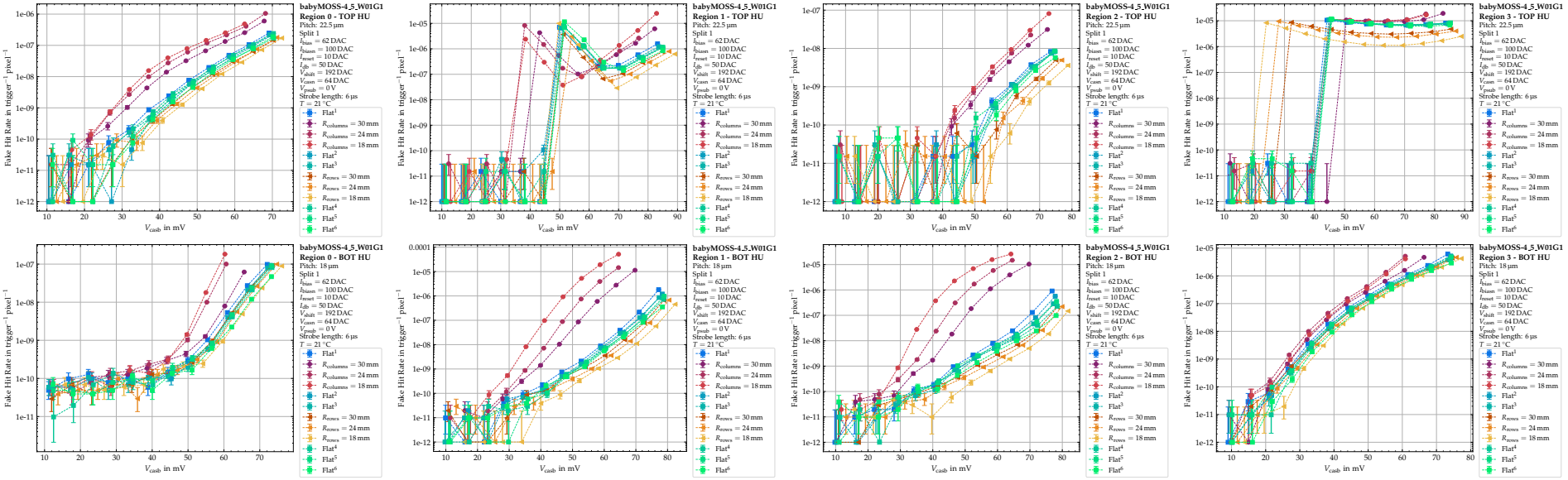

Figure A.2.22: Fake hit rate in trigger^{-1} pixel^{-1} vs. V_{casb} in mV, for babyMOSS-4_5_W01G1 with $V_{\text{psub}} = 0\,\text{V}$.

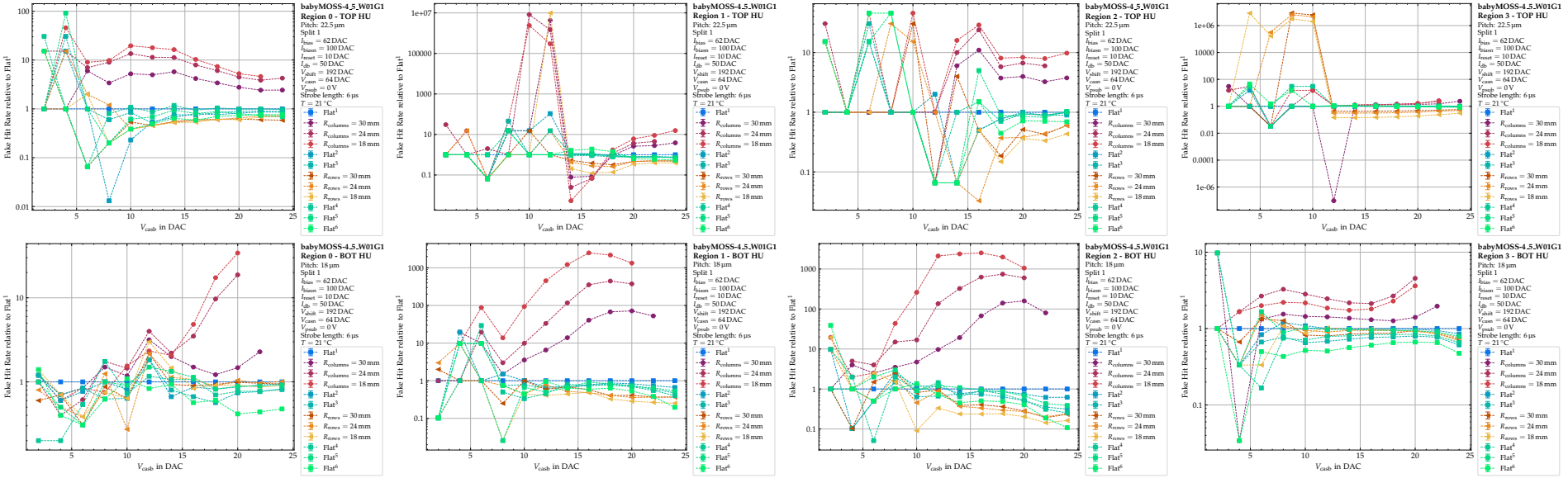

Figure A.2.23: Fake hit rate relative to Flat^1 vs. V_{casb} in DAC, for babyMOSS-4_5_W01G1 with $V_{\text{psub}} = 0\,\text{V}$.

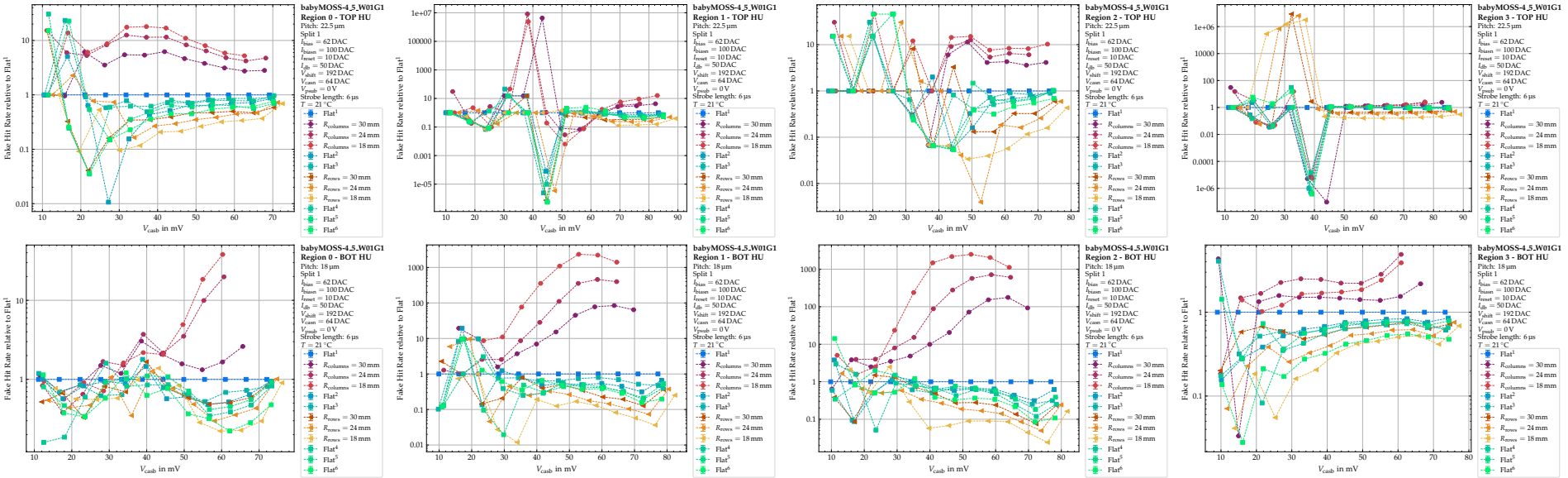

Figure A.2.24: Fake hit rate relative to Flat^1 vs. V_{casb} in mV, for babyMOSS-4_5_W01G1 with $V_{\text{psub}} = 0\,\text{V}$.

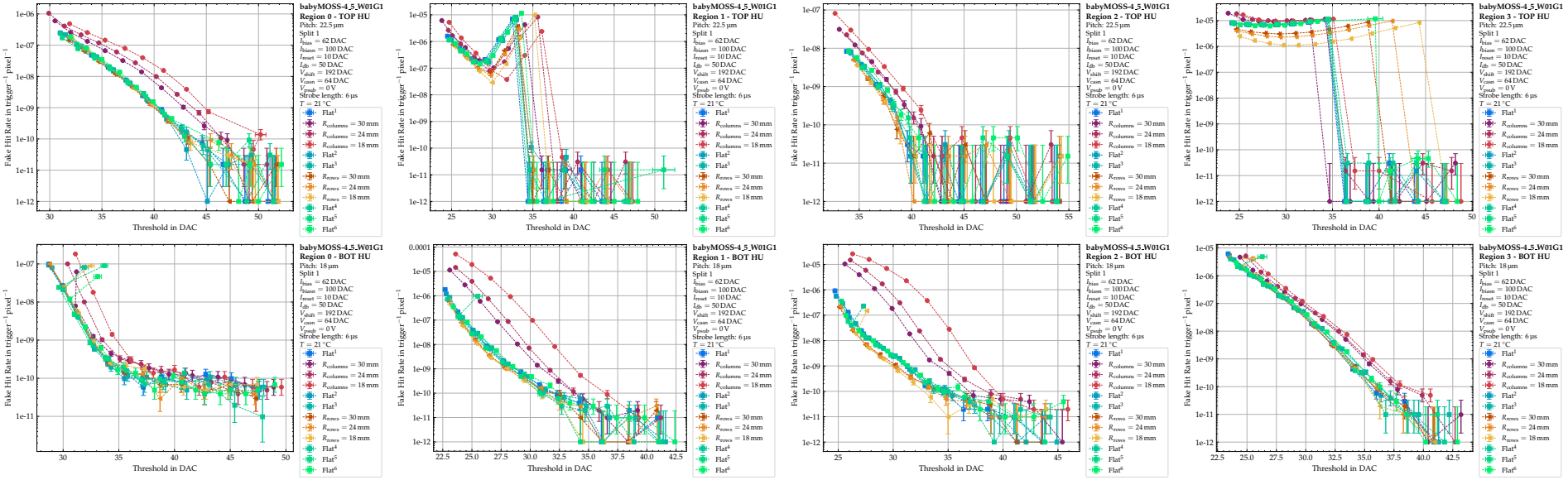

Figure A.2.25: Fake hit rate in trigger^{-1} pixel^{-1} vs. Threshold in DAC, for babyMOSS-4_5_W01G1 with $V_{\text{psub}} = 0\,\text{V}$.

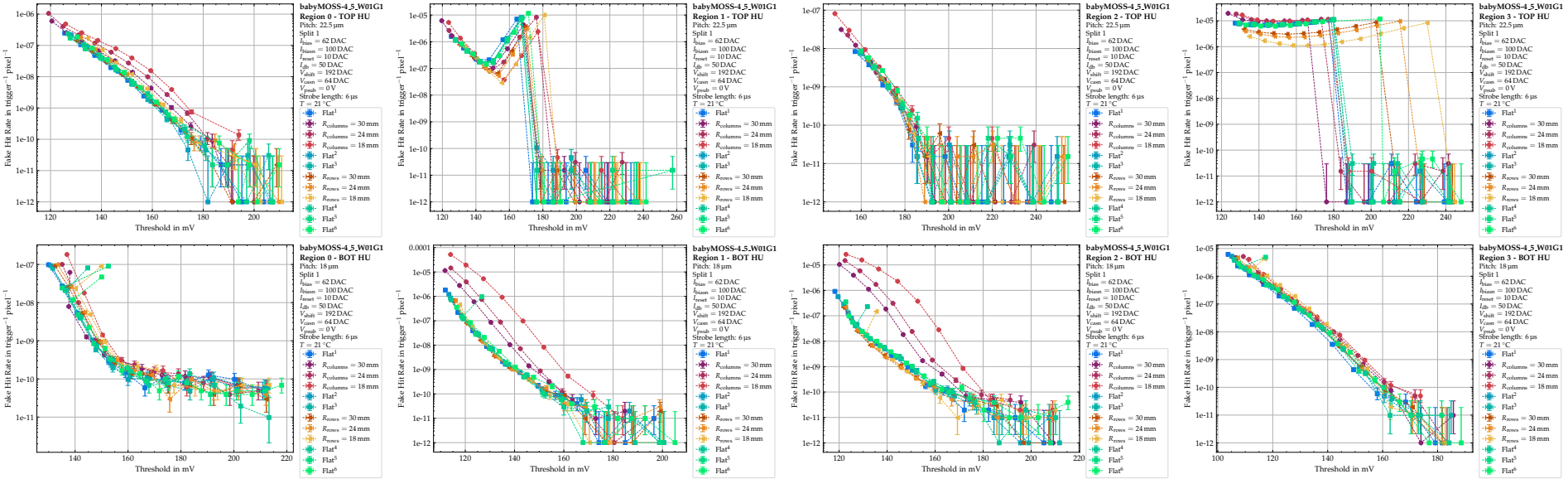

Figure A.2.26: Fake hit rate in trigger^{-1} pixel^{-1} vs. Threshold in mV, for babyMOSS-4_5_W01G1 with $V_{\text{psub}} = 0\,\text{V}$.

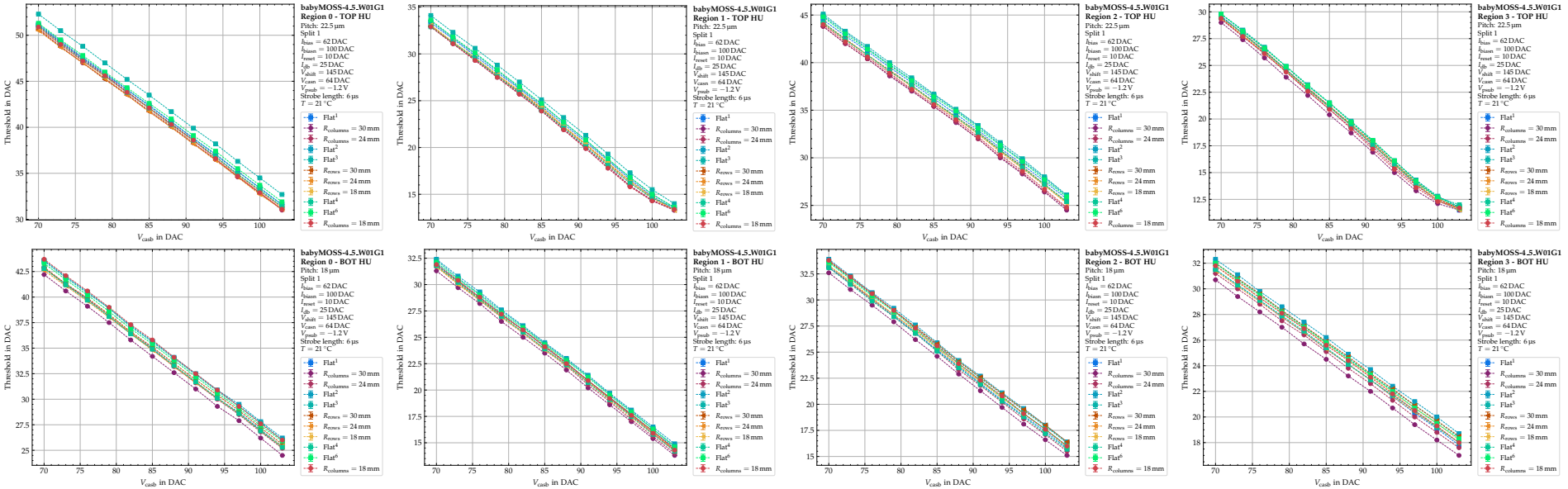

Figure A.2.27: Threshold in DAC vs. V_{casb} in DAC, for babyMOSS-4_5_W01G1 with $V_{\text{psub}} = -1.2\,\text{V}$.

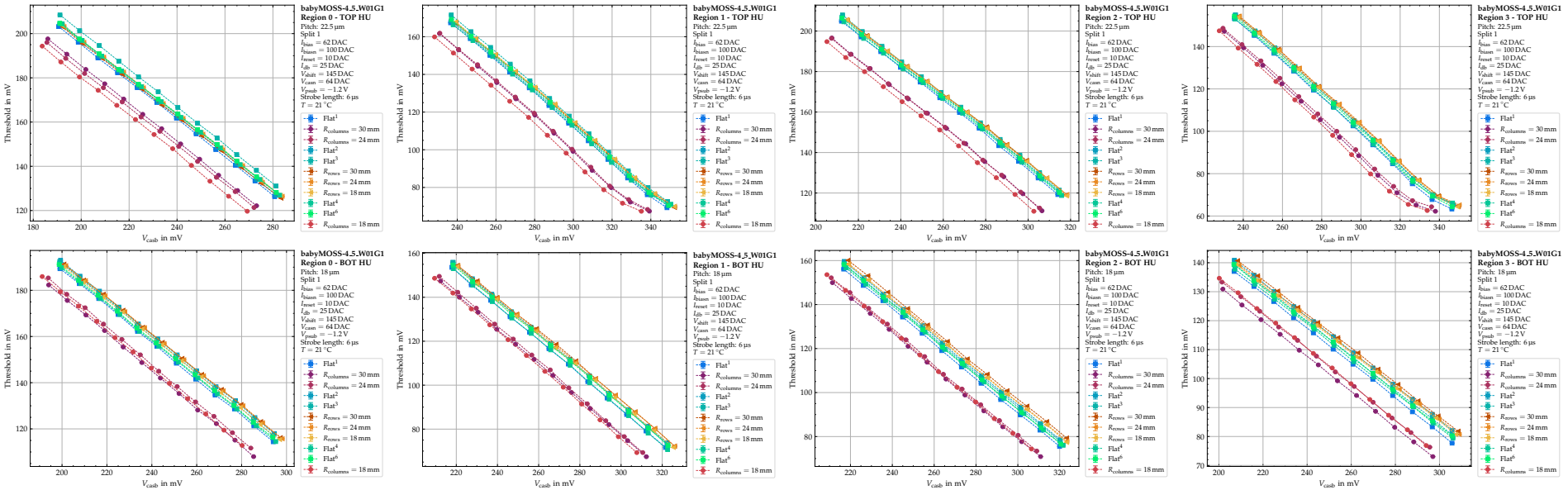

Figure A.2.28: Threshold in mV vs. V_{casb} in DAC, for babyMOSS-4_5_W01G1 with $V_{\text{psub}} = -1.2\,\text{V}$.

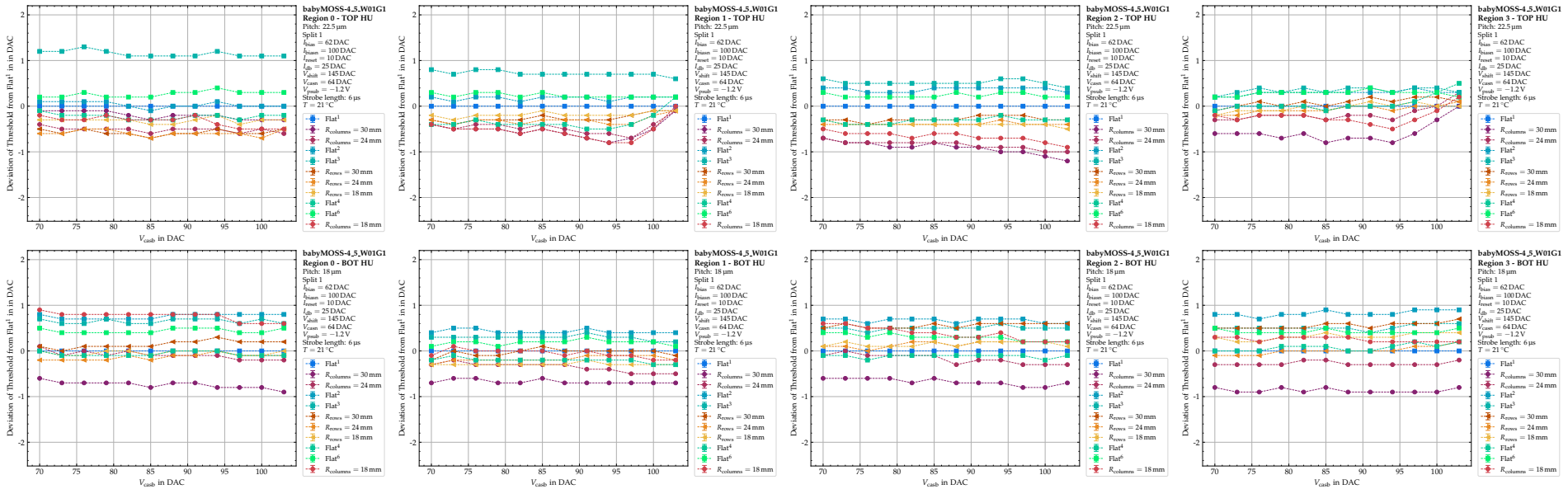

Figure A.2.29: Deviation of Threshold from Flat^1 in DAC vs. V_{casb} in DAC, for babyMOSS-4_5_W01G1 with $V_{\text{psub}} = -1.2\,\text{V}$.

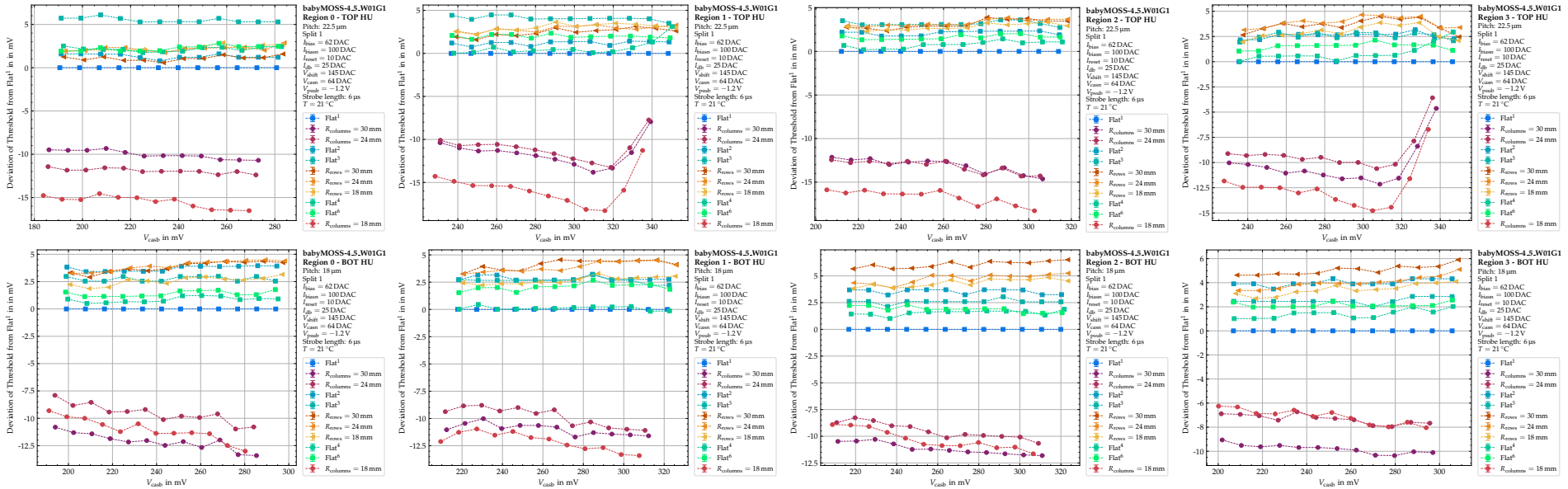

Figure A.2.30: Deviation of Threshold from Flat^1 in mV vs. V_{casb} in mV, for babyMOSS-4_5_W01G1 with $V_{\text{psub}} = -1.2\,\text{V}$.

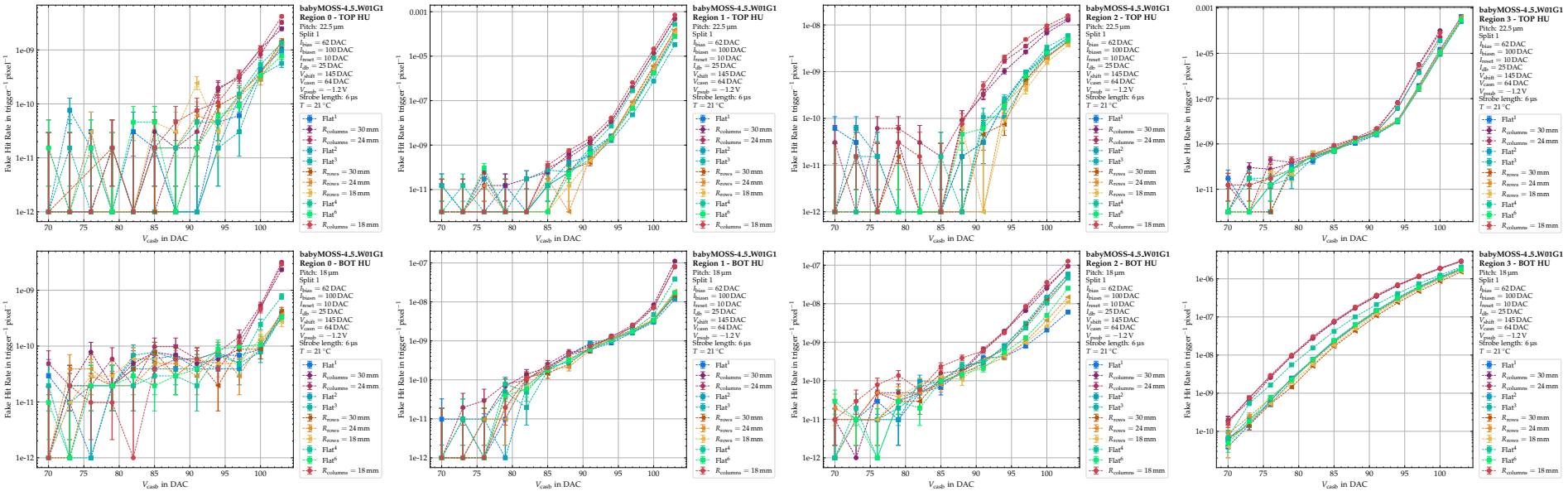

Figure A.2.31: Fake hit rate in trigger^{-1} pixel^{-1} vs. V_{casb} in DAC, for babyMOSS-4_5_W01G1 with $V_{\mathrm{psub}} = -1.2\,\mathrm{V}$.

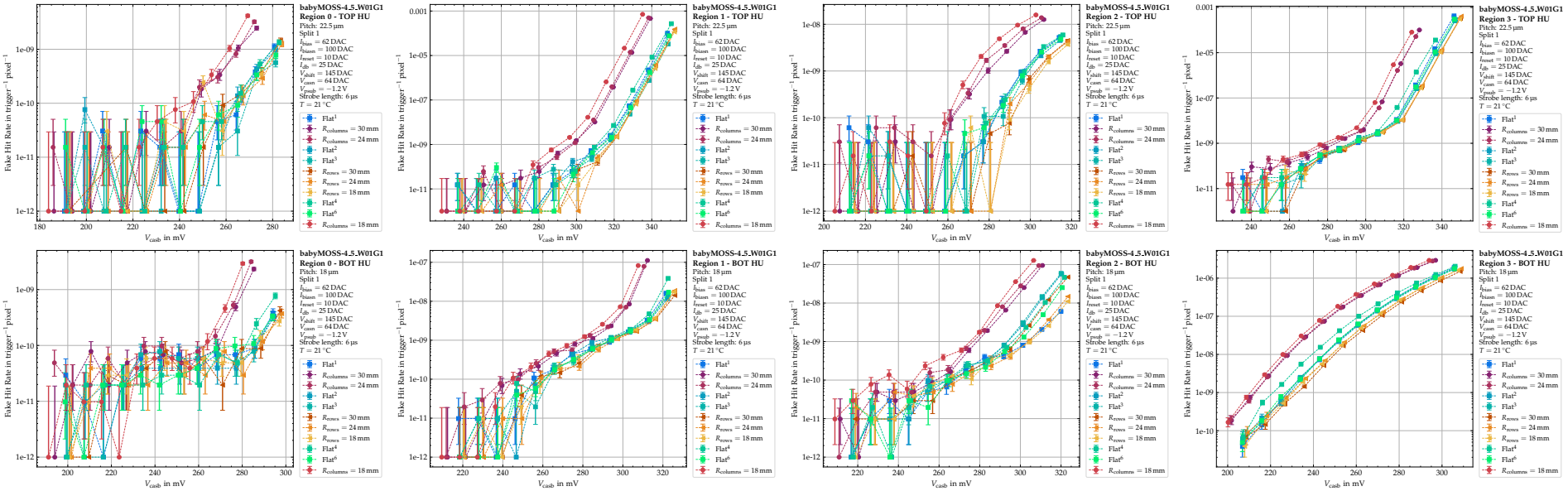

Figure A.2.32: Fake hit rate in trigger^{-1} pixel^{-1} vs. V_{casb} in mV, for babyMOSS-4_5_W01G1 with $V_{\mathrm{psub}} = -1.2\,\mathrm{V}$.

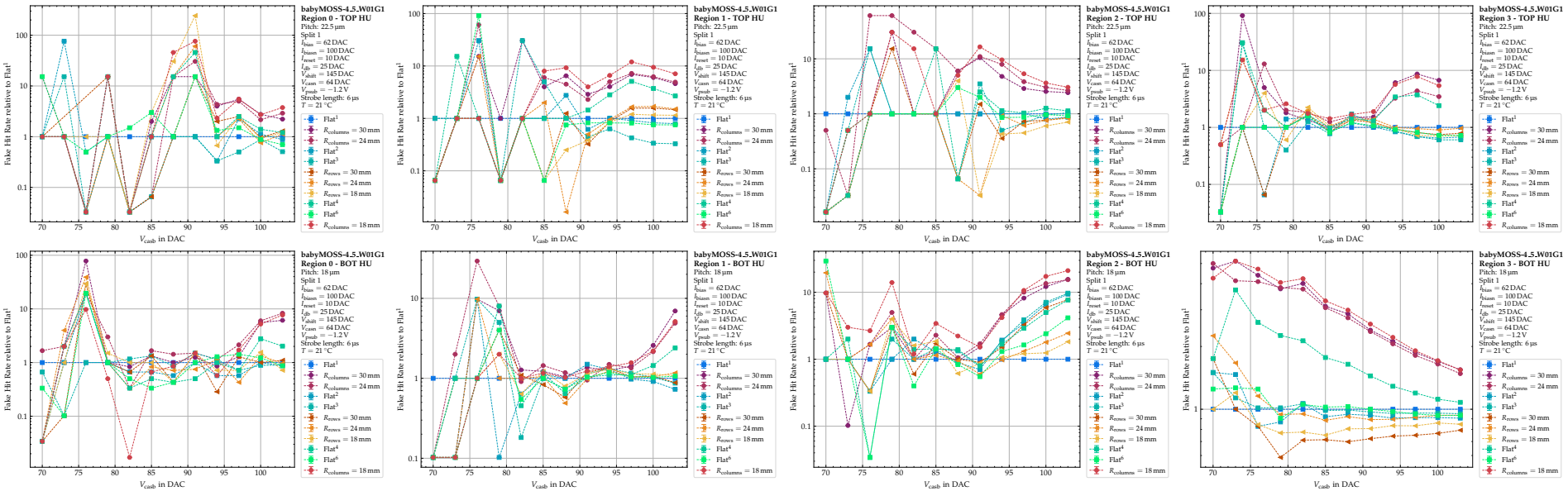

Figure A.2.33: Fake hit rate relative to Flat^1 vs. V_{casb} in DAC, for babyMOSS-4_5_W01G1 with $V_{\text{psub}} = -1.2\,\text{V}$.

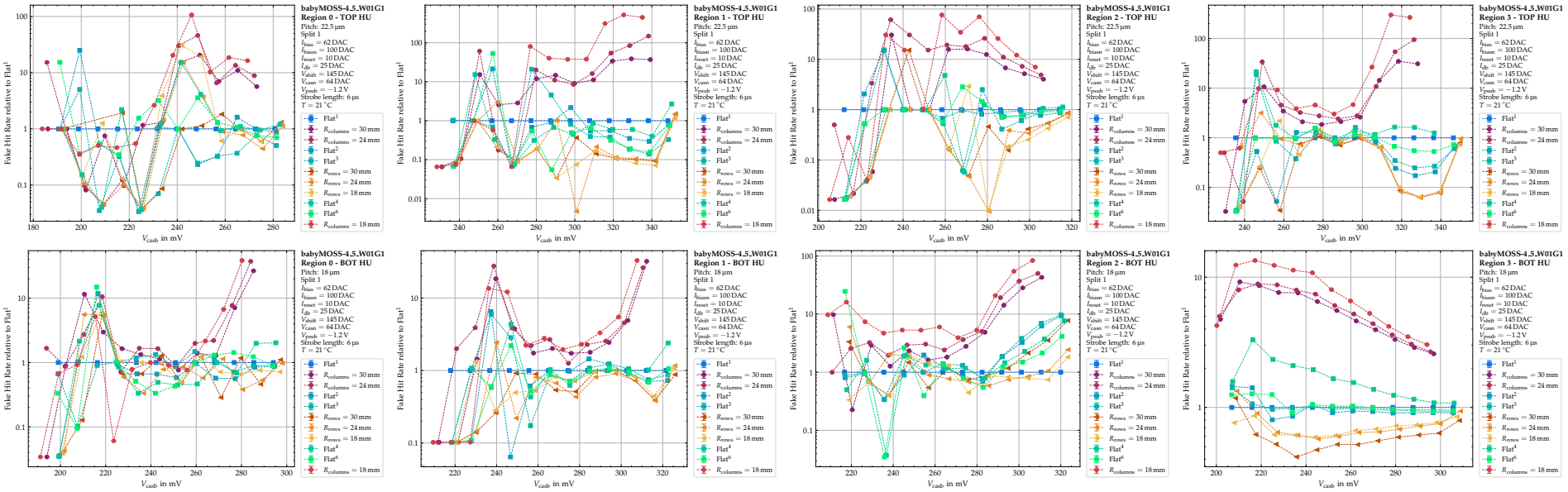

Figure A.2.34: Fake hit rate relative to Flat^1 vs. V_{casb} in mV, for babyMOSS-4_5_W01G1 with $V_{\text{psub}} = -1.2\,\text{V}$.

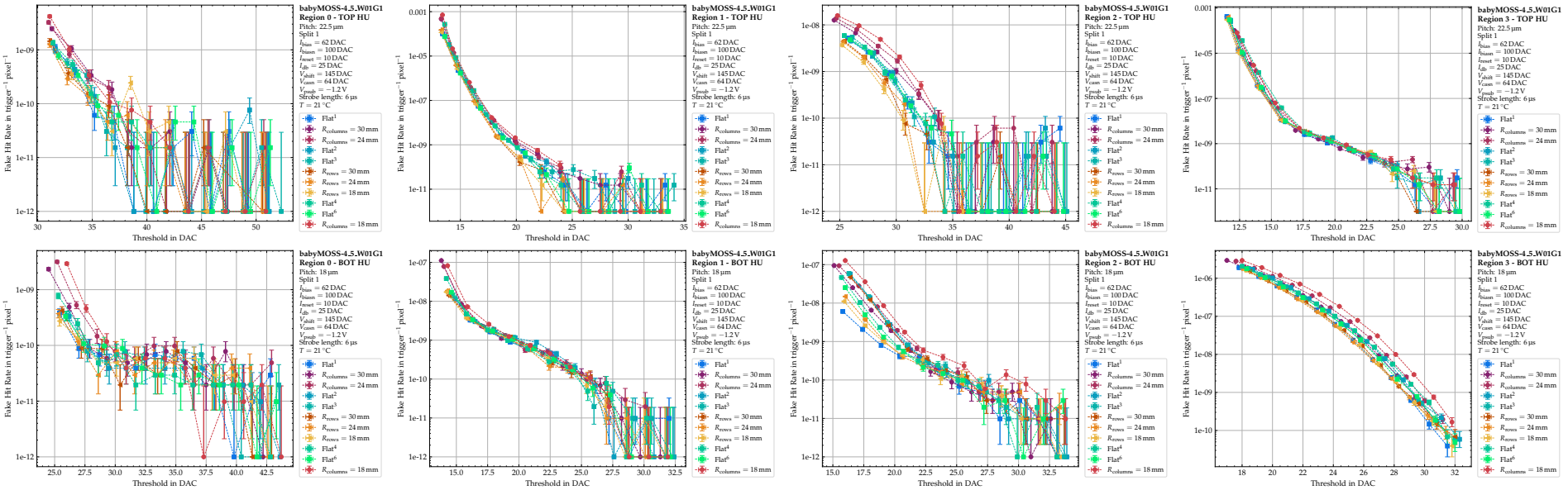

Figure A.2.35: Fake hit rate in trigger^{-1} pixel^{-1} vs. Threshold in DAC, for babyMOSS-4_5_W01G1 with $V_{\text{psub}} = -1.2\,\text{V}$.

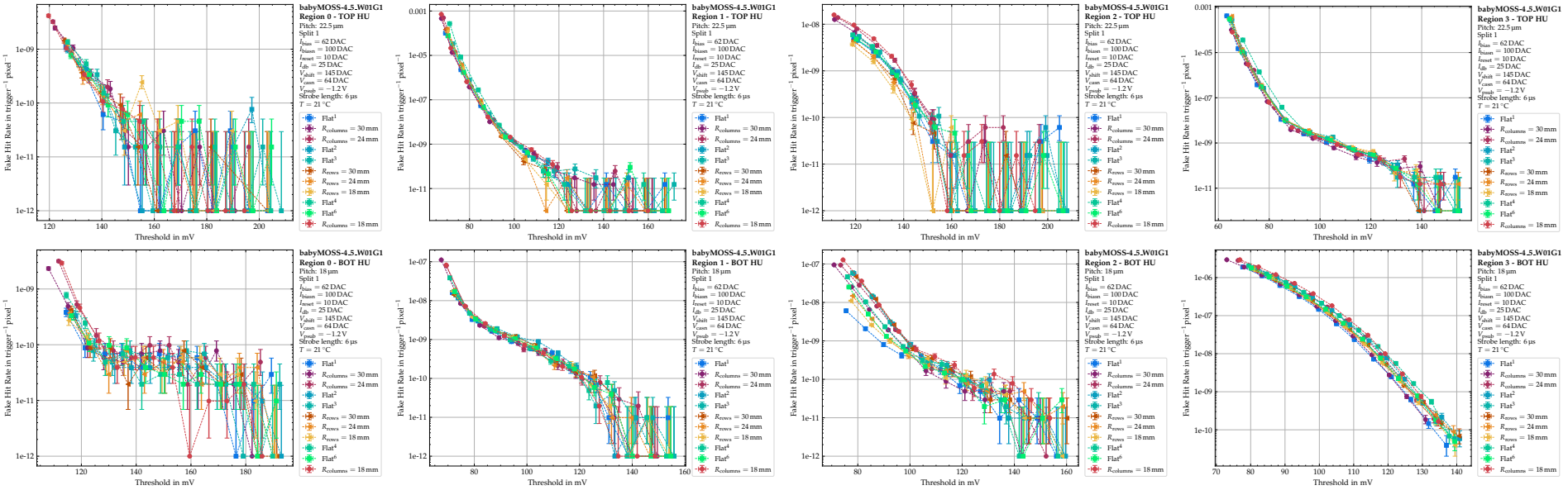

Figure A.2.36: Fake hit rate in trigger^{-1} pixel^{-1} vs. Threshold in mV, for babyMOSS-4_5_W01G1 with $V_{\text{psub}} = -1.2\,\text{V}$.

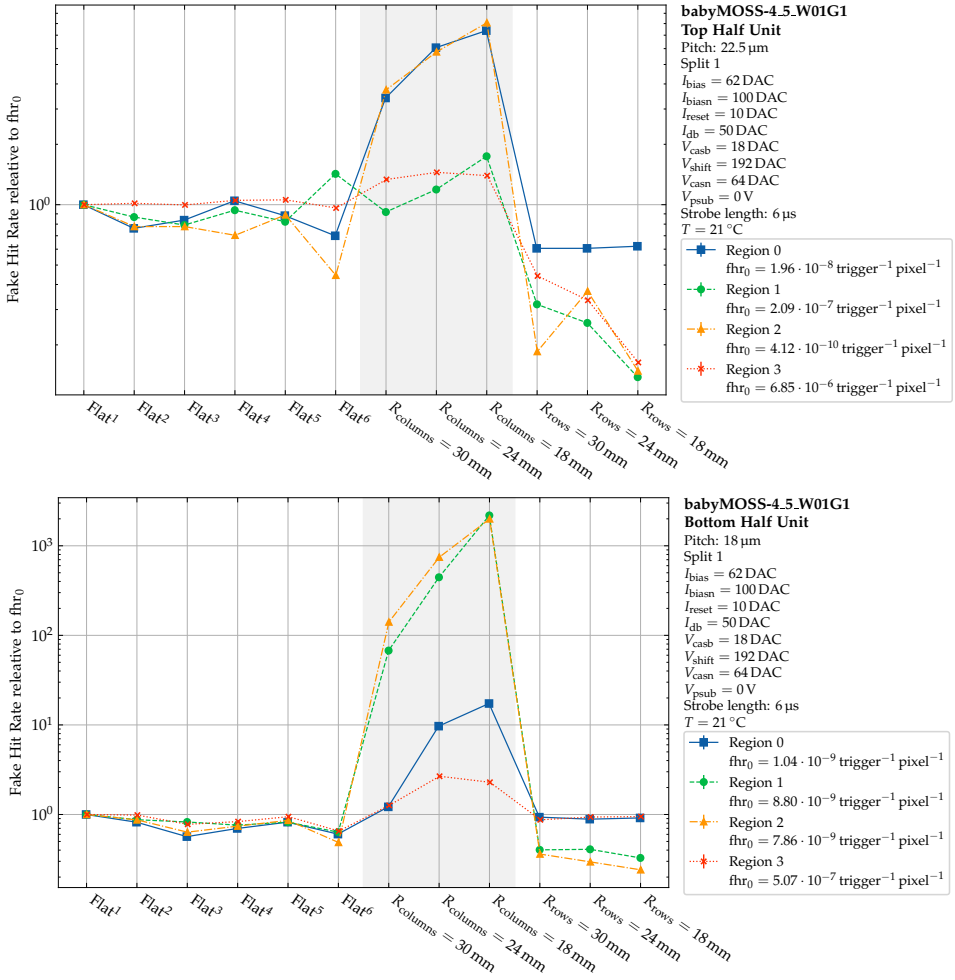

Figure A.2.37: Fake hit rate relative to fhr_0 vs. configuration, for $V_{casb} = 18$ DAC, babyMOSS-4_5_W01G1 with $V_{psub} = 0$ V.

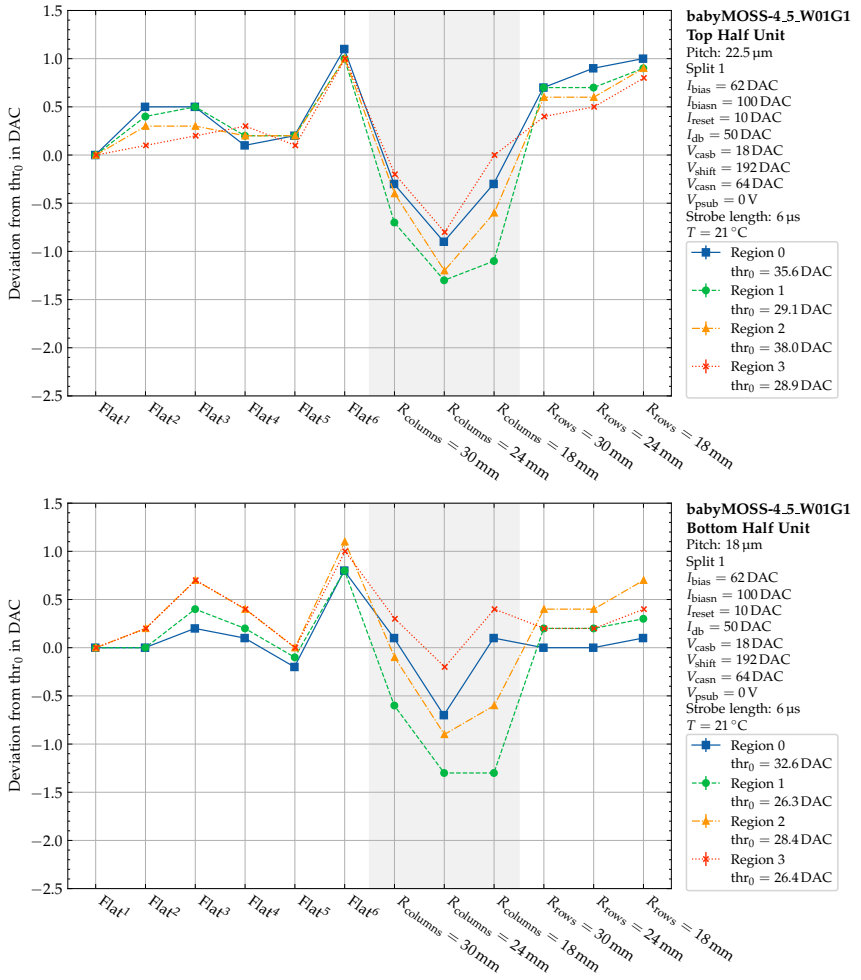

Figure A.2.38: Deviation of Threshold from thr_0 in DAC vs. configuration, $V_{casb} = 18$ DAC, babyMOSS-4_5_W01G1 with $V_{psub} = 0$ V.

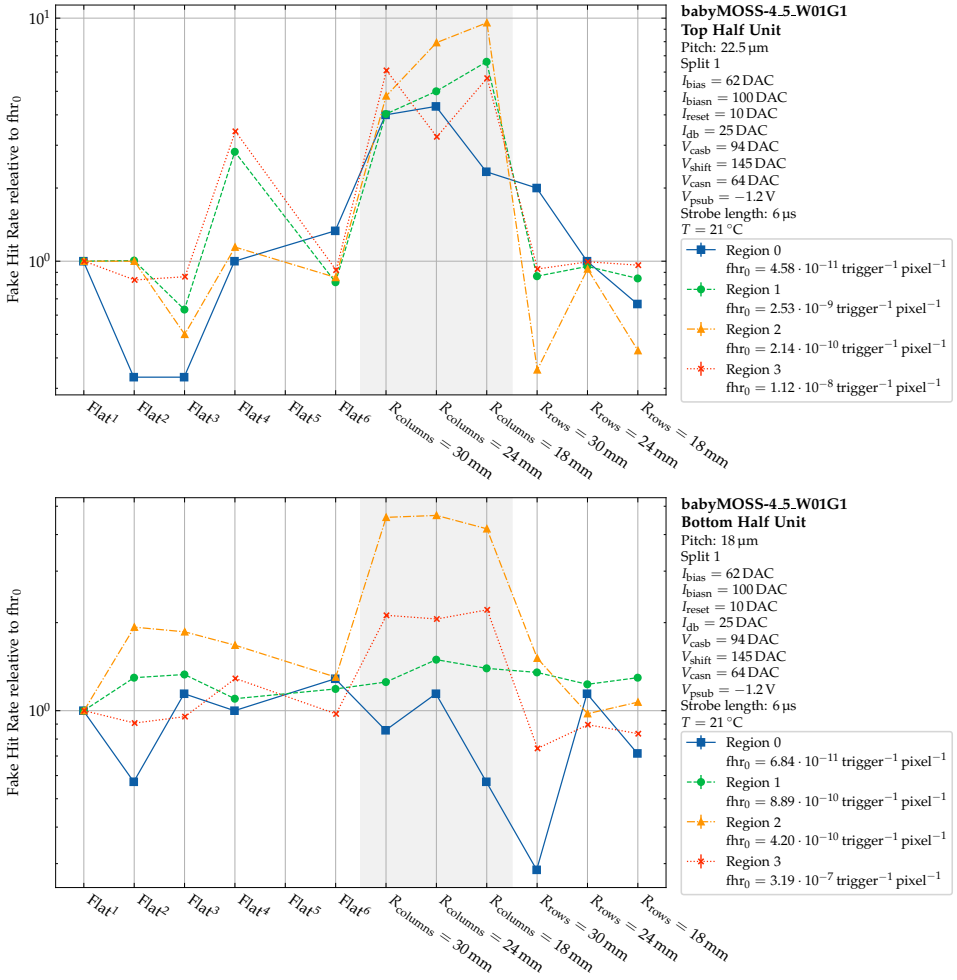

Figure A.2.39: Fake hit rate relative to fhr$_0$ vs. configuration, for $V_{casb} = 94\,\text{DAC}$, babyMOSS-4_5_W01G1 with $V_{psub} = -1.2\,\text{V}$.

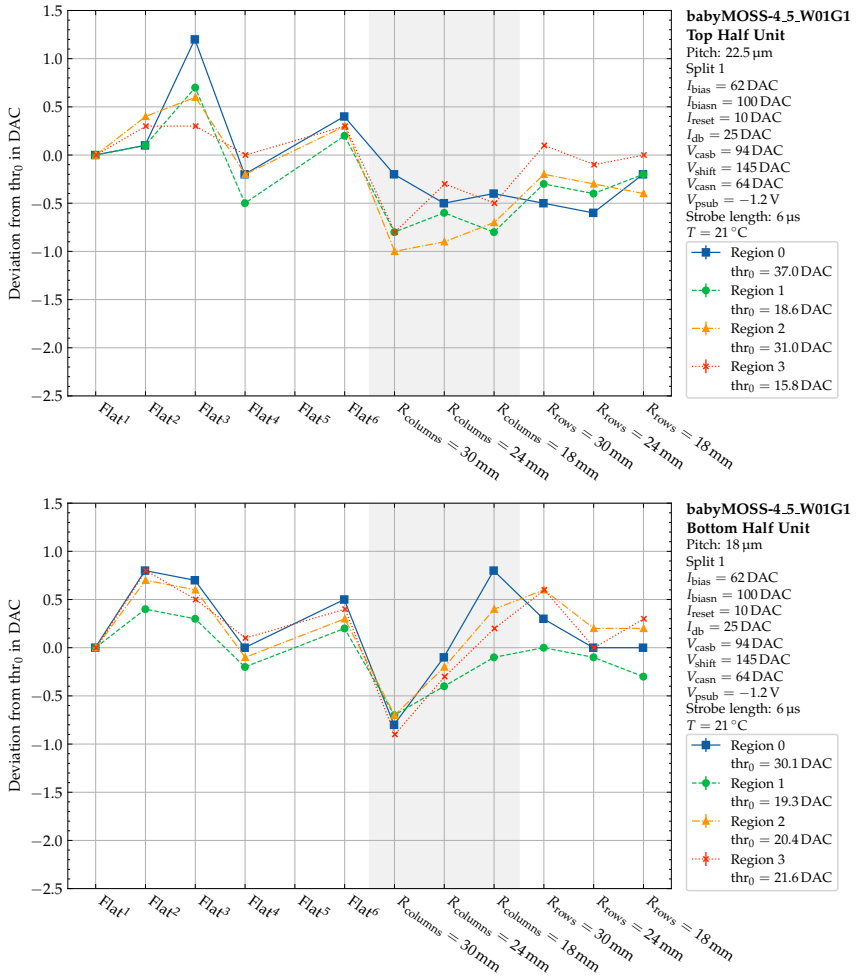

Figure A.2.40: Deviation of Threshold from thr$_0$ in DAC vs. configuration, $V_{casb} = 94\,\text{DAC}$, babyMOSS-4_5_W01G1 with $V_{psub} = -1.2\,\text{V}$.

A.3 babyMOSS-4_3_W01G1

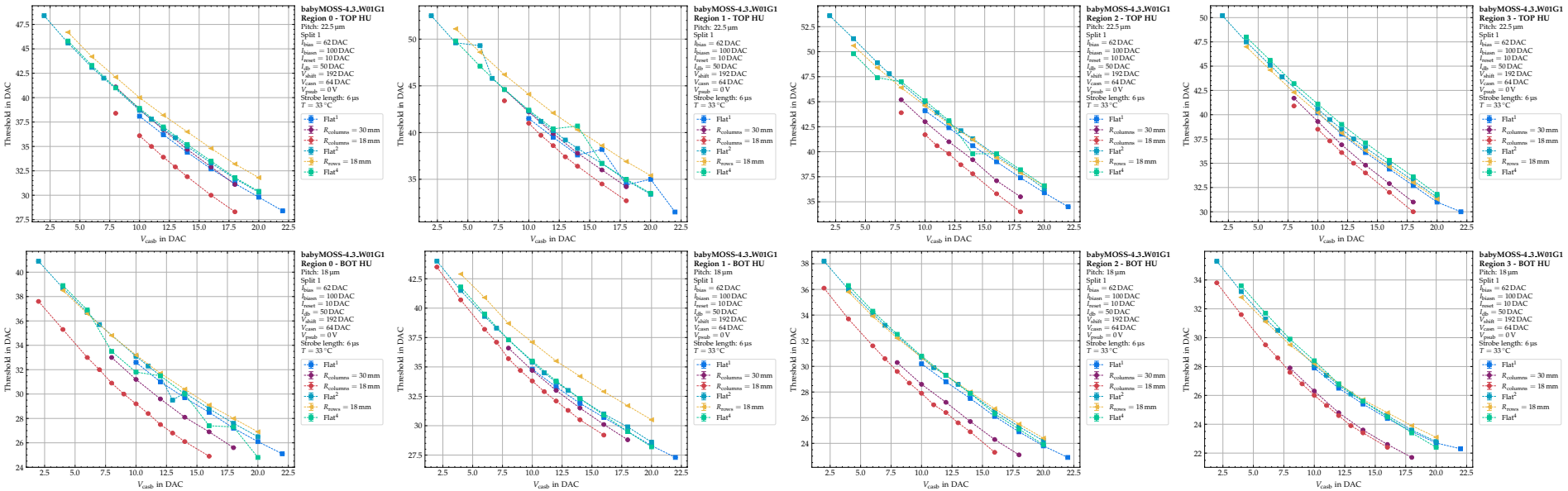

Figure A.3.1: Threshold in DAC vs. V_{casb} in DAC, for babyMOSS-4_5_W01G1 with $V_{\text{psub}} = 0\,\text{V}$.

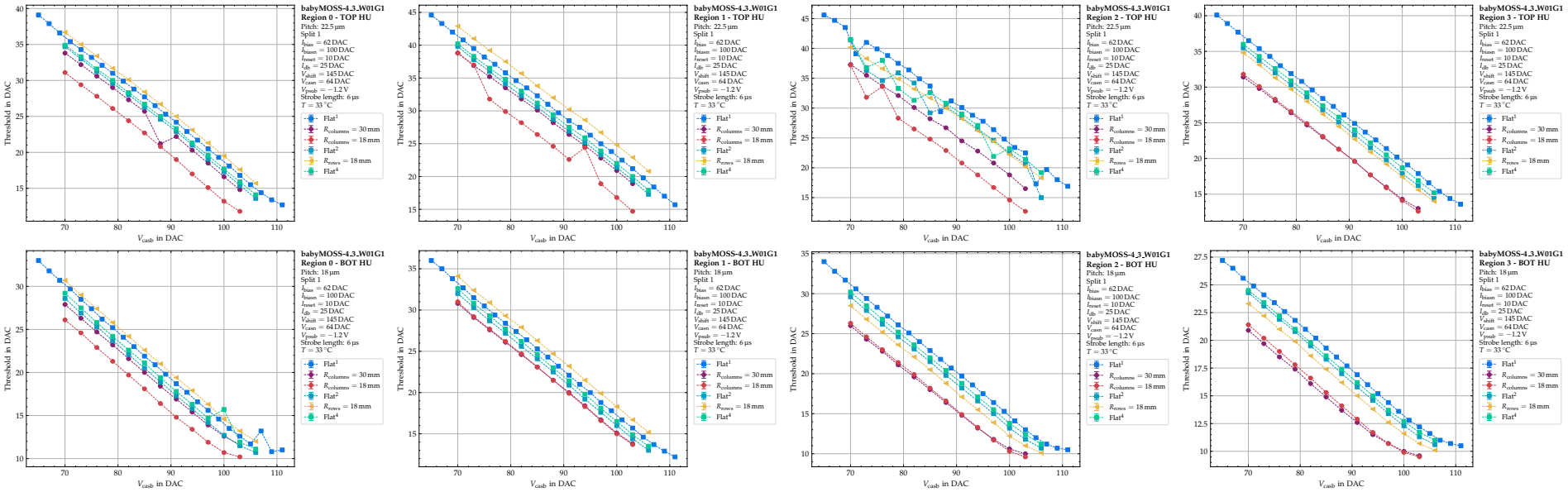

Figure A.3.2: Threshold in DAC vs. V_{casb} in DAC, for babyMOSS-4_5_W01G1 with $V_{\text{psub}} = -1.2\,\text{V}$.

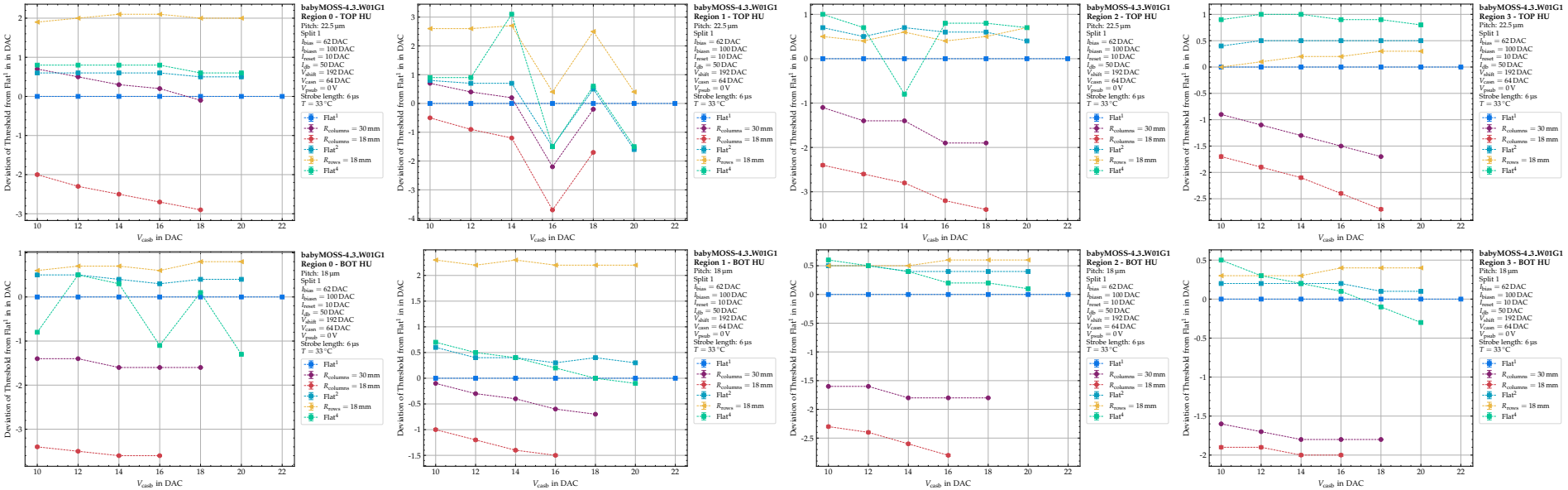

Figure A.3.3: Deviation of Threshold from Flat^1 in DAC vs. V_{casb} in DAC, for babyMOSS-4_5_W01G1 with $V_{\text{psub}} = 0\,\text{V}$.

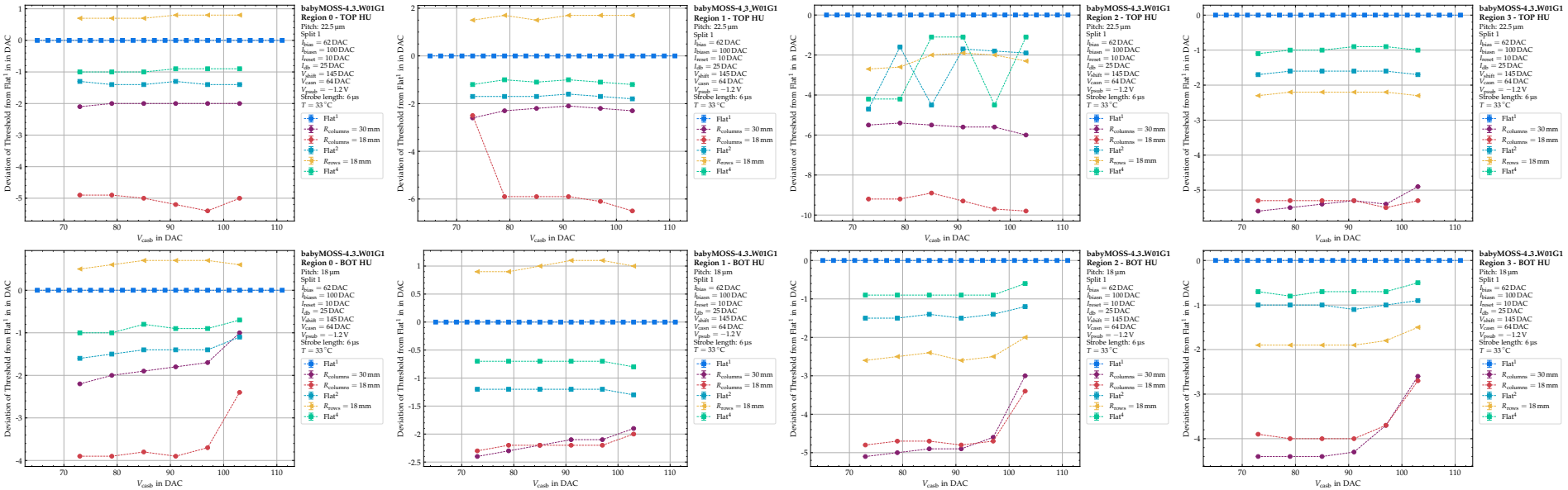

Figure A.3.4: Deviation of Threshold from Flat^1 in DAC vs. V_{casb} in DAC, for babyMOSS-4_5_W01G1 with $V_{\text{psub}} = -1.2\,\text{V}$.

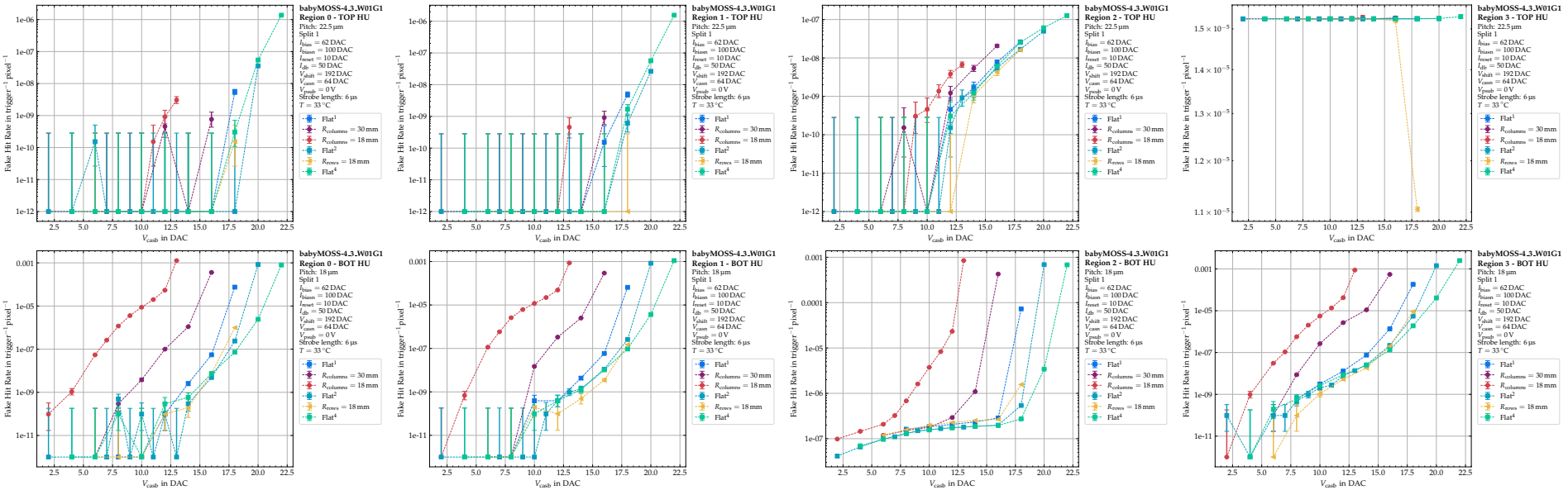

Figure A.3.5: Fake hit rate in trigger^{-1} pixel^{-1} vs. V_{casb} in DAC, for babyMOSS-4_5_W01G1 with $V_{\text{psub}} = 0\,\text{V}$.

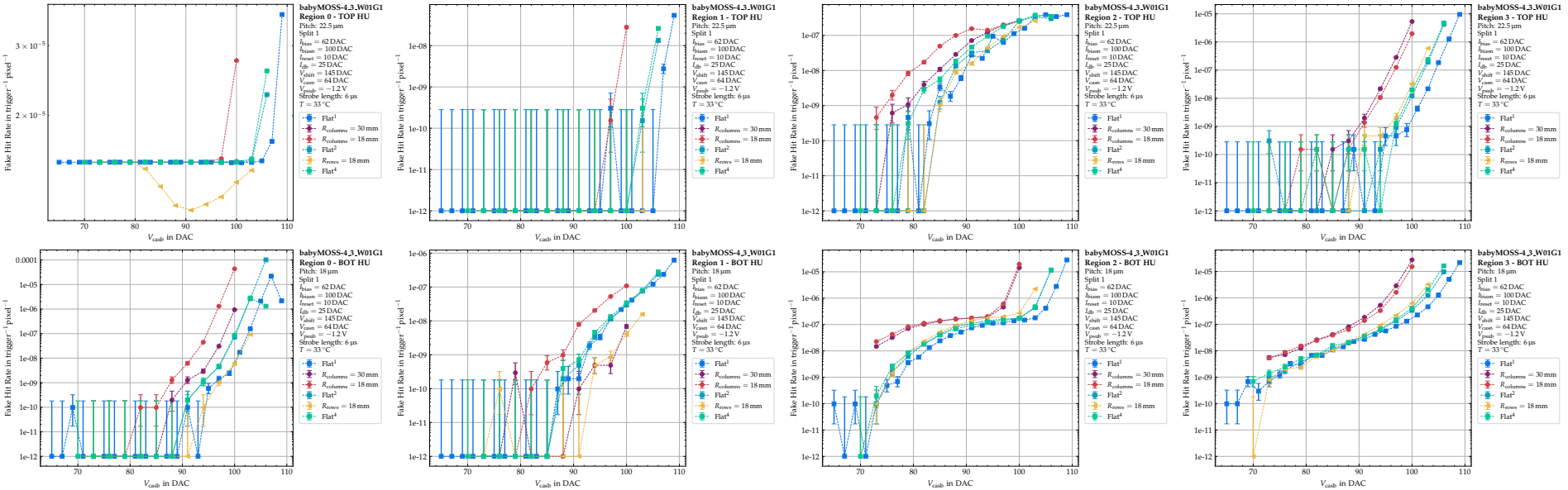

Figure A.3.6: Fake hit rate in trigger^{-1} pixel^{-1} vs. V_{casb} in DAC, for babyMOSS-4_5_W01G1 with $V_{\text{psub}} = -1.2\,\text{V}$.

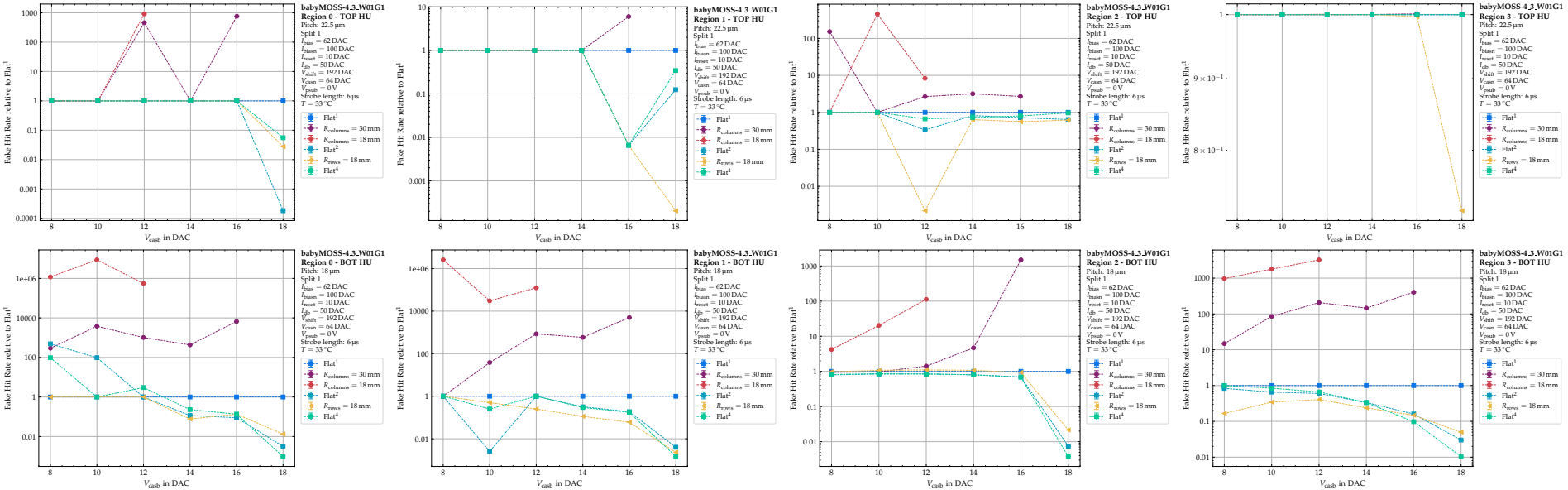

Figure A.3.7: Fake hit rate relative to Flat^1 vs. V_{casb} in DAC, for babyMOSS-4_5_W01G1 with $V_{\text{psub}} = 0\,\text{V}$.

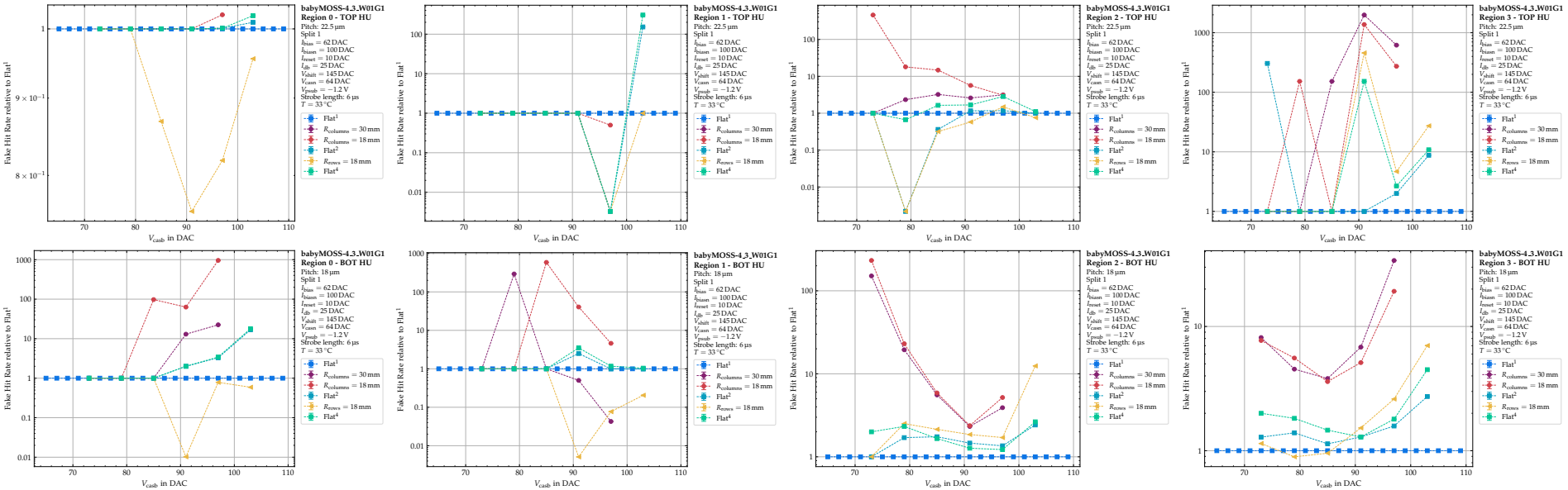

Figure A.3.8: Fake hit rate relative to Flat^1 vs. V_{casb} in DAC, for babyMOSS-4_5_W01G1 with $V_{\text{psub}} = -1.2\,\text{V}$.

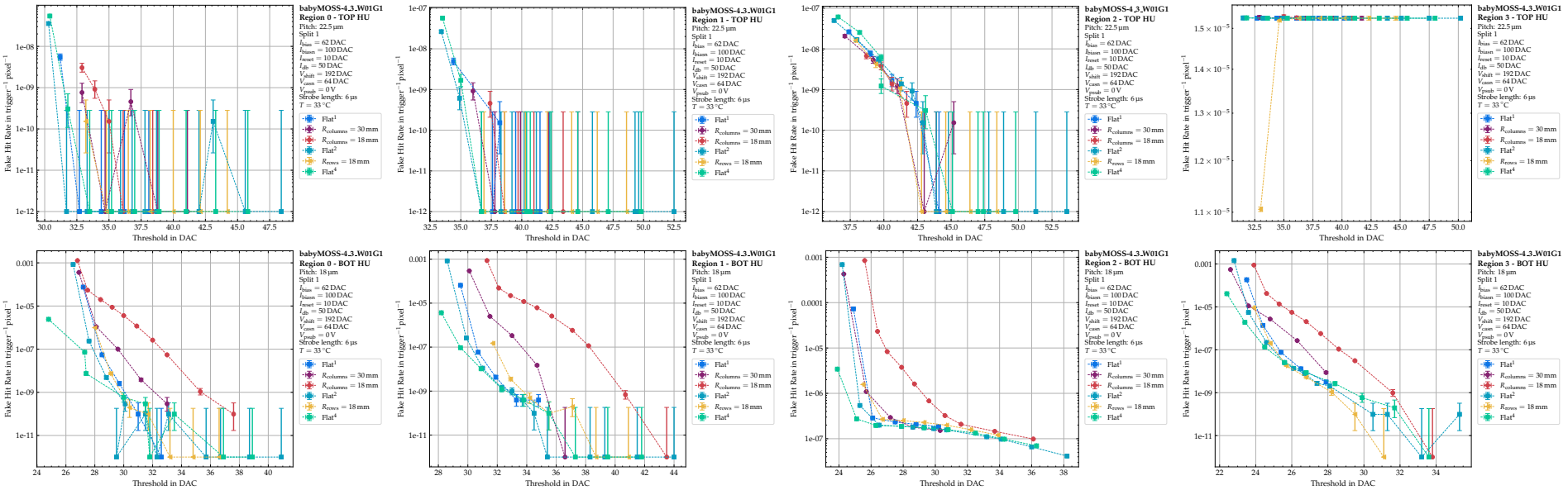

Figure A.3.9: Fake hit rate in trigger^{-1} pixel^{-1} vs. Threshold in DAC, for babyMOSS-4_5_W01G1 with $V_{\text{psub}} = 0\,\text{V}$.

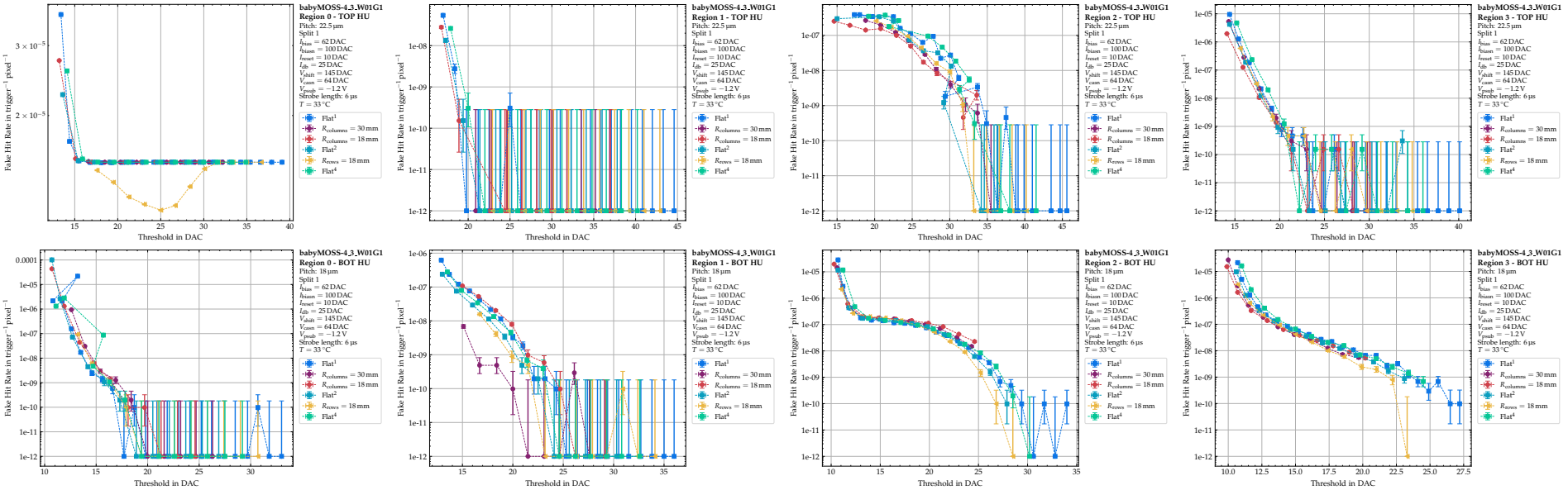

Figure A.3.10: Fake hit rate in trigger^{-1} pixel^{-1} vs. Threshold in DAC, for babyMOSS-4_5_W01G1 with $V_{\text{psub}} = -1.2\,\text{V}$.

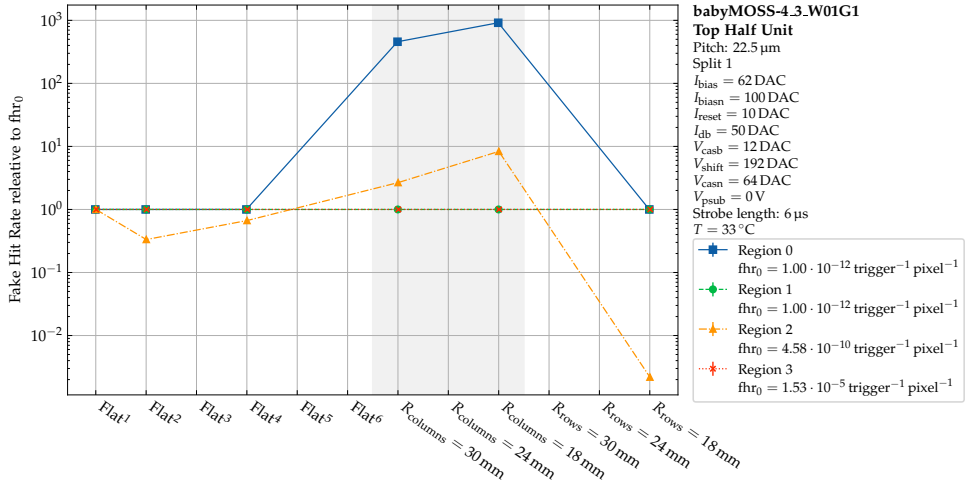

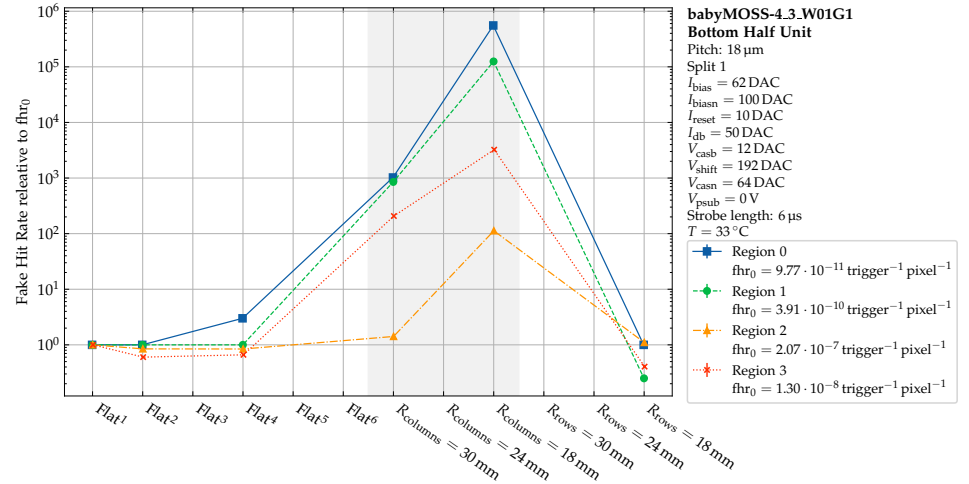

Figure A.3.11: Fake hit rate relative to fhr$_0$ vs. configuration, for $V_{casb} = 12\,\mathrm{DAC}$, babyMOSS-4_3_W01G1 with $V_{psub} = 0\,\mathrm{V}$.

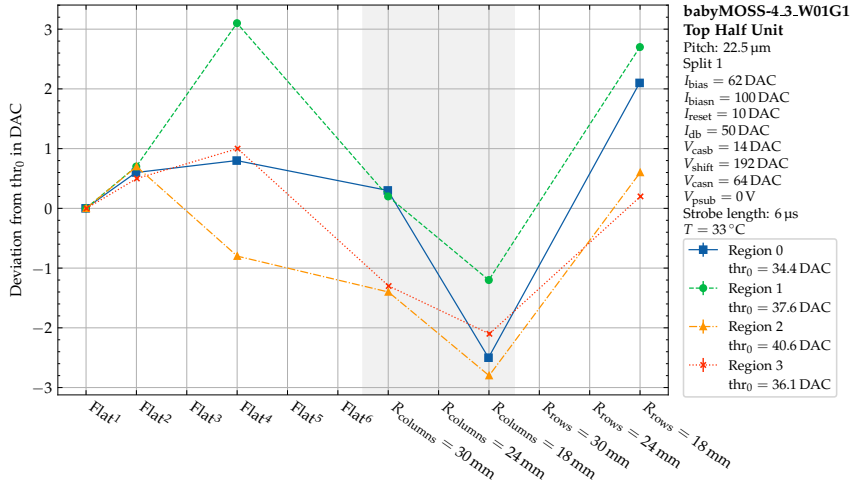

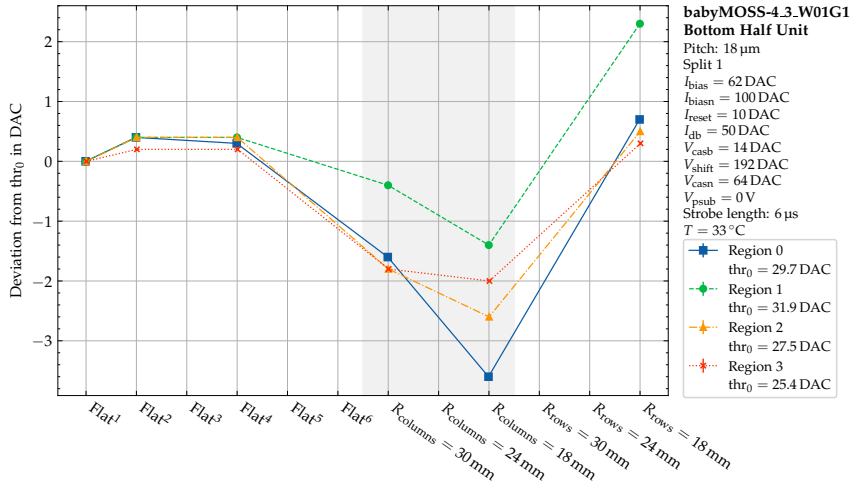

Figure A.3.12: Deviation of Threshold from thr$_0$ in DAC vs. configuration, $V_{casb} = 14\,\mathrm{DAC}$, babyMOSS-4_5_W01G1 with $V_{psub} = 0\,\mathrm{V}$.

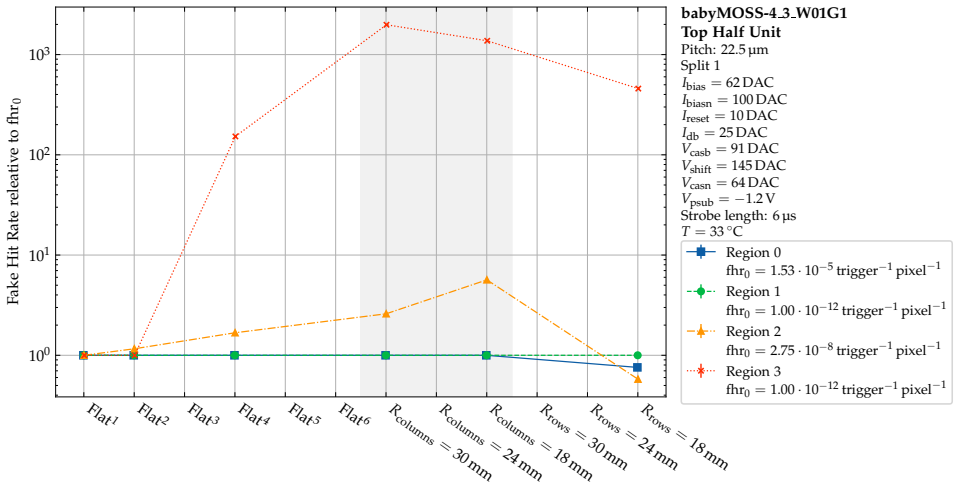

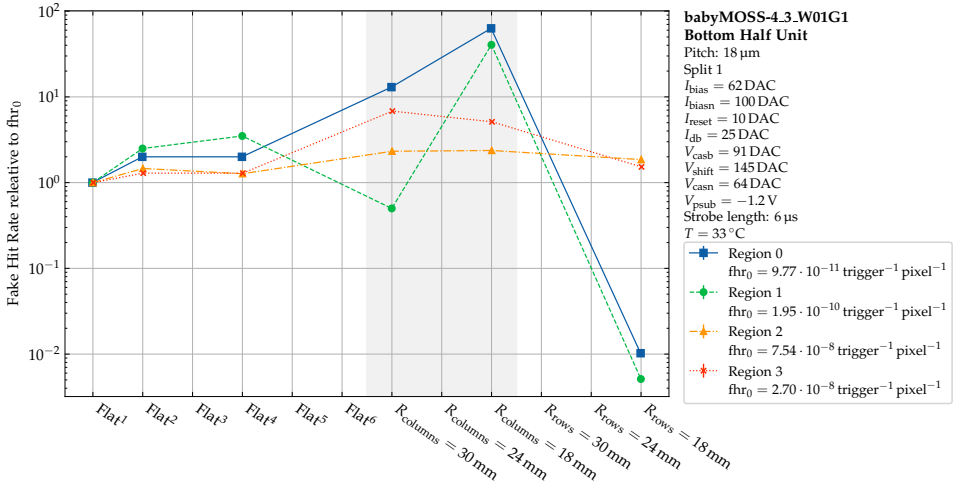

Figure A.3.13: Fake hit rate relative to fhr_0 vs. configuration, for $V_{casb} = 91$ DAC, babyMOSS-4_3_W01G1 with $V_{psub} = -1.2$ V.

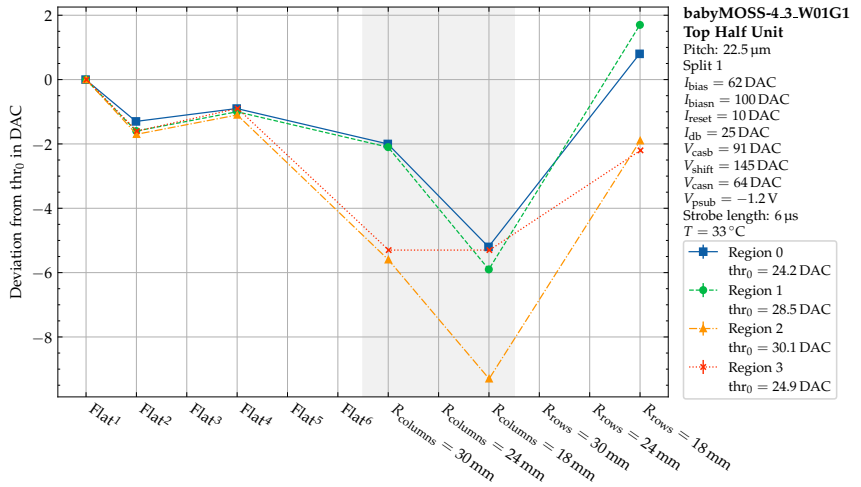

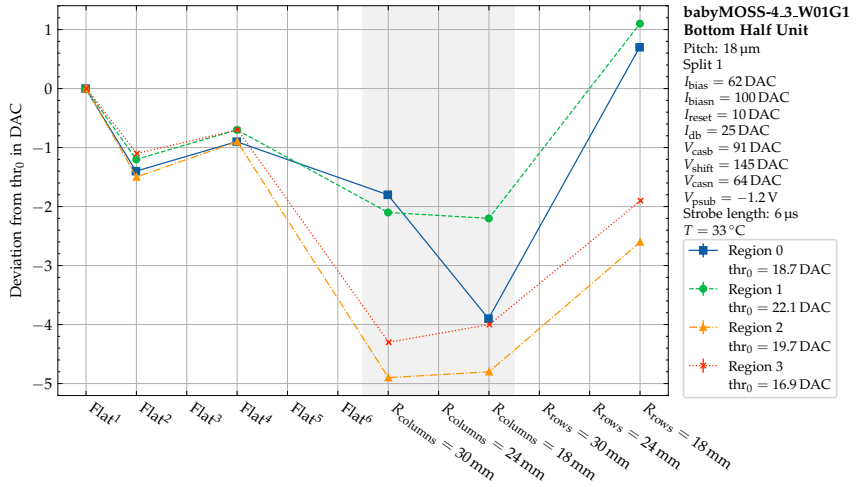

Figure A.3.14: Deviation of Threshold from thr_0 in DAC vs. configuration, $V_{casb} = 91$ DAC, babyMOSS-4_5_W01G1 with $V_{psub} = -1.2$ V.

B Efficiency

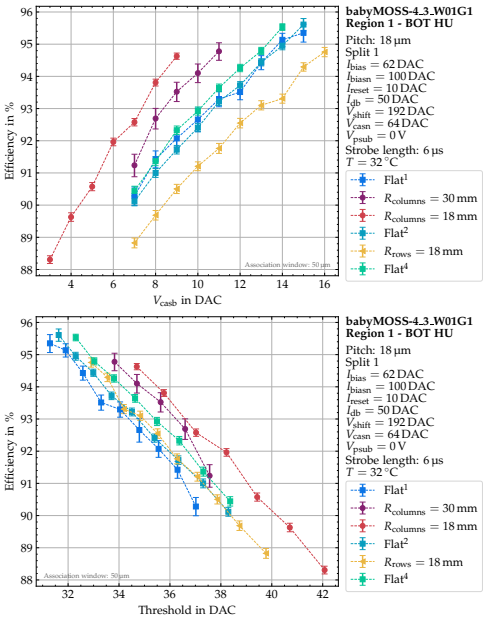

Figure B.0.1: Efficiency vs. V_{casb} (top) and threshold (bottom), both in DAC units, for region 1 of the BOT HU of babyMOSS-4_3_W01G1 with $V_{\text{psub}} = 0\,\text{V}$.

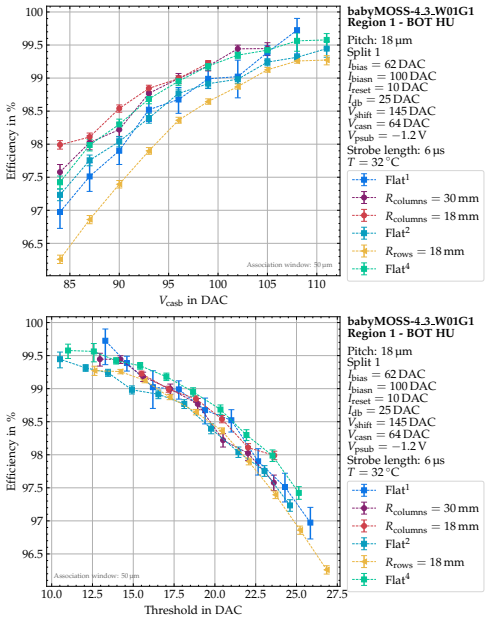

Figure B.0.2: Efficiency vs. V_{casb} (top) and threshold (bottom), both in DAC units, for region 1 of the BOT HU of babyMOSS-4_3_W01G1 with $V_{\text{psub}} = -1.2\,\text{V}$.

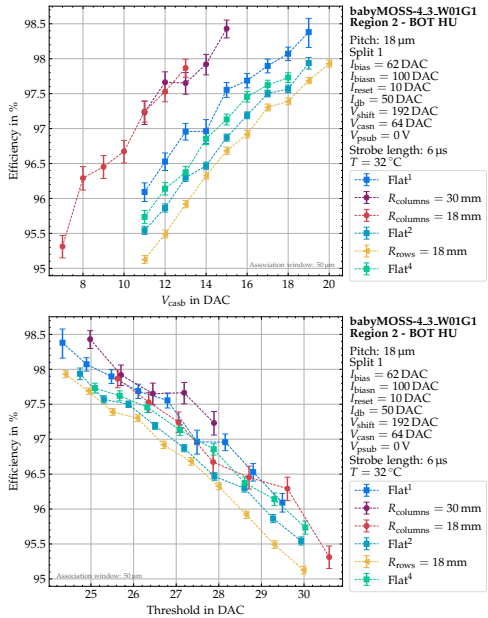

Figure B.0.3: Efficiency vs. V_{casb} (top) and threshold (bottom), both in DAC units, for region 2 of the BOT HU of babyMOSS-4_3_W01G1 with $V_{\text{psub}} = 0\,\text{V}$.

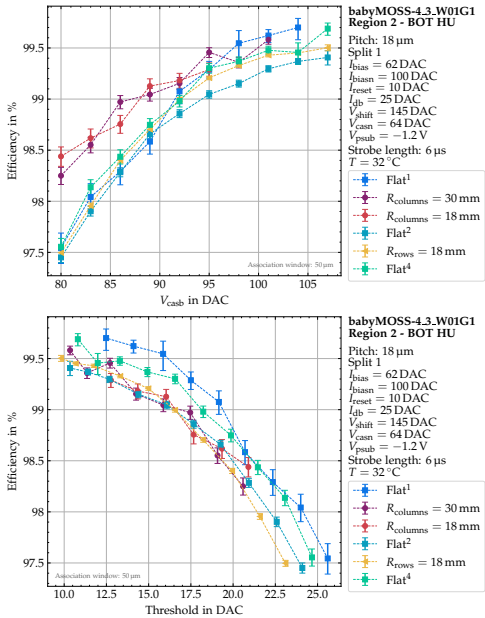

Figure B.0.4: Efficiency vs. V_{casb} (top) and threshold (bottom), both in DAC units, for region 2 of the BOT HU of babyMOSS-4_3_W01G1 with $V_{\text{psub}} = -1.2\,\text{V}$.

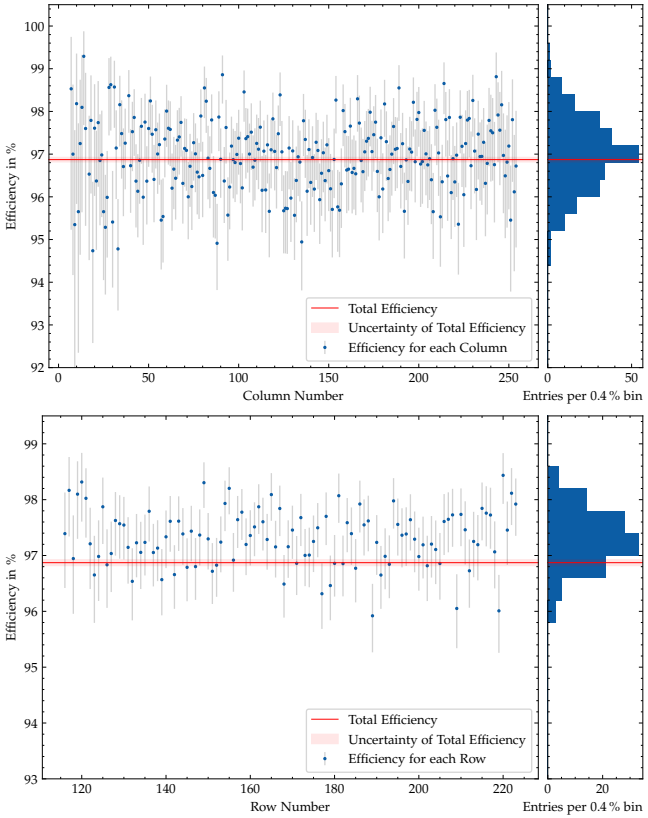

Figure B.0.5: Efficiency vs. columns (top) and rows (bottom), for Flat^2, $V_{\text{casb}} = 15\,\text{DAC}$, region 2 of the BOT HU of babyMOSS-4_3_W01G1 with $V_{\text{psub}} = 0\,\text{V}$. The efficiency distribution and the mean of the whole region are also indicated.

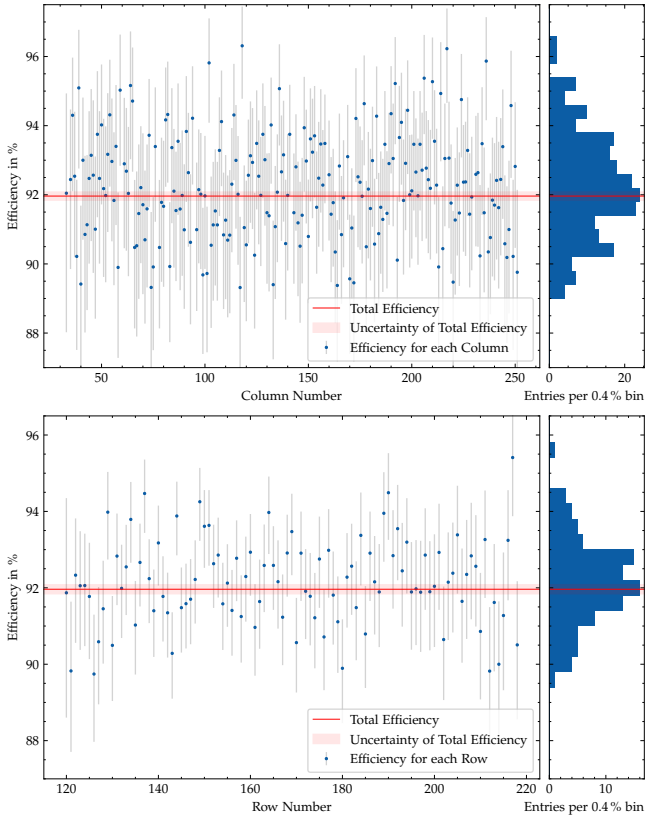

Figure B.0.6: Efficiency vs. columns (top) and rows (bottom), for $R_{\text{columns}} = 18\,\text{mm}$, $V_{\text{casb}} = 10\,\text{DAC}$, region 1 of the BOT HU of babyMOSS-4_3_W01G1 with $V_{\text{psub}} = 0\,\text{V}$. The efficiency distribution and the mean of the whole region are also indicated.

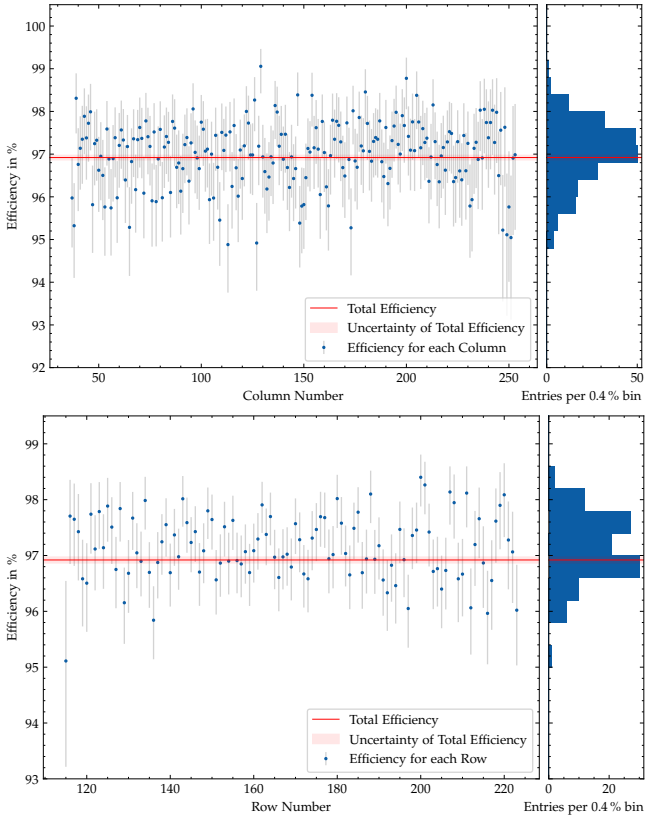

Figure B.0.7: Efficiency vs. columns (top) and rows (bottom), for $R_{\text{rows}} = 18\,\text{mm}$, $V_{\text{casb}} = 16\,\text{DAC}$, region 2 of the BOT HU of babyMOSS-4_3_W01G1 with $V_{\text{psub}} = 0\,\text{V}$. The efficiency distribution and the mean of the whole region are also indicated.